NASA/CR–2010-216731

Aero-Structural Assessment of an Inflatable Aerodynamic Decelerator

Essam F. Sheta, Vinod Venugopalan, X. G. Tan, Peter A. Liever, and Sami D. Habchi
CFD Research Corporation, Huntsville, Alabama

August 2010

NASA STI Program . . . in Profile

Since its founding, NASA has been dedicated to the advancement of aeronautics and space science. The NASA scientific and technical information (STI) program plays a key part in helping NASA maintain this important role.

The NASA STI program operates under the auspices of the Agency Chief Information Officer. It collects, organizes, provides for archiving, and disseminates NASA's STI. The NASA STI program provides access to the NASA Aeronautics and Space Database and its public interface, the NASA Technical Report Server, thus providing one of the largest collections of aeronautical and space science STI in the world. Results are published in both non-NASA channels and by NASA in the NASA STI Report Series, which includes the following report types:

- TECHNICAL PUBLICATION. Reports of completed research or a major significant phase of research that present the results of NASA programs and include extensive data or theoretical analysis. Includes compilations of significant scientific and technical data and information deemed to be of continuing reference value. NASA counterpart of peer-reviewed formal professional papers, but having less stringent limitations on manuscript length and extent of graphic presentations.

- TECHNICAL MEMORANDUM. Scientific and technical findings that are preliminary or of specialized interest, e.g., quick release reports, working papers, and bibliographies that contain minimal annotation. Does not contain extensive analysis.

- CONTRACTOR REPORT. Scientific and technical findings by NASA-sponsored contractors and grantees.

- CONFERENCE PUBLICATION. Collected papers from scientific and technical conferences, symposia, seminars, or other meetings sponsored or co-sponsored by NASA.

- SPECIAL PUBLICATION. Scientific, technical, or historical information from NASA programs, projects, and missions, often concerned with subjects having substantial public interest.

- TECHNICAL TRANSLATION. English-language translations of foreign scientific and technical material pertinent to NASA's mission.

Specialized services also include creating custom thesauri, building customized databases, and organizing and publishing research results.

For more information about the NASA STI program, see the following:

- Access the NASA STI program home page at *http://www.sti.nasa.gov*

- E-mail your question via the Internet to help@sti.nasa.gov

- Fax your question to the NASA STI Help Desk at 443-757-5803

- Phone the NASA STI Help Desk at 443-757-5802

- Write to:
  NASA STI Help Desk
  NASA Center for AeroSpace Information
  7115 Standard Drive
  Hanover, MD 21076-1320

NASA/CR–2010-216731

Aero-Structural Assessment of an Inflatable Aerodynamic Decelerator

Essam F. Sheta, Vinod Venugopalan, X. G. Tan, Peter A. Liever, and Sami D. Habchi
CFD Research Corporation, Huntsville, Alabama

National Aeronautics and
Space Administration

Langley Research Center
Hampton, Virginia 23681-2199

Prepared for Langley Research Center
under Contract NNM06AA10C

August 2010

Available from:

NASA Center for AeroSpace Information
7115 Standard Drive
Hanover, MD 21076-1320
443-757-5802

SUMMARY

NASA is conducting an Entry, Descent and Landing Systems Analysis (EDL-SA) Study to determine the key technology development projects that should be undertaken for enabling the landing of large payloads on Mars for both human and robotic missions. Inflatable Aerodynamic Decelerators (IADs) are one of the candidate technologies. A variety of EDL architectures are under consideration. The current effort is conducted under NASA SBIR Phase III program for development and simulations of computational framework for inflatable structures.

In the Phase I study of this program, the feasibility of the CFDRC's Multi-Disciplinary Integrated Computing Environment (MDICE) was demonstrated for simulations of thin-walled ballute configurations. The simulations were conducted using CFDRC's in-house fluid dynamics and structural dynamics codes. In the Phase II study, selected codes were implemented and integrated into the MDICE framework for aeroelastic simulations of ballute configurations. The selected codes include NASA LaRC CFD FUN3D code, NASA JSC DSMC DAC code, and ABAQUS finite element structural dynamics code. The framework was validated by conducting aeroelastic simulations of the NASA Langley wind tunnel model for a 6-inch clamped ballute. The results compared fairly well with the wind tunnel data. The framework was also demonstrated for coupled fluid structure interaction of nonlinear model of attached ballute configuration supplied by Ball Aerospace.

The objective of this Phase III effort is to provide computational aero-structural and dynamic analysis and simulations to support the EDL-SA assessments of IAD controllability and structural integrity for Mars Aerocapture and EDL. Several design configurations and analyses are considered to determine the candidate technology that meets the requirements. Among the important considerations for IADs is whether they provide the desired controllability and can withstand the loads induced by banking maneuvers.

Geometrical and grid models for the considered IAD configurations are developed and tested. NASA provided CFDRC with the geometrical models, flow conditions, the material properties, and other information as needed to perform the simulations. The notional model was for double stack Toroids configuration consists of 23 toroidal tubes. A reacting thermally perfect CO2 model was used to simplify the Mars atmosphere. A coupled dynamic aero-structural simulations are performed for all cases using Euler CFD analysis, structural Finite-Element (FEM) analysis, and prescribed trajectory motion. Extensive FEM simulations were conducted with various dynamic and internal pressures and using variable fidelity CFD calculated loads. The aeroelastic responses of the model were computed using two-way fluid-structure interaction (FSI) coupling. In addition, aeroelastic responses of several cases were also computed using one-way FSI coupling from the fluid to the structure. The structural deformations and stresses exhibited mostly cyclic behavior over the model and tended to fluctuate around almost constant mean values. The results show dramatic decrease of the aeroelastic deformations when the effects of radial enforcement straps are added to the model. The von Mises stress levels on the Gores and Toroids were far less than the yield stress of the materials of the Gores and Toroids.

A new IAD configuration model based on single stack Toroids was also considered. The aerodynamic flowfield and forces of the single stack Toroids configuration were very similar to the double stack Toroids configuration. There were small increases in the displacements and in the von Mises stresses. The single stack Toroids configuration model was also tested at multiples of the reference dynamic pressure. The dynamic response showed an increased number of modes with an increase in flow dynamic pressure. The stresses were still within limits even for the case with 1.5 times the reference dynamic pressure.

PREFACE

This is the final report for the NASA SBIR Phase III contract entitled "Aero-Structural Assessment of an Inflatable Aerodynamic Decelerator". This project is sponsored by NASA Langley Research Center as follow-on to Phase II SBIR (NASA Contract Number NNM06AA10C). The effort is performed by CFD Research Corporation (CFDRC Project Number 8927). The principal investigator is Dr. Essam F. Sheta, and the co-investigator was Mr. Vinod Venugopalan. The Project Manager is Mr. Sami D. Habchi. The technical monitor of this project is Dr. Jamshid Samareh (NASA Langley Research Center).

ACKNOWLEDGEMENTS

The authors of this report would like to express their appreciation to the technical monitor Dr. Jamshid Samareh of NASA Langley Research Center for his close participation and discussions regarding the content and direction of this effort. The author would also like to thank Ms. Michelle Munk, Mr. Robert Dillman, and Mr. Thomas Zang of NASA Langley Research Center for their feedback on the direction of the effort.

TABLE OF CONTENTS

LIST OF FIGURES

LIST OF TABLES

1 INTRODUCTION

1.1 Background

NASA is conducting an Entry, Descent and Landing Systems Analysis (EDL-SA) Study to determine the key technology development projects that should be undertaken for enabling the landing of large payloads on Mars for both human and robotic missions. Inflatable Aerodynamic Decelerators (IADs) are one of the candidate technologies. A variety of EDL architectures are under consideration. Taken together these architectures include IADs for aerocapture (hypersonic) and for the entry (hypersonic) and the descent (supersonic and subsonic) stages of EDL. Many aspects of IADs need to be considered, e.g., inflatability, heating, deformation, structural integrity, aerodynamic performance, and controllability. For each stage there are rather challenging requirements. Part of the EDL-SA assessment includes determining whether the candidate technologies meet the requirements. Among the important considerations for IADs are whether they provide the desired controllability and can withstand the loads induced by banking maneuvers. The purpose of this effort is to provide computational predictions to support the EDL-SA assessments of IAD controllability and structural integrity for Mars Aerocapture and EDL.

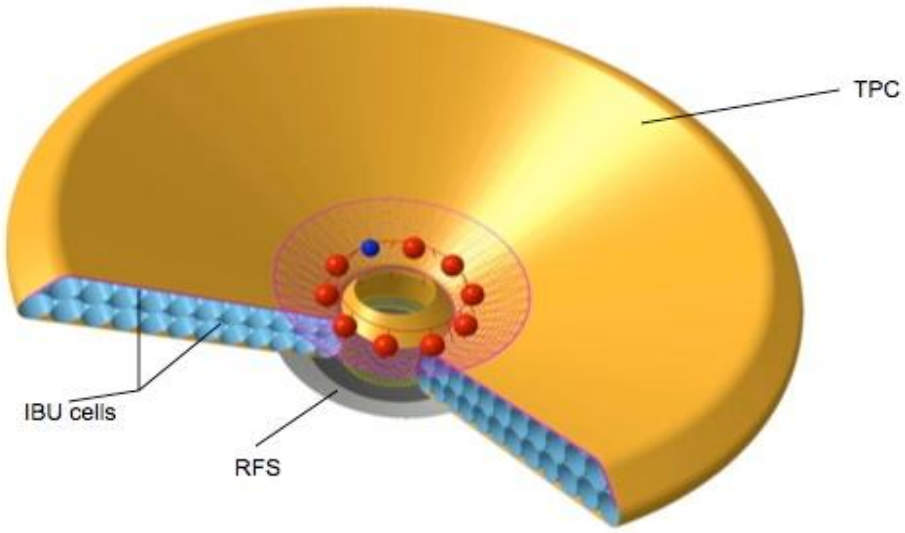

Figure 1. Notional design of an IAD.

Figure 1 illustrates the key components of the IADs under consideration. The Inflatable Braking Unit (IBU) consists of pressurized internal toroidal cells covered with a smooth surface containing the Thermal Protective Cover (TPC). The structural properties of the IBU are nonlinear. The Rigid Front Shell (RFS) is a rigid metallic structure. The payload is a cylinder that attaches to the back portion of the RFS. In this effort, the payload is not modeled. The model is subject to banking maneuver that is modeled by a prescribed rotational motion of the RFS. The flow field and the structural response of the model are three-dimensional and exhibit no symmetries. The aerodynamics will be described by the Euler equations.

1.2 Work Scope

The scope of this work is to conduct CFD aero-structural and dynamic simulations of Inflatable Aerodynamic Decelerators (IADs). The computation predictions are intended to answer the question: For a specific design and configuration, what range, if any, of internal pressures does the IBU maintain structural integrity during the banking maneuver?

The flow conditions of primary interest are Mach 18 at angles of attack of 30 degrees. The banking maneuver corresponds to a prescribed acceleration of the RFS of 5 deg/sec^2 with duration of 4 seconds. The computations will first determine the steady flow field at the flow conditions, and then conduct the banking maneuver. The predictions will include time histories of the aerodynamic forces and moments, the structural deformations of the IBU, and the stresses at the RFS–IBU attachment points.

The effort in this contract was performed under the following tasks:

Task 1: Development of Computational Models
Develop three-dimensional computational models for the aerodynamics, structural dynamics, and dynamics motion of the notional IAD design. A simplified Mars atmosphere chemistry model with an equivalent specific heat ratio is developed for the aerodynamics model. Several structural models are considered and tested to select the appropriate model for the rest of the effort. Chapter 4 of this report discusses the effort conducted under Task 1.

Task 2: Aeroelastic and Dynamic Analysis of Double Stack IAD Configuration
Conduct aero-structural and dynamic simulations of the notional double stack toroids IAD configuration at 30 degrees angle of attack and bank angle rate of 5 deg/sec^2. There are two subtasks are performed in this simulation:

1. Rigid body and steady flow simulation of the double stack IAD at 30 degrees angle of attack and no dynamic motion. The final solution of this subtask will be used as the initial conditions for the aeroelastic and dynamic simulations.
2. Conduct aeroelastic and dynamic simulation of the double stack IAD at 30 degrees angle of attack and bank angle rate of 5 deg/sec^2. Simulations will be carried out for 4 seconds.

The model and results of Task 2 simulations are discussed in details in Chapter 5 of this report.

Task 3: Aeroelastic and Dynamic Analysis of Modified Double Stack IAD Configuration at 30^0 Angle of Attack
Conduct aero-structural and dynamic simulation of a modified design of the double stack IAD configuration at 30^o angle of attack and bank angle rate of 5 deg/sec^2. The design modifications included different internal tube pressures, different structural material properties, and different thickness dimensions based on modeling the effects of radial straps. There are two subtasks are performed in this simulation:

1. Modify the 3D structural FEM model to account for the modified material properties, modified model thickness dimensions, and different internal toroidal pressures.

2. Conduct aeroelastic and dynamic simulation of the modified IAD at 30^o angle of attack and bank angle rate of 5 deg/sec^2.

The model and results of Task 3 simulations are discussed in details in Chapter 6 of this report.

Task 4: <u>Aeroelastic and Dynamic Analysis of Single Stack IAD Design at 30^o Angle of Attack</u>

Conduct aero-structural and dynamic simulation of a single stack toroids IAD design at 30^o angle of attack and bank angle rate of 5 deg/sec^2. The design modifications may include different internal tube pressures, different structural material and/or thickness properties, or different IAD shape. There are three subtasks to be performed in this simulation:

1. Modify the 3D structural FEM model and CFD computational model for the single stack IAD model, including the corresponding material properties, thickness dimensions, and internal toroidal pressures.
2. Conduct rigid body steady flow simulation of the single stack toroids IAD at 30^o angle of attack and no dynamic motion.
3. Conduct aeroelastic and dynamic simulation of the single stack toroids IAD at 30^o angle of attack and bank angle rate of 5 deg/sec^2. Simulations will be carried out for 4 seconds.

The model and results of Task 4 simulations are discussed in details in Chapter 7 of this report.

Task 5: <u>Effect of Dynamic Pressure on the Aeroelastic Response of the Single Stack IAD Design at 30^o Angle of Attack</u>

Conduct aero-structural and dynamic simulation of single stack toroids IAD design at 30^o angle of attack and bank angle rate of 5 deg/sec^2. The aeroelastic simulations will be conducted at different dynamic pressures. There are three subtasks to be performed in this simulation:

1. Conduct rigid body steady flow simulation of the single stack toroids IAD at 30^o angle of attack and no dynamic motion. The simulations will be conducted at different dynamic pressures to compute the aerodynamic flow field characteristics that are used as the initial conditions of the aeroelastic simulations.
2. Conduct aeroelastic and dynamic simulation of the single stack toroids IAD at 30^o angle of attack, bank angle rate of 5 deg/sec^2, and different dynamic pressures. Simulations will be carried out for 4 seconds.
3. Conduct aeroelastic simulation of the single stack toroids IAD at increasing aerodynamic loads to determine the failure point of the model.

The model and results of Task 5 simulations are discussed in details in Chapter 8 of this report.

Task 6: <u>Documentations and Deliverables</u>

A final report will be prepared and will document all the work done under the above described tasks. The final report will include the following;

- A brief discussion of the analysis methodology

- A description of the analysis input information which was used to produce the analysis results
- A description and discussion of the simulation results
- Graphs, flow field pictures and other such information which describe the details of the flow field.

Additionally, periodic interim oral reports in the form of either MS PowerPoint slides or MS Word document will be prepared and delivered to NASA for discussions.

2 GEOMETRY MODELING AND GRID GENERATION

The geometrical details of the MIAS model received from NASA are shown in Figure 2. The model has an outside diameter of 23 meters and central adapter of 3.6 meters. The inflatable Braking Unit (IBU) consists of a total of 23 pressurized internal toroidal cells covered with a smooth shield surface. The diameter of every toroidal cell is 0.92 meters. A rigid front shield is also shown in the figure with a diameter of 8.0 meters.

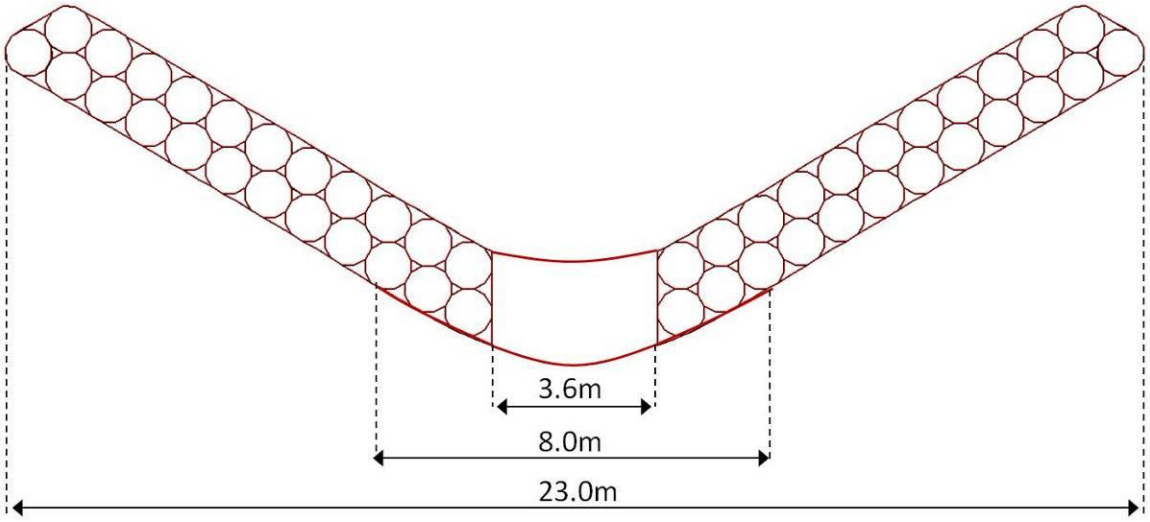

Figure 2. Geometrical details of the MIAS model

In this study, two different configurations were analyzed viz., the nominal double stacked configuration shown in Figure 2 and a single stack configuration with only one row of toroids. For each configuration, CFD-GEOM, a geometry modeling and grid generation software was used to create the geometry and grid. The nominal and modified IAD models were created as part of Task 1 and Task 4 respectively. The three-dimensional topology and grids for nominal and modified IAD configurations are discussed below.

2.1 Computational Grid Model for Double-Stacked IAD Configuration

The computational grid model of the MIAS was developed using the grid generator CFD-GEOM. The overall computational grid is modeled using 60 zonal blocks containing about 3.6 million grid cells. The outer boundaries of the computational grid are shown in Figure 3. As shown in the figure, the computational grid model of the MIAS is overset over a background grid to enable the dynamic bank maneuvering. The surface overset grid of the MIAS model is shown in Figure 4. The grid over the geometrical symmetry plane is also shown in the figure. The grid is fine enough for Euler solution and is clustered around the body to sharply capture the expected bow shock around the body. The overset grid of the MIAS model is built with a 42 zonal blocks consisting of about 2.4 million grid cells.

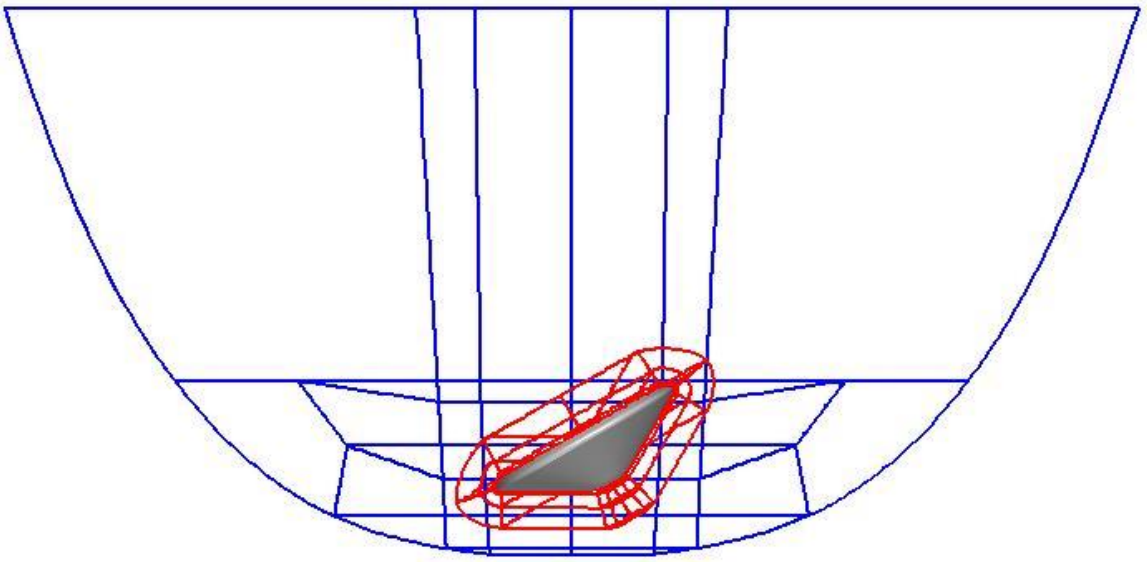

Figure 3. Overall computational grid boundaries of the double-stacked design.

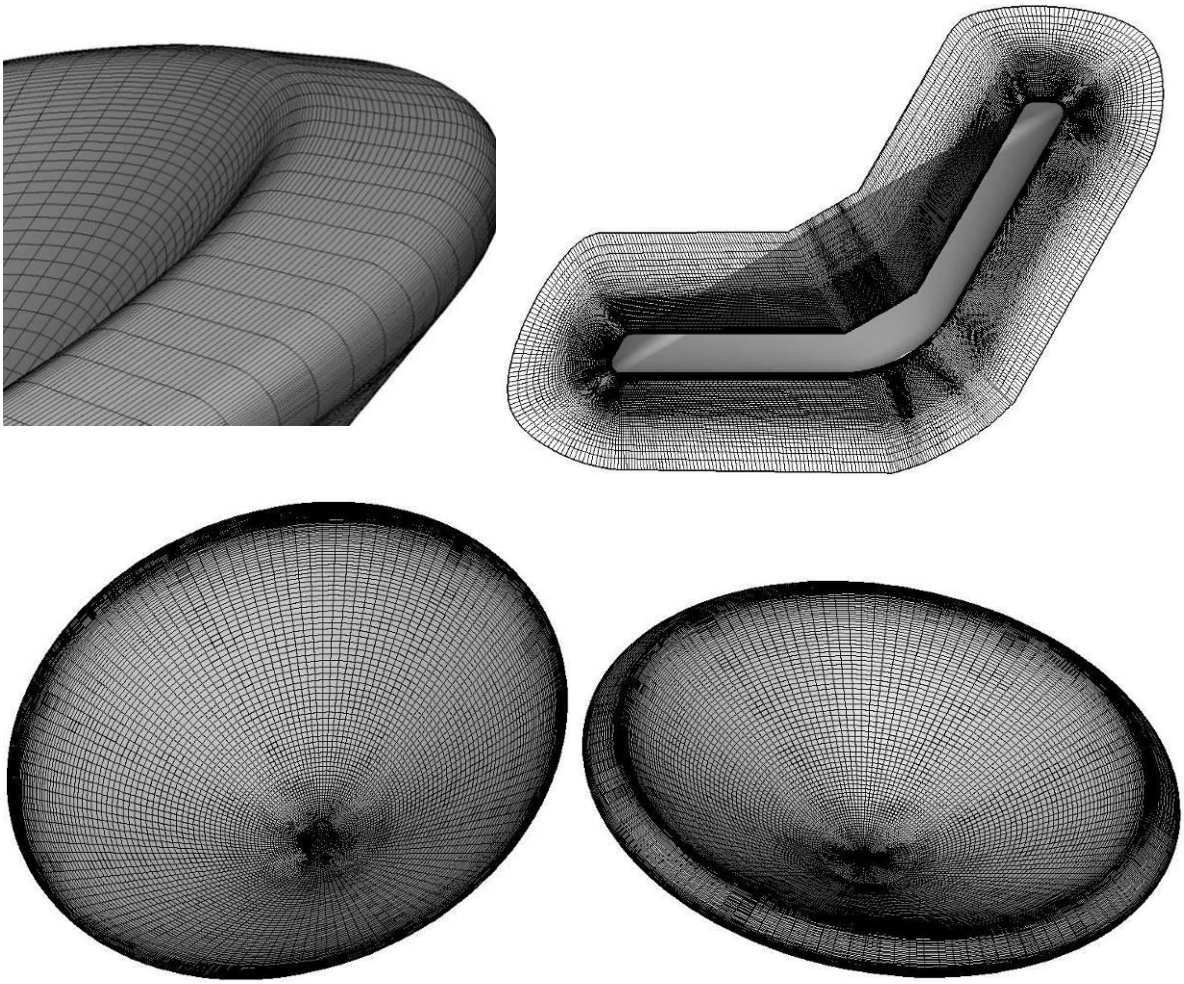

Figure 4. Computational 3D grid of the MIAS overset grid model for the double-stacked design.

The background grid is shown in Figure 5. The figure shows how the MIAS grid is overset the background. A close up view of the grid oversetting is shown in Figure 6. The background grid model was developed using an equivalent spacing for better Chimera interpolation near the outer boundaries of the overset grid. The background grid model is built with an 18 zonal blocks consisting of about 1.2 million grid cells. Although the geometrical model is symmetric, the computational grid was developed and the simulations were conducted on a full 360 degrees three-dimensional model due to the dynamic maneuver that will be considered in the subsequent chapters.

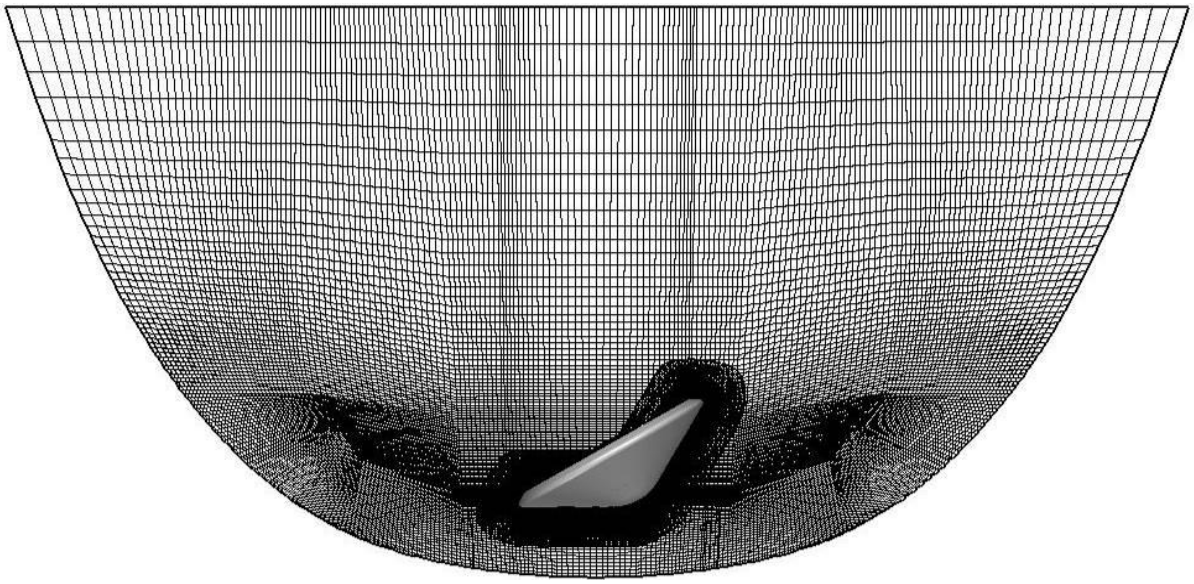

Figure 5. Three-dimensional background grid model for the double-stacked design.

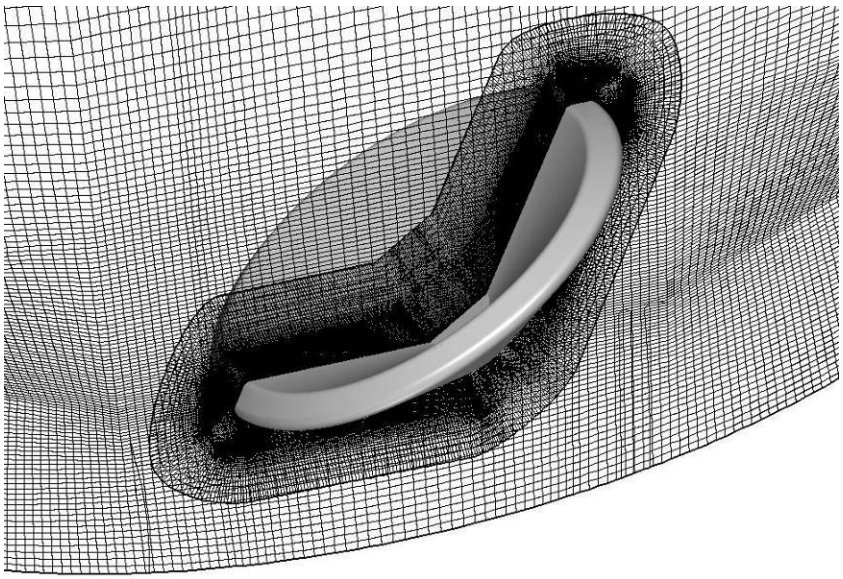

Figure 6. Close up view of the overset grid over the background grid.

2.2 Computational Structural Dynamics Model for Double-Stacked IAD Configuration

The computational structural dynamics FEM model of the nominal double stack MIAS configuration is shown in Figure 7. The model consists of 32,490 quad shell elements of non-zero thickness. A cut across the model showing the details of the model is also shown in the figure. The toroids are modeled with 12 quad shell elements each. The toroids are connected together through one of the 12 elements, and they are also connected with the gores (the outside skin) through on segment. The details of the geometrical FEM model are shown in Figure 8. In this model, the thicknesses of the model are exaggerated for clarity.

The toroids are made of Kevlar and the gores are made of Upilex. The material properties of the Kevlar and the thickness of the toroids are shown in Table 1. The material properties of the Upilex and the thickness of the gores are shown in Table 2. A high temperature knock down factor of 0.5 is used for the toroids modulus of elasticity. The toroid thickness is 13.178 mil and the thickness of the gores is 26.536 mil. The original structural model of the MIAS configuration includes six circumferential straps along each of the toroids, in addition to 18 radial straps holding the model together. These straps are not modeled in the initial FEM model and will be considered in the modified FEM design model.

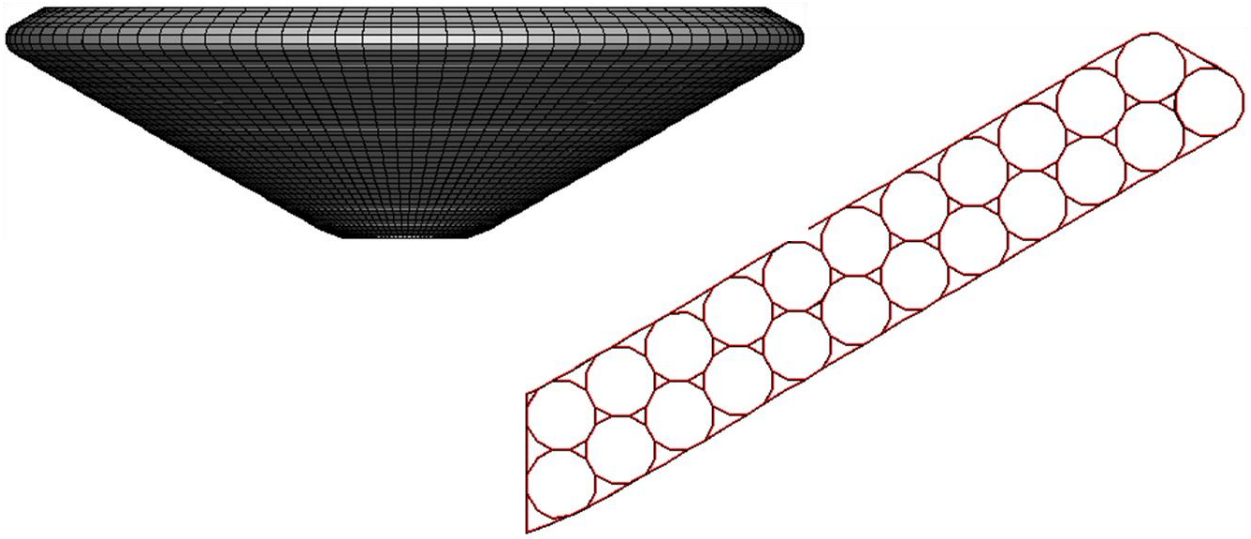

Figure 7. Computational FEM model of the double stack MIAS configuration

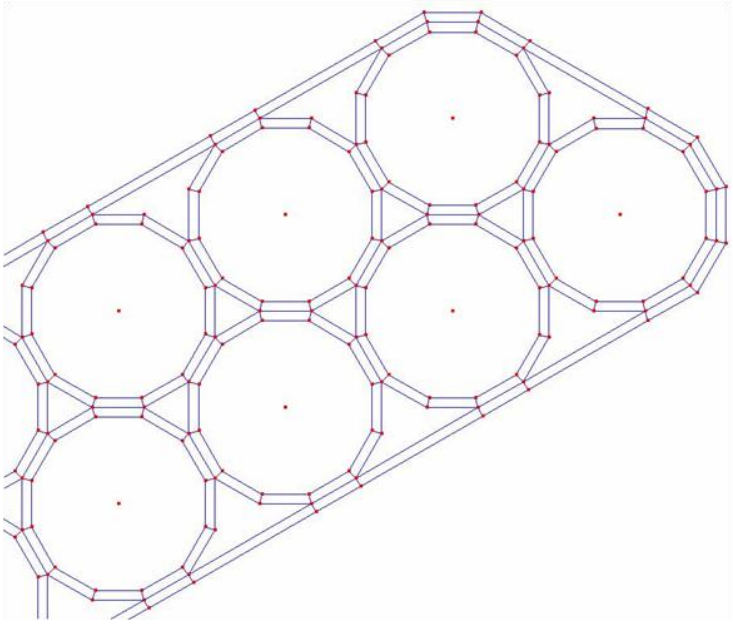

Figure 8. Details of the FEM model assembly (thickness exaggerated).

Table 1. Material properties of the toroids for the double stack IAD configuration

Kevlar Properties for Toroids	
Max E	70 E+09 Pa
Design E	35 E+09 Pa
Density	1440 Kg/m^3
Poisson ratio	0.1
Toroids thickness	13.178 Mil

Table 2. Material properties of the gores for the double stack IAD configuration

Upilex Properties for Gores	
E	3.7 E+09 Pa
Density	1470 Kg/m^3
Poisson ratio	0.34
Gores thickness	26.536 Mil

2.3 CFD Flow and Flight Conditions for the IAD Configurations

The same flow and flight conditions were used for all the cases simulated in this study. These conditions are presented in Table 3.

Table 3. Flow and flight conditions for the simulations

Parameter	Value		Parameter	Value
Time (sec)	2.183000000e+02		G-Load (earth g's)	3.701706979e+00
Altitude (m)	2.674990635e+04		Pressure (N/m^2)	3.771500270e+01
Density (kg/m^3)	1.301150987e-03		Dynamic Pressure (N/m^2)	5.143675033e+03
Temperature (K)	1.768426264e+02		Bank Angle (deg)	1.087088056e+02
Atmosphere Relative Velocity (m/s)	2.811822563e+03		Angle of Attack (degrees)	30.0

2.4 Aerodynamic Forces and Reference Quantities

The pressure signal over the surfaces of the IAD model was integrated to compute the aerodynamic forces. The sign and directions of the aerodynamic forces and moments are shown in Figure 9. The moment reference point is about 9.2 meters from the nose of the model. The moment is positive in the counter clock wise direction. The aerodynamic moments are normalized with respect to the model reference length of 23.0 meters. The reference area is 415.475 m^2, and the reference dynamic pressure is 5143.675 N/m^2. The reference quantities are summarized in Table 4.

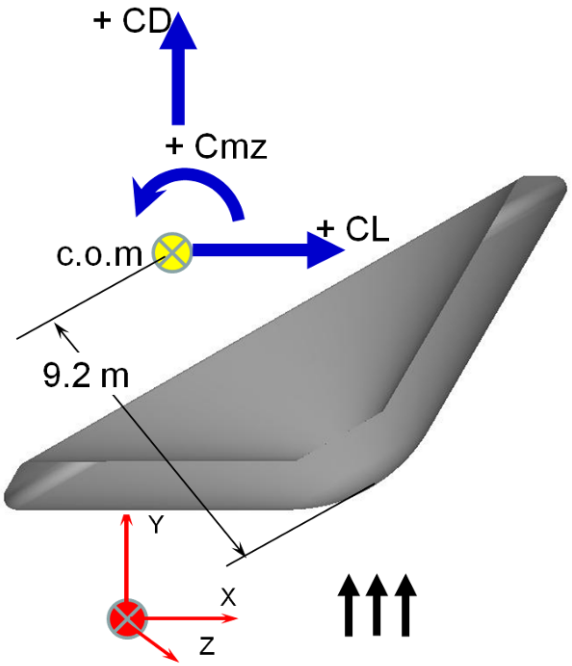

Figure 9. Sign convention of the aerodynamic forces and moments.

Table 4. Reference conditions for the aerodynamic forces and moments

Parameter	Value (metric)
S_{ref}	415.475 m^2
L_{ref}	23.0 m
x_{mrc}	0.0 m
y_{mrc}	9.2 m
z_{mrc}	0.0 m
Q_{ref}	5143.675 Pa

3 COMPUTATIONAL METHODOLOGY

The Multi Disciplinary Integrated Computing Environment (MDICE[1,2]), developed by CFDRC for Air Force Research Lab and NASA, was used for the coupling between the fluid CFD solver and structures dynamics FEM solver. The CFD solver used in this project was the density-based flow solver; CFD-FASTRAN.[3] The FEM solver used was the FEM module of CFDRC's Computational Physics (CoPhy) solver.[4]

3.1 CFD Solver – CFD-FASTRAN

CFD-FASTRAN, a commercial well validated flow solver originally developed by CFDRC, solves the Euler or full Navier-Stokes equations in a general curvilinear coordinate system employing finite-volume methods. The flow solver supports structured / unstructured, hybrid, multi-block, blocked and chimera grid systems, with automatic hole cutting for Chimera grid systems. CFD-FASTRAN is applicable for steady-state calculations or time-varying solutions and includes a built-in 6-DoF module for multiple interdependent moving body dynamic calculations. Several turbulence models are supported in CFD-FASTRAN, including the high Reynolds number k-ε with wall functions, Spalart-Allmaras, Baldwin-Lomax, Menter-SST and the k-ω turbulence models. Both flux-vector and flux-difference splitting schemes are employed with higher-order limiters.

The initial conditions for most of the cases were the undisturbed uniform free stream conditions everywhere at 30-degree angle of attack. In some cases the flowfield was restarted from constant free stream conditions except in localized regions (e.g. close to the surface) where pressure and velocity modification were made to allow the solution to smoothly transition from startup to convergence. The initial local pressure close to the IAD surface was increased to allow the shock to form outside the cup without causing solution diverging.

Cases started from free stream conditions were begun first order and run until the forces were not changing by a significant amount. Roe's flux difference splitting was used for spatial discretization of all equations. All flux limiting was done with the min-mod limiter.

All walls were modeled initially as slip adiabatic boundary conditions. The inflow and outflows used Riemann Invariants. CFD-FASTRAN detects when an outflow is supersonic and uses a more appropriate simple extrapolation in this case. The fluid was modeled with reacting CO2 properties.

CFD-FASTRAN has been validated for numerous supersonic and hypersonic flow predictions similar to the flow considered under this project.[5-10]

3.1.1 Computational Chemistry Model for Mars Atmosphere

The Martian atmosphere contains mostly CO2 which decomposes into CO and O across the hypersonic bow shock wave. Because of the shock layer chemical reactions, the post-shock specific heat ratio is lowered which significantly affects the shock stand-off distance. For the proposed preliminary design aero-elastic analysis, the computational expense of a chemically

reacting CO2 model is undesirable and unnecessary. The correct shock standoff and post-shock gas flow conditions (pressure, dynamic pressure, etc.) must be obtained for correct fluid-structure dynamic effects. The details of the gas composition may be important for surface heating effects, but are not a first order concern for the present work.

Few simplified chemistry models are analyzed to replace the fully reacting CO2 modeling. One model is perfect gas CO2 model with an equivalent gamma (ratio of specific heats) tuned to result in the correct shock jump prediction. The thermodynamic properties used for the equivalent perfect gas case are identical to standard carbon dioxide (transport coefficients and universal gas constant). One model is for a specific heat ratio of 1.33 that is based on pre-shock speed of sound. However, since the specific heats are function of temperature, post-shock properties are different than pre-shock properties. As the temperature increases behind the shock, so is gamma (specific heat ratio) and therefore post-shock values will be different.

Another model is based on a specific heat ratio of approximately 1.15 that is used to modify the values of Cv and Cp. The new value of the specific heat ratio is obtained such that the shock stand-off distance for the perfect gas case is similar to the one obtained for non-equilibrium reacting gas. The value of the equivalent gamma is determined with simple one dimensional normal shock relationships for the selected flight condition along the stagnation line.

In order to select the correct model for the analysis, an axi-symmetric simulations of a more detailed CO2 5-species reacting flow was conducted as part of Task 1. The axi-symmetric pressure distribution over the model is shown in Figure 10. Two more axi-symmetric simulations were conducted using the equivalent specific heat ratio of 1.33 and 1.15 for comparison. The pressure distributions from these simulations are also shown in the figure. The figure shows clearly that the model that takes into consideration the post-shock properties is more accurate and closer to the reacting CO2 model.

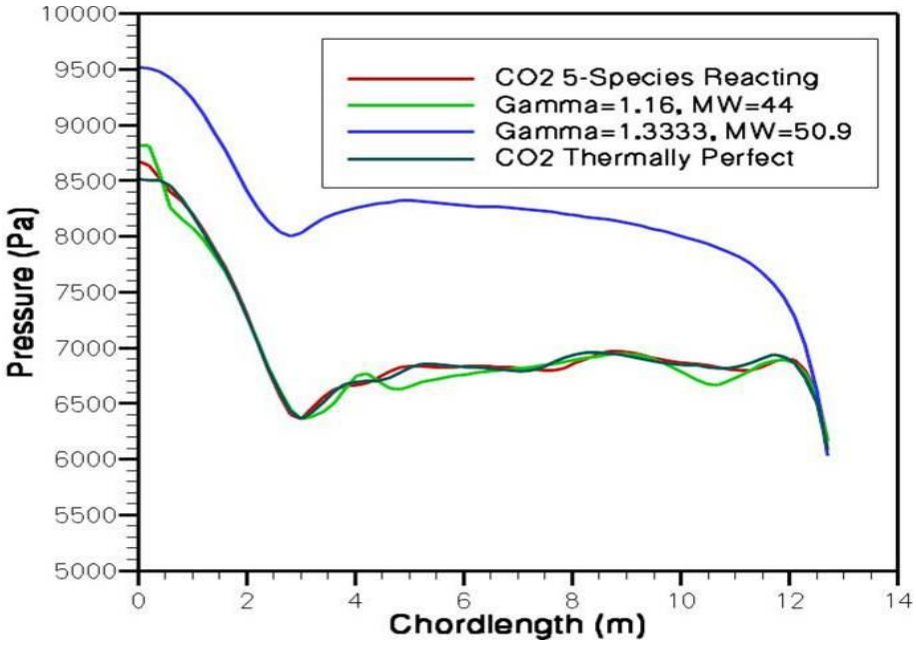

Figure 10. Axi-symmetric solution comparisons between different Chemistry models

Another simulation was also conducted using a thermally perfect CO2 model (single specie mixing of CO2) with a curve fit for specific heat Cp from Chemistry data bases. The pressure distribution for an axi-symmetric simulation using this model is also shown in Figure 10. The figure shows that the thermally perfect CO2 model gives almost similar results as the reacting gas model. The reason is that the reacting case showed that the chemical reactions are small and almost all the effect comes from the dependent of specific heat on temperature.

3.2 FEM Solver – CFDRC-FEM

CFDRC's FEM code used in this project is part of a multi-physics and multi-scale computational physics (CoPhy) software package, written in the object-oriented language C++ and developed by CFDRC. It contains several modules including: pressure-based CFD, heat transfer, structures dynamics, electrostatics, chemistry, and several others. Each module solves physics on the same or different grids, and data exchanges between different modules are seamless. The code was successfully used to model tightly coupled aerothermoelastic problems of hypersonic vehicles.[11] Only the finite element module or CFDRC-FEM was used in this project. Further information and validation for CFDRC-FEM is provided in Appendix A.

CFDRC-FEM solves stress/deformation, and acoustic in a Lagrangian frame. The most relevant features of CFDRC-FEM are:

- Both explicit and implicit FEM solver available for different time-scale applications;
- Unstructured mixed element grids including tetra, hexa, pyramid, prism, octree;
- Accurate finite elements such as mixed formulation for incompressible materials, and locking-free shell formulation and solid-shell formulation applicable for both smooth and folded shell structure;
- Multi-rigid body dynamics with various joints and its implicit coupling with flexible bodies;
- Various non-linear material models such as hyperelasticity, viscoelasticity and elastoplasticity;
- Various surface interaction such as Contact-impact algorithm, tied-interface to connect domains with different mesh;
- Acoustic model and its implicit interaction with structural dynamics;
- Capable of calculate large structured/unstructured mesh movement in the fluid domain;
- Efficient large-scale parallel computing with interface to Petsc solver;
- Seamless coupling with fluid dynamic module and heat transfer module.

Problems involving thin shell elements with large aspect ratios are extremely hard to solve with implicit solvers due to the difficulty of inverting ill-conditioned matrices. The usage of explicit solvers is cost-prohibitive due to the fact that the time step is driven by the small thickness. Therefore, we have used the mass scaling technique for shell elements involving explicit transient analysis. This scaling permits large critical time step size without loss of stability, which is particularly necessary for very thin shell structures.

In CoBi-FEM, the triangular and quadrilateral shell elements are used with linear interpolation function, therefore the translational masses at elemental node I is

$$m_u^I = \int_A \int_h \rho_0 N^I (1+\zeta) dA d\zeta$$

The rotational masses are computed by the scaling at the node I by a factor α

$$m_r^I = \alpha \int_A \int_h \rho_0 N^I (1+\zeta) \zeta dA d\zeta$$

where A and h are the area and the thickness of the element, respectively, and the scaling factor of $\alpha = 1.5A/h^2$.

3.3 MDICE Infrastructure

MDICE provides an environment that handles the transmission of data between different physical or multi-physics modules across networks and computing platforms. A fluid structure interaction problem can be performed between different sets of CFD and CSD codes as seen in Figure 11.

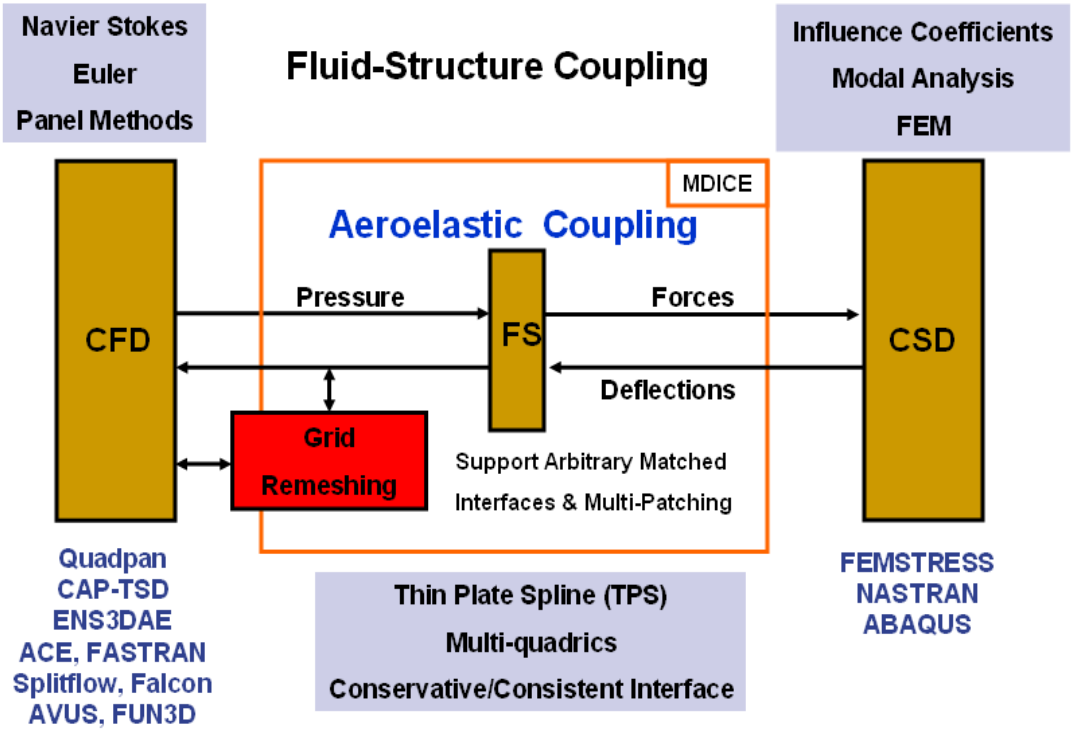

Figure 11 MDICE fluid structure interaction scheme.

Data transmission occurs through memory; therefore even a simulation composed of separate analyses and distributed across a heterogeneous network appears as a tightly coupled code. Existing analysis codes are integrated through an object-oriented application programming

interface (API), ensuring that modern technology can readily be implemented into the simulation process. The simulation modules integrated into the MDICE environment must only be modified to deliver and receive data and information from the MDICE system. MDICE has a full interface for codes written in F77, F90, C, or C++. Modules are 'MDICE-compliant' once their subroutines have been equipped with appropriate MDICE calls for sending and receiving information. The code module must then be linked to the MDICE library and recompiled. A code module can also be made compliant without any modifications, but with much reduced efficiency, by having the MDICE wrapper script invoking module execution in a file-based mode (disk I/O).

Once all necessary modules are integrated (deemed 'MDICE-compliant'), analyses are coordinated in a multidisciplinary simulation through a scripting language. The disciplinary analyses are initiated from within MDICE. Each analysis loads grid and restart information and then releases execution control to MDICE. Once each module is placed in a wait mode, the simulation is run through the scripting language, which is executed through the MDICE GUI. The first command usually issued to each module creates an interface object within MDICE. An interface object stores pointers to the grid and variable information that resides directly in the analysis modules' memory. Following, MDICE assembles the interface objects, or performs calculations necessary for the interpolation of quantities between the disciplinary grids.

MDICE framework has been used successfully for numerous aeroelastic applications. The most prominent is prediction and control of F/A-18 aircraft that is recognized by "Aerospace America" magazine as one of the yearly achievements in 2002.[12-14] MDICE was also used to model and analyze different inflatable structures.[15,16]

Currently supported MDICE Applications include:

- Distributed Computing: Codes May Be Run On Different Unix Or Windows Workstations
  - Parallel, Distributed Execution Of Code Solution
  - Network Of Heterogeneous Computer Systems (Mix Of Unix And Windows Computers)
  - Multi-Level Parallelism
- Fluid-Fluid Interfaces: Flow Solvers Coupled With Other Flow Solvers
  - Code-To-Code Coupling: Incompressible To Compressible, Pressure-Based To Density-Based
  - Arbitrary Grid Coupling And Alignment (e.g. Structured To Unstructured Grids)
  - Multi-Dimensional Coupling (e.g. Axi-symmetric to 3D, 2D to 3D)
  - Mixing Plane Interfacing (Circumferential Averaging)
- Fluid-Structure Interfaces: Communication Between Flow And Structural Solvers
  - Conservative And Consistent Interfacing (Force And Virtual Work Conservation)
  - Arbitrary Grid Coupling (e.g. Structured Fluid Grids To Unstructured Solids Grids)
  - Multi-Dimensional Coupling (e.g. Structural Beam Models Coupled To Three-Dimensional Fluids Flow Models)
- Flow/Structural Solvers Coupled With Grid Generators
  - Direct Coupling Of Grids With Analysis Codes For Optimization Problems
- Computer Aided Design Codes Directly Coupled With A Grid Generation Tool
  - Automated Remeshing Of Parametric Geometries

The MDICE environment includes three main parts:

1. Multi-Physics Simulation Controller
2. Multi-Physics Analysis Modules
3. Multi-Physics Interfacing Modules

The first part is the MDICE controller, which controls the temporal synchronization of the data transfer and the multi-level parallelism of the multi-physics analysis modules and coupling routines. The second part is a set of multi-physics fluid, thermal (under development), and structure analysis modules for the analysis of the multi-physics characteristics of a hypersonic vehicle. The third part is the multi-physics interfacing modules such as fluid-fluid, fluid-structure, thermal-solid interfacing modules. The various parts are described in the remainder of this section.

3.3.1 MDICE Controller

The first component in MDICE is a central controlling process that serves as an object repository and provides application control via MDICE specific script language and remote procedure calls. The remote procedure calls are the mechanism by which MDICE controls the execution and synchronization of the participating applications. The controller oversees several important tasks such as:

- Direct launching and stopping of application modules on specified hosts in the MDICE environment.
- Control workflow of a simulation by means of scheduling tasks to the application modules.
- Facilitate data transfer between application modules.

3.3.2 Multi-Physics Analysis Modules

The second part of the MDICE environment is a set of analysis modules for multi-physics analysis. In this project, the multi-physics modules used were CFD-FASTRAN for computational fluid dynamics, and CFDRC-FEM (CoPhy) for computational structural dynamics.

These codes can interact with each other or with any multiple numbers of codes already in the MDICE environment. Third party tools from US govt. (AVUS, FUN3D etc), public domain and commercial areas (CFD-FASTRAN, CFD-ACE, AERO-F, AERO-S, ABAQUS, Matlab etc) can and have been integrated and fully coupled with CoPhy flow and/or FEM and/or thermal solvers seamlessly.

3.3.3 Multi-Physics Interfacing Modules

The interface module consists of several interface types that let two codes communicate information between each other. A CFD code and a FEM code communicate through a fluid structure interface, a CFD code and a thermal code communicate via the fluid-thermal interface and the FEM and a thermal code can communicate via a volumetric interface. A CFD code can also talk to a different CFD code through a fluid-fluid interface. None of these interfaces requires one to one grid connectivity. The data interpolation is done in a conservative consistent fashion.

Fluid-Structure Interface

The fluid-structure interface algorithm is used to project forces from the fluid cells into equivalent forces and moments to the structure cells and to project the deflections of the structure to the fluid. In the developed environment, a conservative-consistent interfacing module is used for the fluid-structure coupling. The fluid-structure interfacing is formulated in the most general sense for maximum flexibility. There are no inherent assumptions that the fluid grid is matched with the structure grid, either through different mesh densities, mesh architecture, or through physical separation between the interfaces as seen with thick shell finite-element models.

The relevant features of the fluid-structure interfacing module are:

- 100% conservative and consistent.
- Solid forces are directly projected from the face pressure. The fluid nodal forces are translated to the solid nodes using finite-element shape functions.
- Fluid nodal deflections are directly projected from the solid nodal deflections.
- All grid alignment is automatic (accomplished by using fast ADT geometrical searching).
- Unstructured and structured grids are supported.

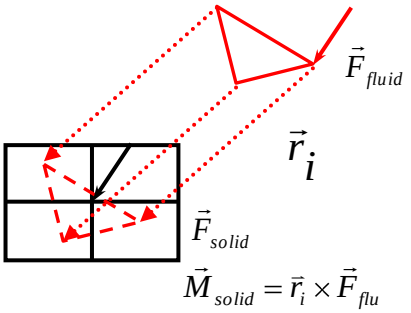

The conservation property aims to conserve the forces and moments in the interpolation process between two or more grids. In this case, the sum of all forces and moments on the fluid interface is equivalent to the sum of all forces and moments on the structure interface. Requiring that the virtual work performed by the solid interface is equivalent to the virtual work performed by the fluid interface provides the necessary consistency or virtual work conservation.

The surface grids of the CFD and CSD models of the IAD configuration are not identical as shown in Figure 12. In a typical aeroelastic analysis, the aerodynamic forces are projected into the surface then interpolated into the nodes of the FEM model using the fluid-structure interfacing module.

Fluid-Thermal Interface

The fluid-thermal interface is used to exchange heatflux from the fluid cells to the structure cells and to project the temperature of the structure to the fluid. The fluid-thermal interfacing is formulated in the most general sense for maximum flexibility. There are no inherent assumptions that the fluid grid is matched with the structure grid, either through different mesh densities, mesh architecture, or through physical separation between the interfaces as seen with thick shell

finite-element models. This interface was not used in this project but can be used in future work if the thermoelastic effects need to be simulated.

FEM-Thermal Volumetric Interface

The FEM-thermal volumetric interface is used to exchange temperature from the thermal nodes to the structure nodes and to project the displacement of the structure to the thermal nodes. The volumetric interfacing is formulated in the most general sense for maximum flexibility. There are no inherent assumptions that the fluid grid is matched with the structure grid, either through different mesh densities, mesh architecture. The disadvantage is that it is a computationally expensive interpolation. This interface was not used in this project but can be used in future work if the thermoelastic effects need to be simulated.

Fluid-Fluid Interface

The fluid-fluid interface is used to exchange conserved flow quantities between one set of fluid cells to another set of fluid cells being solved by FASTRAN. The fluid-fluid interfacing is formulated in the most general sense for maximum flexibility. There are no inherent assumptions that the fluid interfaces from each domain are matches with each other, either through different mesh densities, mesh architecture, or through small physical separation between the interfaces. The interpolated is based on conserved fluid quantities.

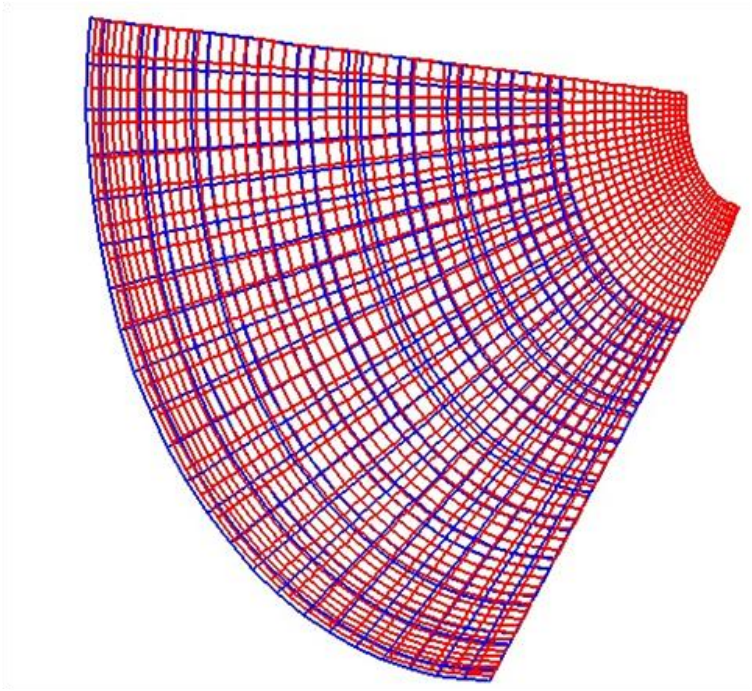

Figure 12. Surface CFD and CSD grids overlaid over each other

3.4 Coupling Methods

Various coupling methods and options were used through the course of this project to exchange CFD loads and deflections between the CFD and the Structural FEM models. The simplest

method was to divide the structural model and CFD model into a number of sections and impose the average pressure load of each CFD section to the corresponding structural boundary. This method is referred to as the "***CFD averaged constant loading***". The second method is to transfer the pressure loads from the CFD fluid structure interface to structural FSI interface using MDICE interface modules to transfer the loads in a conservative consistent manner. However, in this method, the deformations resulting from these loads are not transferred back to the CFD solver. This method is referred to as "***one-way coupling***". The final method is the full "***two-way coupling"*** in which the pressures and deflections are both exchanged.

4 STEADY AERODYNAMIC FLOWFIELD FOR THE DOUBLE STACK IAD CONFIGURATION

The previously described aerodynamic model was used to simulate the aerodynamic flowfield around the IAD configuration. The flow and flight conditions for the simulation as well as the computational models and solution methodology were presented in previous chapters.

4.1 Steady State Aerodynamic Simulation Results

The aerodynamic model described in chapters 2 and 3 was used to simulate the aerodynamic flowfield around the MIAS model at a specific set of conditions outlined in Table 3. Initially, three-dimensional simulations were conducted for both the constant specific heat ratio model and the CO2 thermally perfect model with Cp from curve fit. The effect of the chemistry model on the pressure contours over the model is shown in Figure 13. As shown in the figure, the thermally perfect model produced a shock that is closer to the body surfaces. Since the reacting CO2 chemistry model is more representative of the Mars atmosphere, this model is used for the remaining of the CFD simulations.

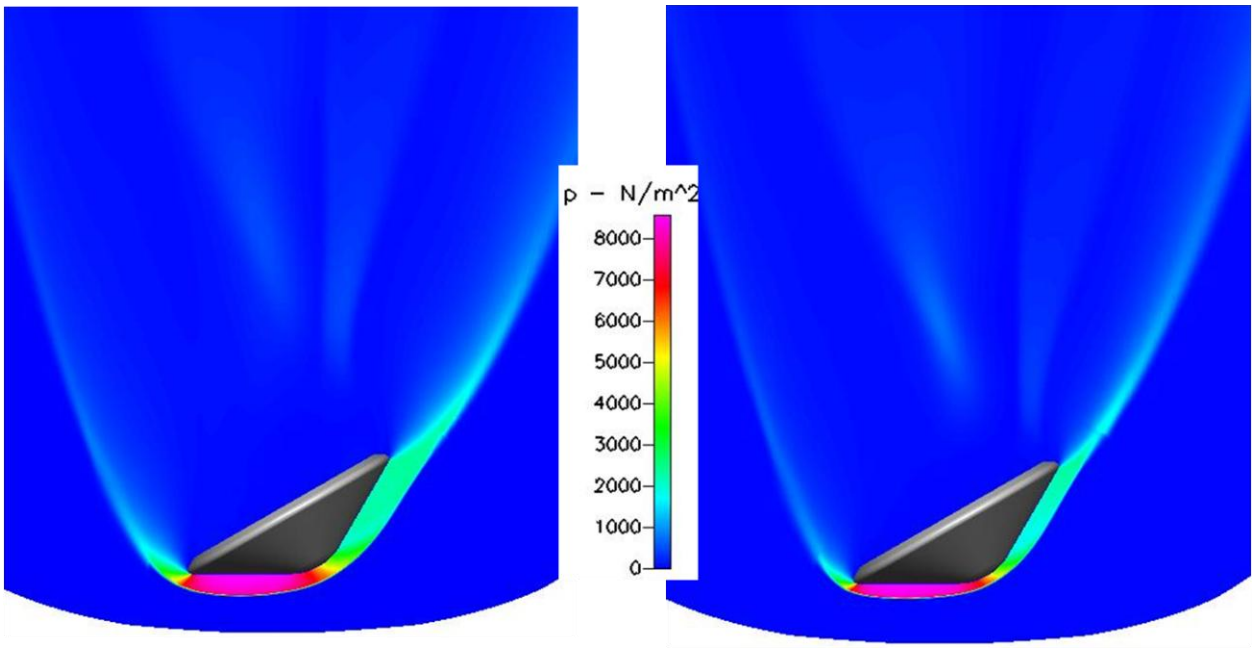

(a) onstant specific hear ratio = 1.33

(b) O2 thermally perfect model with Cp curve fit

Figure 13. Effect of chemistry model on pressure contours over the MIAS model.

The details of the flow field results for the case of reacting CO2 chemistry model (thermally perfect CO2 model) are presented next. The overall pressure and temperature contours over the symmetry plane of the whole computational domain are shown in Figure 14 and Figure 15, respectively. A maximum pressure of about 8500 Pa occurs over the front shield of the model

and in front of the oncoming flow. The Mach number contours and relative normal velocity contours over the symmetry plane of the whole computational domain are shown in Figure 16 and Figure 17, respectively.

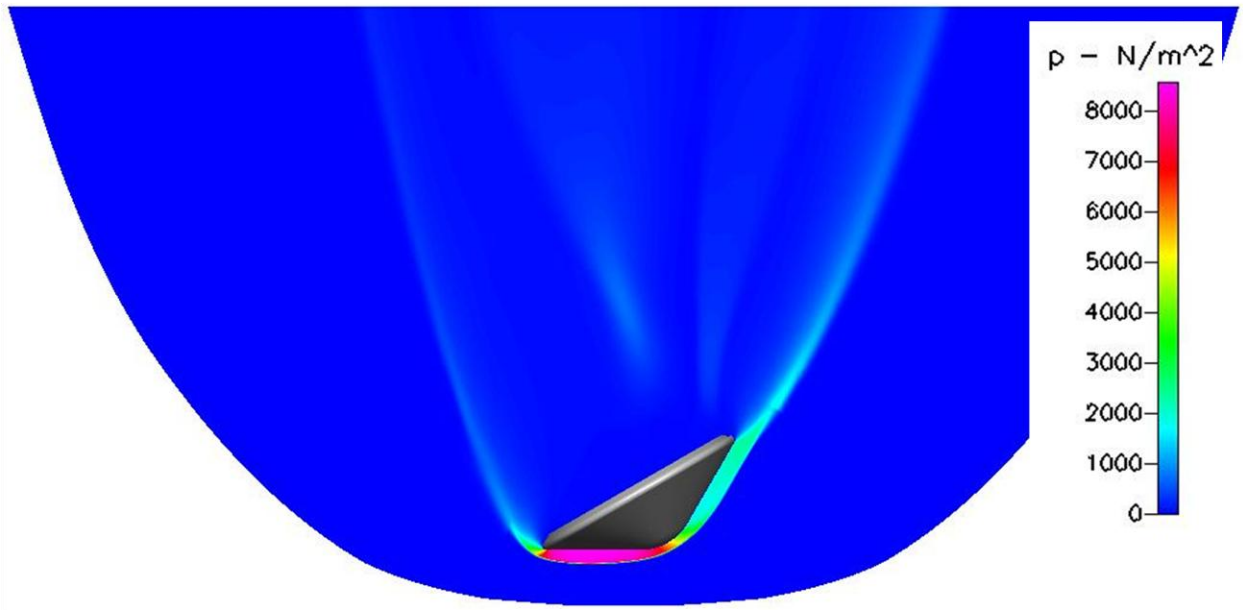

Figure 14. Steady state pressure field around the MIAS model

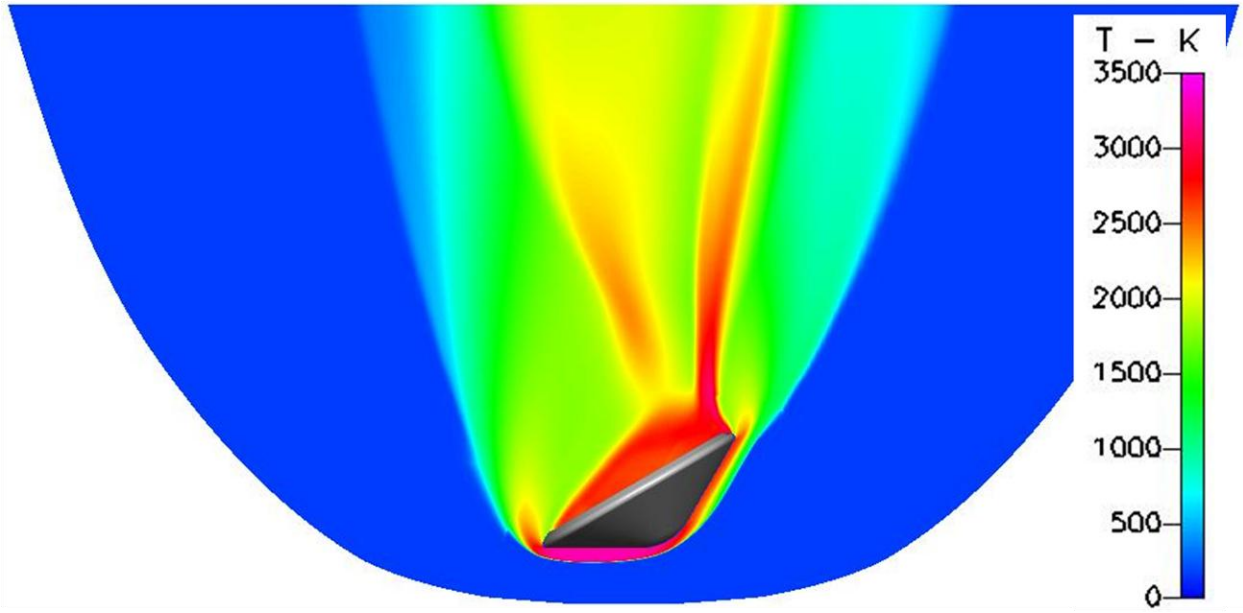

Figure 15. Steady state temperature field around the MIAS model

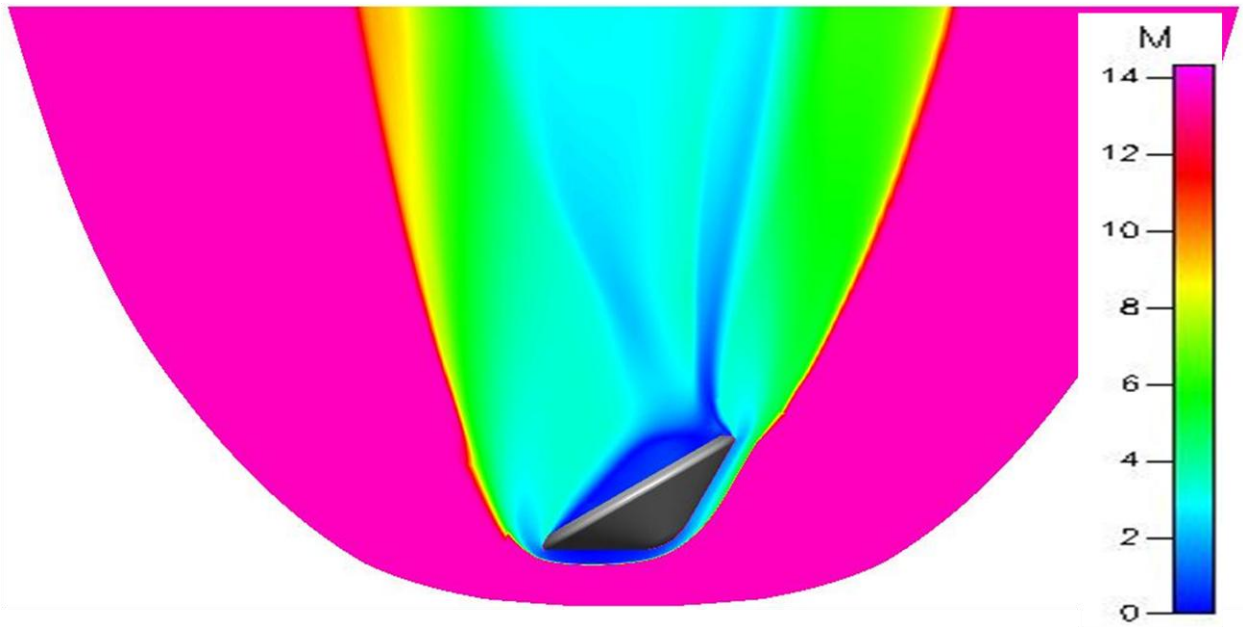

Figure 16. Steady state Mach contours around the MIAS model

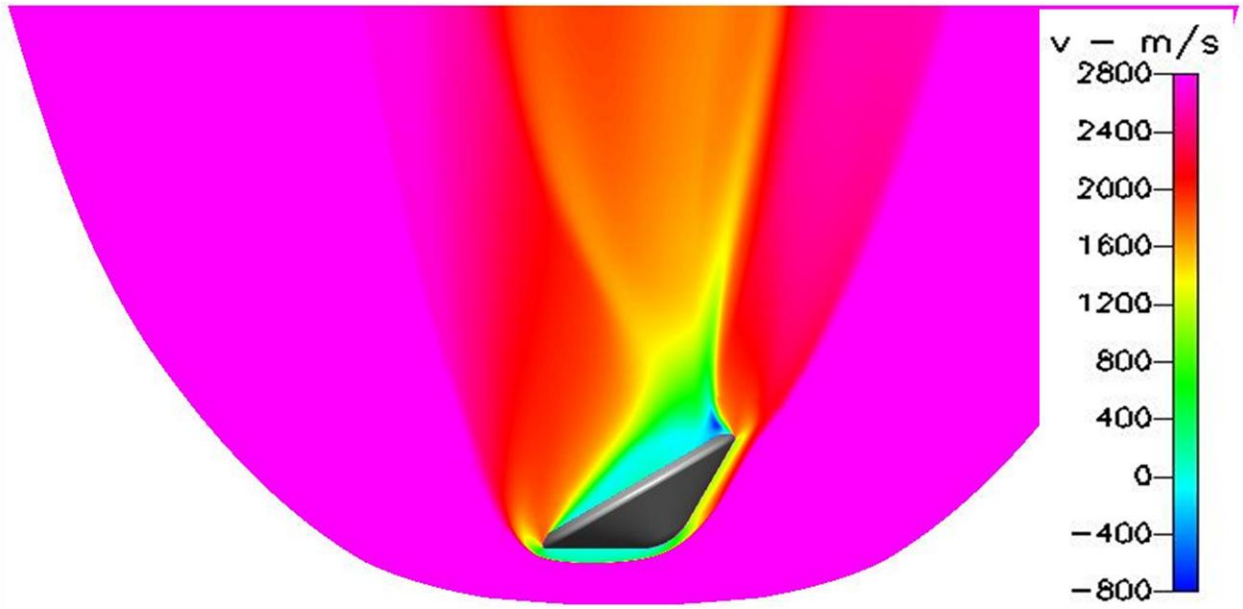

Figure 17. Steady state normal velocity contours around the MIAS model

The surface pressure contours over the front and back of the MIAS model surfaces are show in Figure 18. The maximum pressure occurs nears the windward side of the model and decreases toward the leeward side. The pressure in the back of the model is very small compared to the front side. The details of the pressure contours in the back side of the model are shown in Figure 19 with different scale for clarity. The maximum pressure on the back side of the model is about

0.02 psi and it occurs near the leeward side of the model, most probably due to flow separation from the leeward side. The surface pressure and temperature distribution along the symmetry plane of the model are shown in Figure 20. The figure shows that a fairly constant pressure occurs almost over the whole windward side before it decreases near the leeward side.

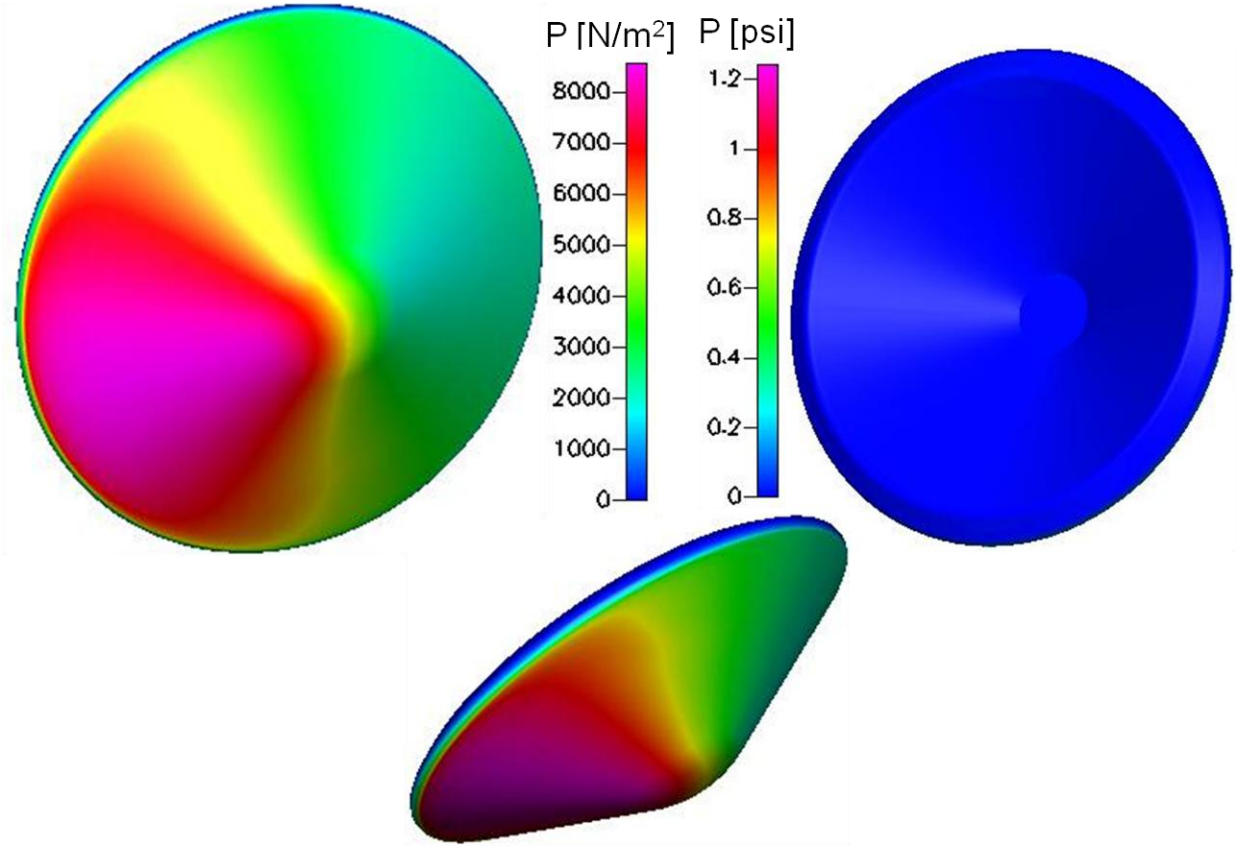

Figure 18. Surface pressure contours over the MIAS model

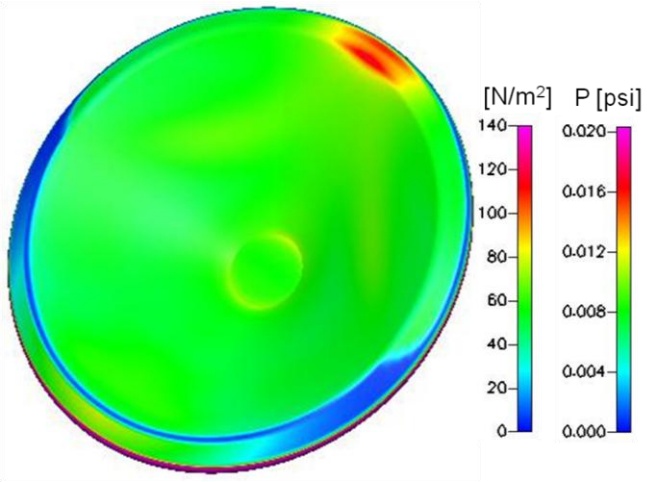

Figure 19. Surface pressure contours on the back of the model

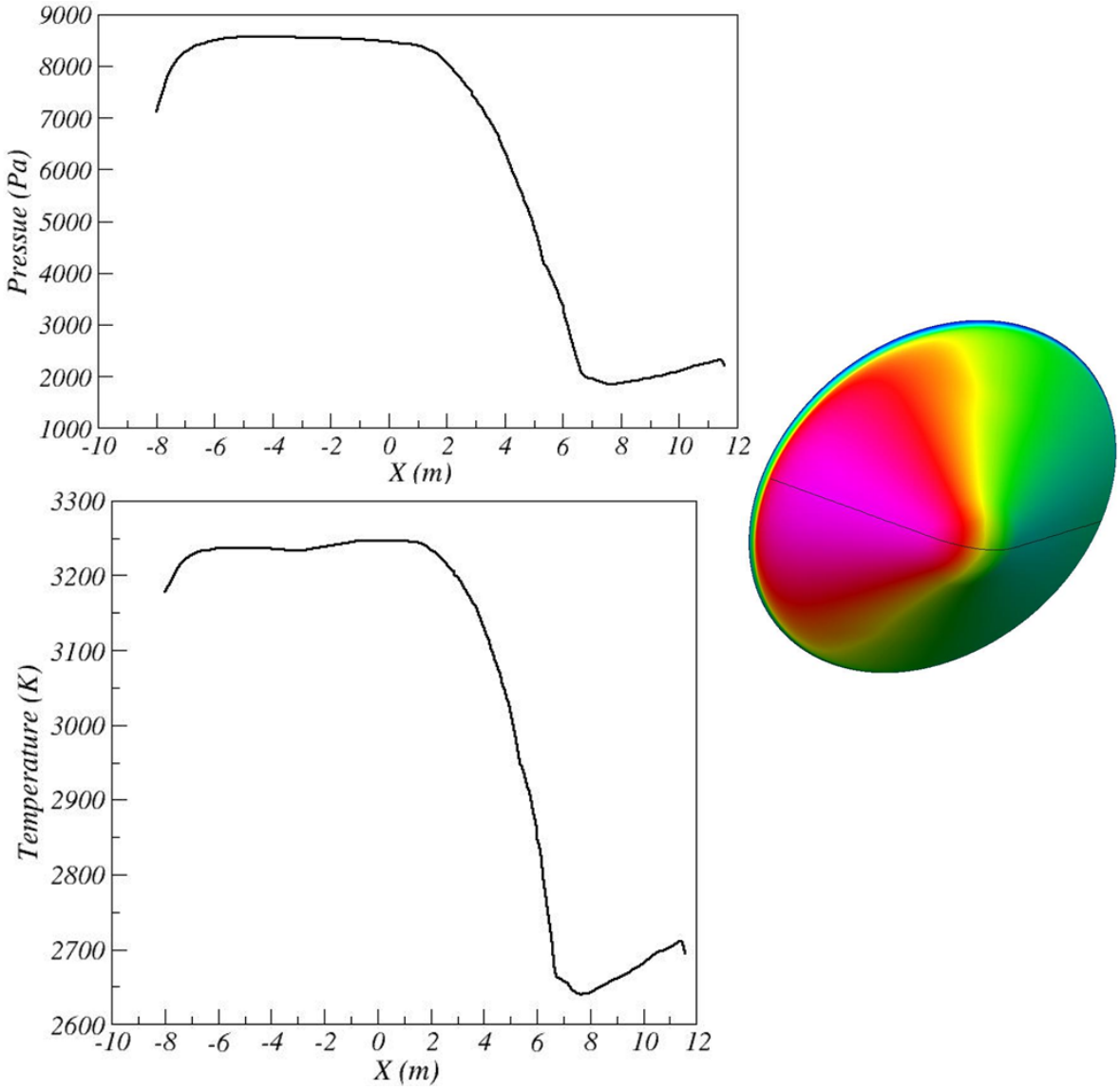

Figure 20. Pressure and temperature distribution along the symmetry plane of the model

The pressure signal over the surfaces of the MIAS model was integrated to compute the aerodynamic forces. The sign and directions of the aerodynamic forces and moments are shown in Figure 9. The history of the aerodynamic lift and drag coefficients are shown in Figure 21. The history of the moment coefficient is shown in Figure 22. The figures show that the aerodynamic forces converge well within 2000 iterations. The final value of the drag and lift coefficients are 0.869 and 0.3004, respectively. The moment coefficient converged at approximately -0.0561. A negative moment coefficient is necessary for the aerodynamic stability of the model.

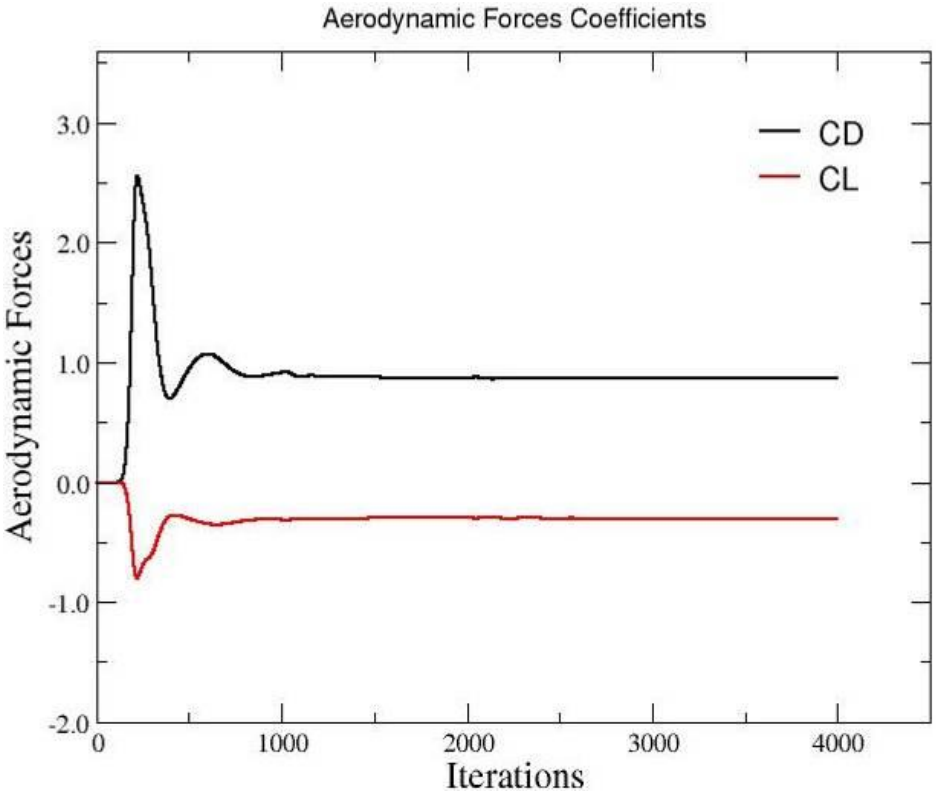

Figure 21. History of lift and drag coefficients

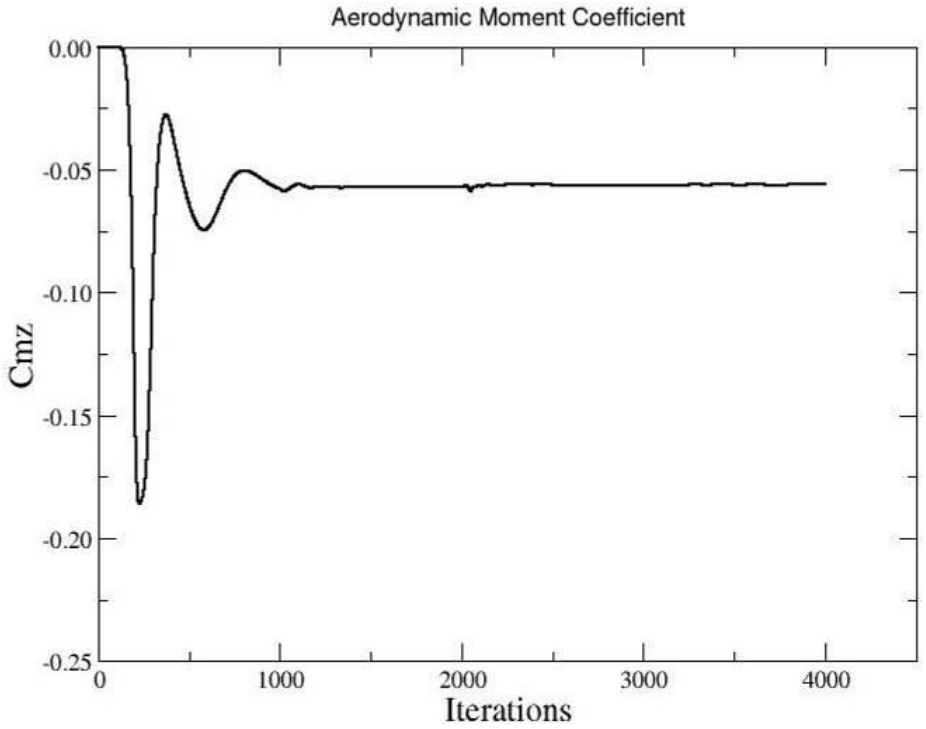

Figure 22. History of moment coefficient.

4.2 Computational Structural Analysis

4.2.1 Static FEM Analysis of the MIAS Model with Constant Loading

The model was tested first with constant loading prior to applying the predicted CFD loads. Several static FEM simulations were conducted at different inflation pressures from 15 KPa to 45 KPa. A constant loading of 5000 Pa was applied over the whole front side of the model, including the windward and leeward sides. No loads were applied at the back side of the model. The effects of the toroids inflation pressure on the peak displacement of the model are shown in Figure 23. The figure shows the results of two simulations; one at the maximum modulus of elasticity, 70 GPa, and another at the knocked-down modulus of elasticity, 35 GPa. In both cases, the modulus of elasticity of the gores is kept the same at 3.7 GPa. The figure shows a fairly exponential curve with the decrease of the inflation pressure. The model at inflation pressure of 10 KPa or less was unstable and was not able to converge. The histories of convergence of the performed simulations are shown in Figure 24.

A typical deformation contours over the model for the case of toroids inflation pressure of 15 GPa and toroids modulus of elasticity of 35 GPa is shown in Figure 25. The figure shows that the peak displacement occurs near the outer diameter of the model.

The FEM cases conducted so far were with constant loading over the model. When the predicted CFD loads were applied to the current model, the nonlinear FEM model was not able to converge and sometimes collapsed. The FEM model had to be revisited to be sure that we are not missing important details that may affect the rigidity and stability of the model.

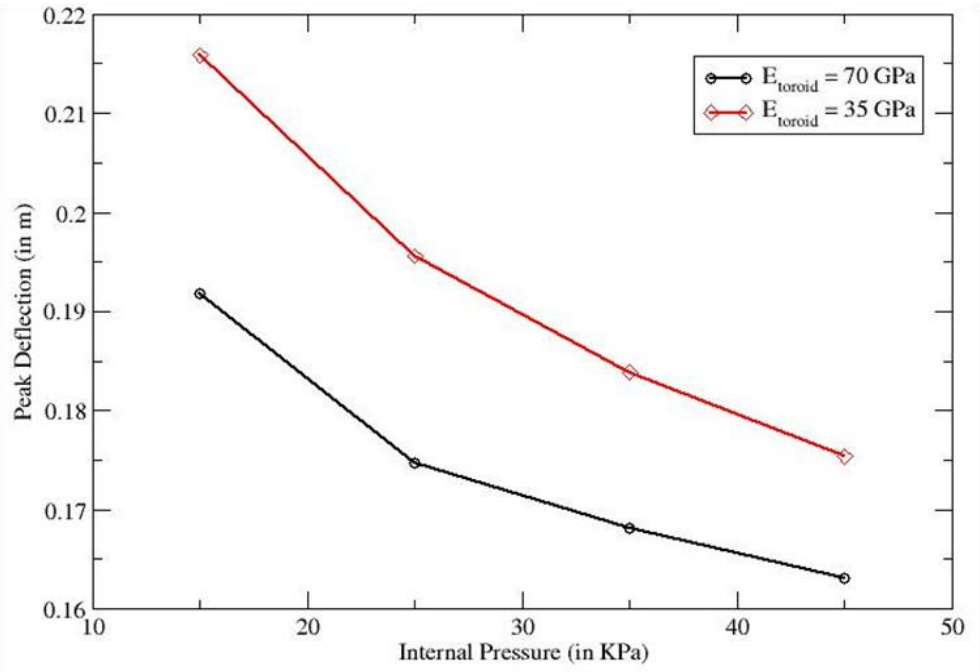

Figure 23. Effect of toroids inflation pressure on the model peak deflection

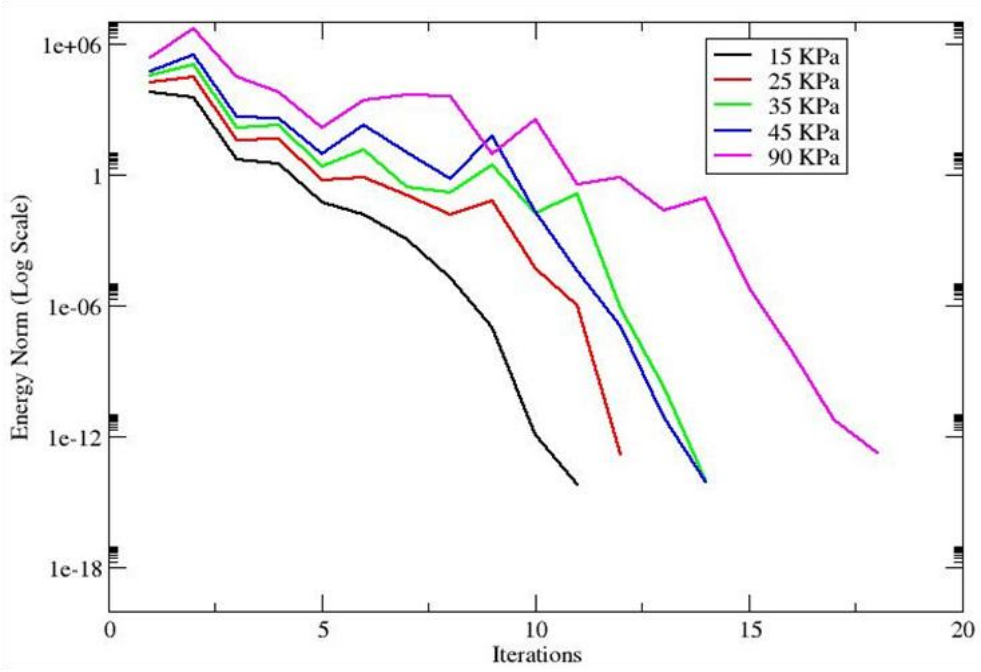

Figure 24. The convergence histories of the conducted simulations

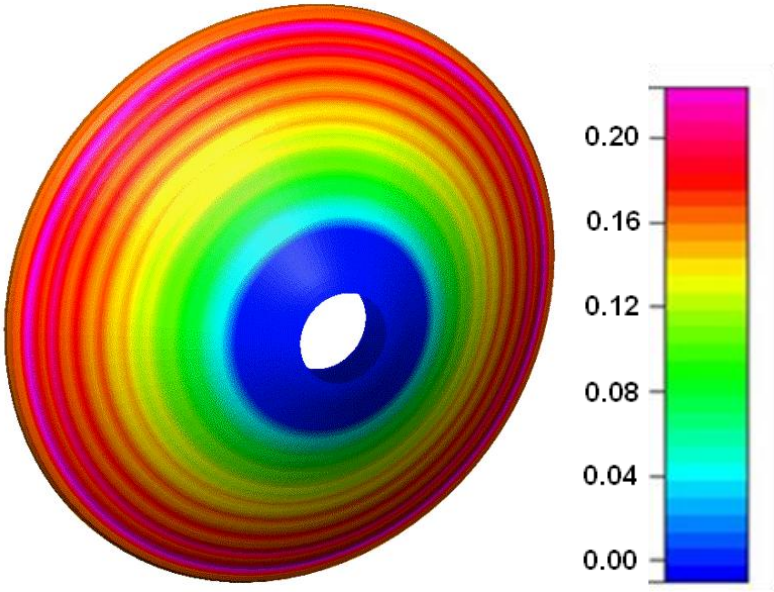

Figure 25. Deformation contours for the case of inflation pressure of 15 GPa.

4.2.2 Static FEM Analysis of the Modified MIAS Model

As mentioned in the previous section, the original FEM model was only converging when an average constant loading was applied. The simulations were not converging when the predicted CFD loads were applied over the model. Looking back at the details of the toroids, the toroids

thickness was 13.178 mil and it has 6 straps running along the major circumferential direction of the model, as shown in Figure 26. These circumferential straps were ignored in the original model. The straps are made of Kevlar with maximum modulus of elasticity of 70 GPa and Poisson's ratio of 0.1. The cross sectional area of these straps is 113.37 mm^2 each. Obviously, these circumferential straps will contribute significantly to the rigidity of the model and therefore have to be taken into consideration.

Since the axial straps are made of Kevlar which is the same material as the toroids, the FEM model can be simplified by using an equivalent toroid thickness. The equivalent toroid thickness is adjusted based on the cross sectional areas of the toroids and axial straps together. The effect of the straps cross sectional area led to an equivalent toroid model with a thickness of about 24 mil. The FEM simulations conducted in remainder of this section correspond to this modified FEM model.

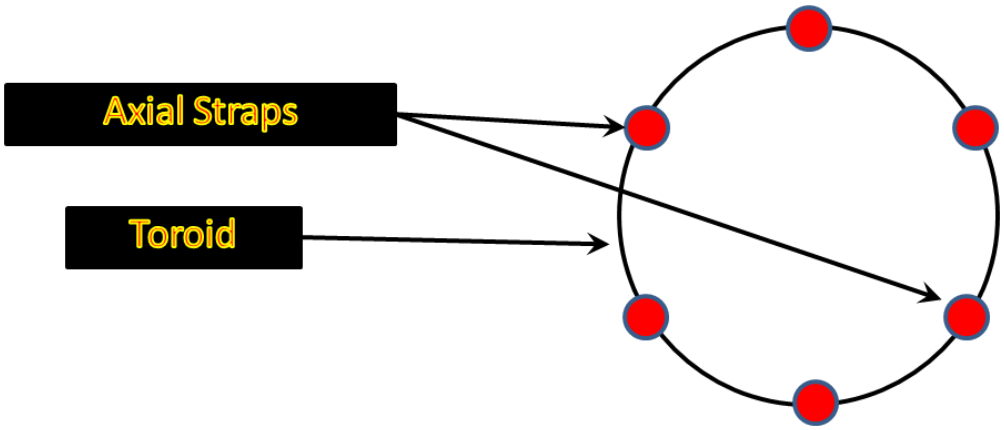

Figure 26. Schematic view showing the toroids structure with axial straps

The predicted pressures over the front shield of the model are converted into forces and projected over the surface model using the MDICE interface module. The contours of the CFD loads over the FEM model are shown in Figure 27. Several static FEM simulations for the modified FEM model were conducted at different inflation pressures from 10 KPa to 35 KPa. The simulations were conducted using the predicted CFD loads as well as accurate constant averaging loading over the model for comparison.

The effects of the toroids inflation pressure on the peak normal displacement and total displacement of the model are shown in Figure 28 for the cases using the predicted CFD loading. The total displacement is computed as follows;

$$\text{Total Displacement} = \sqrt{\delta_x^{\,2} + \delta_y^{\,2} + \delta_z^{\,2}}$$

The same series of simulations were conducted for an average CFD loading over the model. In the average CFD loading simulations, the predicted CFD loads were used to compute an average loading over the windward side and the leeward side of the model. The average CFD load over the windward side was 6706 Pa, and the average CFD load over the leeward side was 2882 Pa.

The results of the total displacements for the predicted CFD loads and CFD average loading are compared to the cases of constant loads of 5000 Pa in Figure 29. Comparing Figure 29 (the green line) to the results of Figure 23 show that the addition of axial straps reduced the displacements by about 30%. The figure also shows that the cases of the predicted CFD loads and the cases of averaged CFD loading yielded close results. The averaged CFD loading on the full front shield under predicts the total deformation in the structure. A better averaging over several patches of the model may lead to even better comparison between both cases.

The deformation contours over the front shield of the model for the predicted CFD loading and the averaged loading are shown in Figure 30 for the case of toroids inflation pressure of 15 KPa. The deformation contours over the same model, removing the front gores skin are shown in Figure 31. The topology of the deformation contours is similar in both cases with a larger region of high deformation for the case of averaged loading.

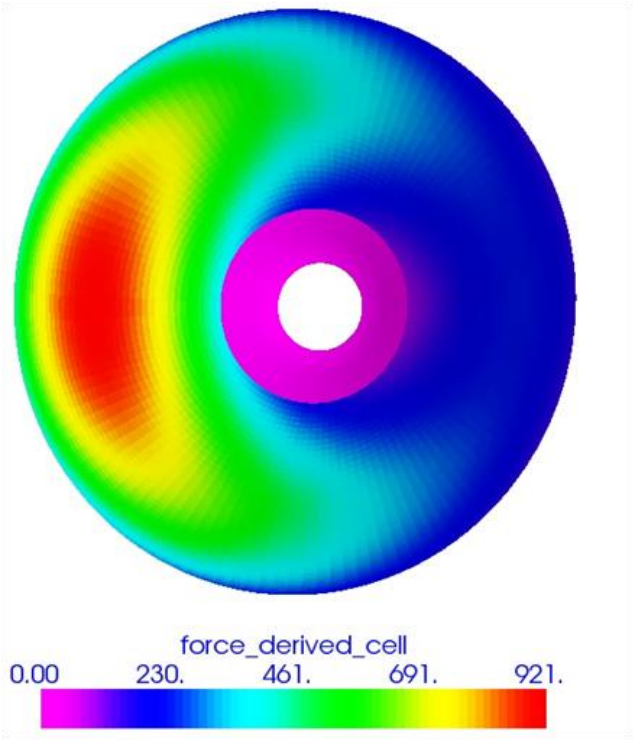

Figure 27. Predicted CFD loading over the front surface of the FEM model

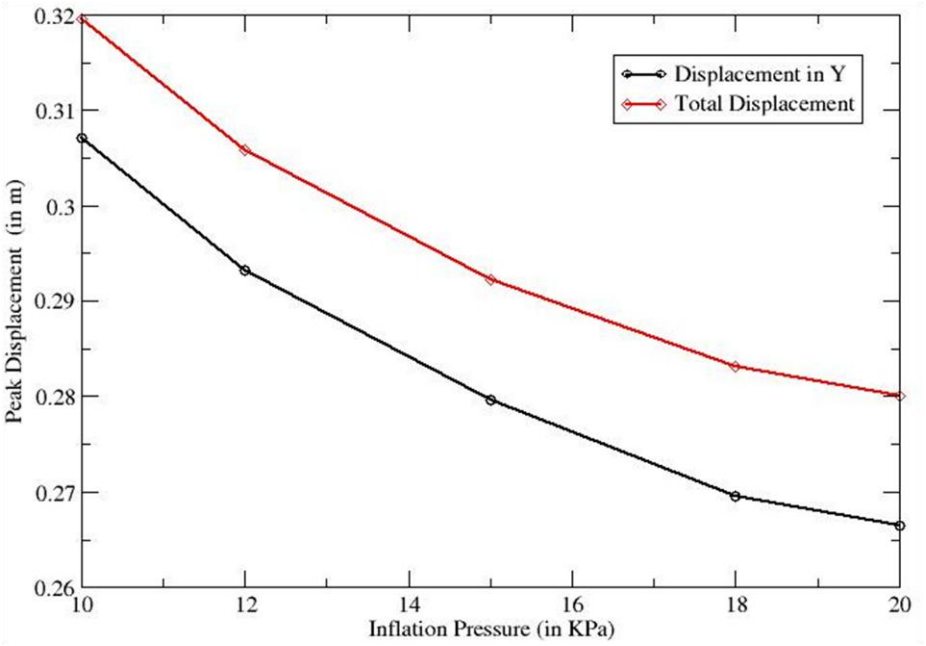

Figure 28. Effect of toroids inflation pressure on the peak displacement of the modified model

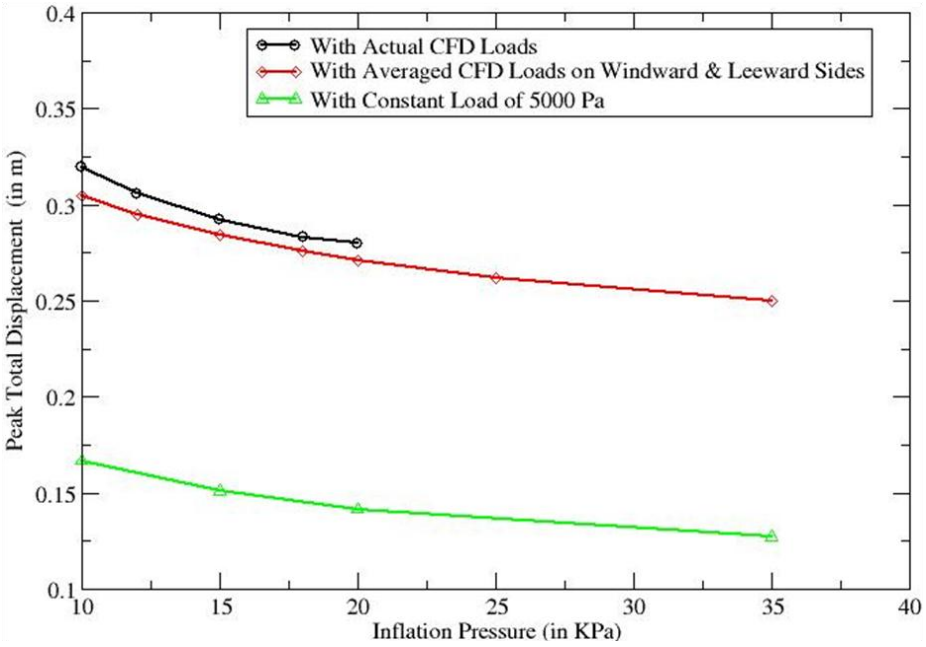

Figure 29. Peak total displacement of the modified FEM model using different loading conditions.

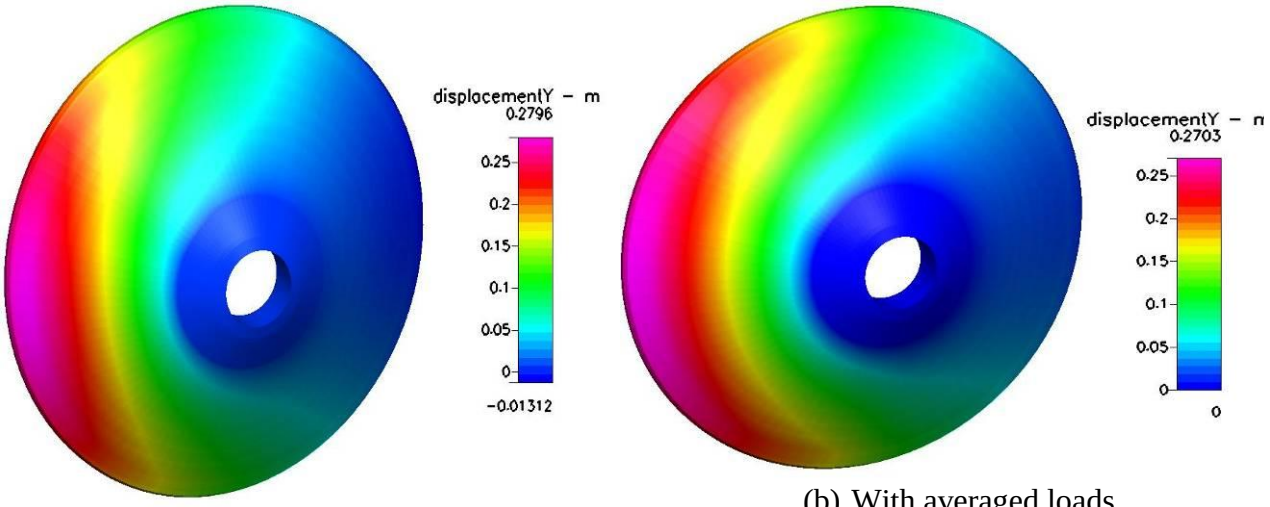

(a) With predicted CFD loads (b) With averaged loads

Figure 30. Deformation contours over the front shield of the modified FEM model at toroids inflation of 15 KPa

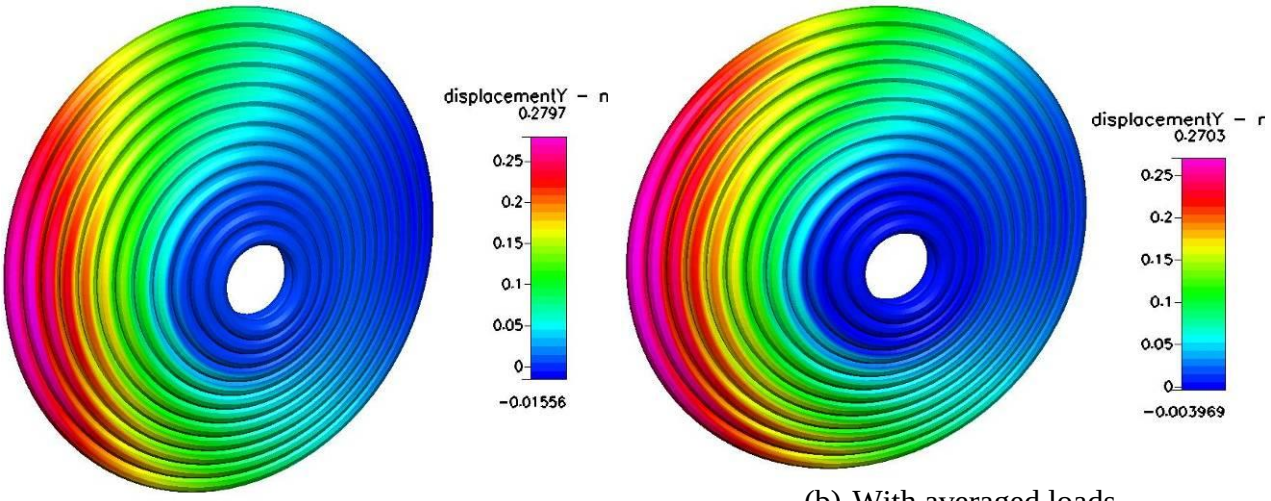

(a) With predicted CFD loads (b) With averaged loads

Figure 31. Deformation contours over the modified FEM model (removing the front gores skin) at toroids inflation of 15 KPa

The effect of toroids inflation pressure on the von Mises stresses for the cases of predicted CFD loads and CFD average loading are compared to the cases of constant loads of 5000 Pa in Figure 32. The cases simulated with the predicted CFD loading is obviously produced higher stresses since the highest stress is generally will be function of the high loads. The contours of von Mises stresses over the model in both cases are shown in Figure 33 for the case of toroids inflation pressure of 15 KPa. The maximum stress occurs in the middle of the windward side near the rigid front shield. The maximum stress on the model is mostly due to the aerodynamic loading. To emphasize this point, a series of FEM simulations were conducted to compute the model response under the effect of toroids internal pressure only, i.e. no CFD loading. The distribution

of von Mises stresses due to the internal pressure only is shown in Figure 34. As shown in the figure, the stresses due to toroids internal pressure only is one-order of magnitude less than the total stresses over the model due to the CFD loading and internal pressure. These test cases show that the effect of aerodynamic loading is higher than the effect of internal pressure.

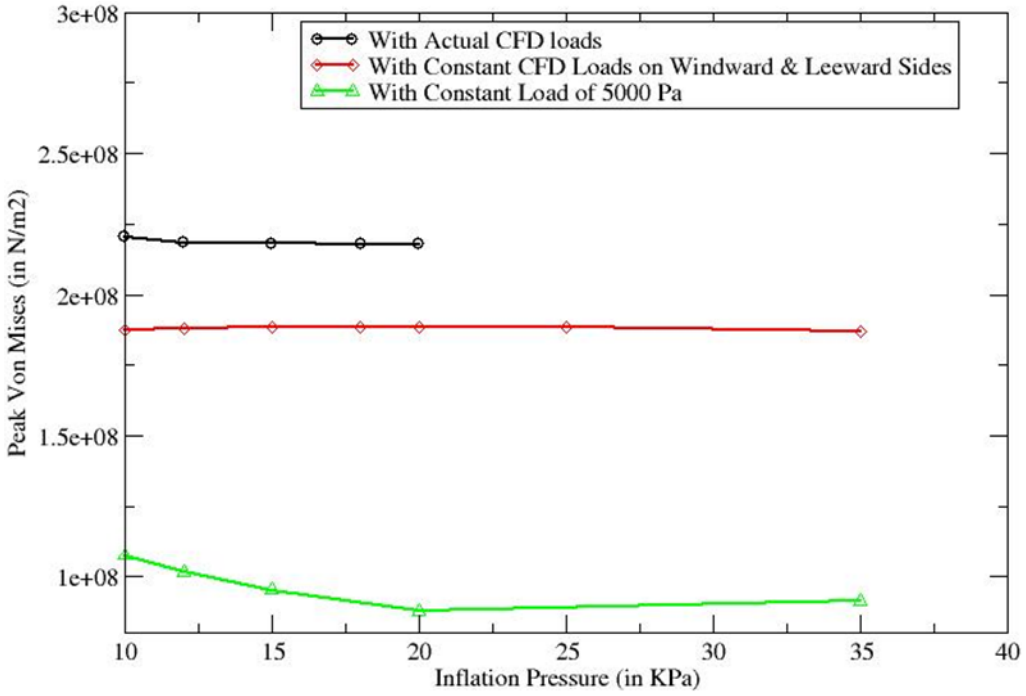

Figure 32. Effect of toroids inflation pressure on von Mises stresses

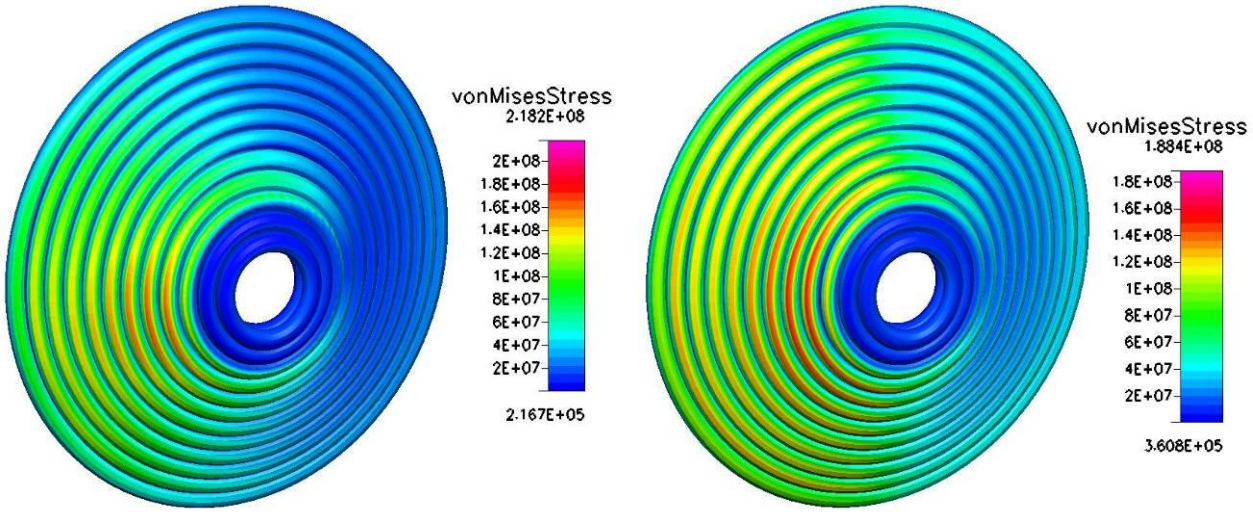

(a) With predicted CFD loads (b) With averaged loads

Figure 33. von Mises stresses over the modified FEM model at toroids inflation of 15 KPa

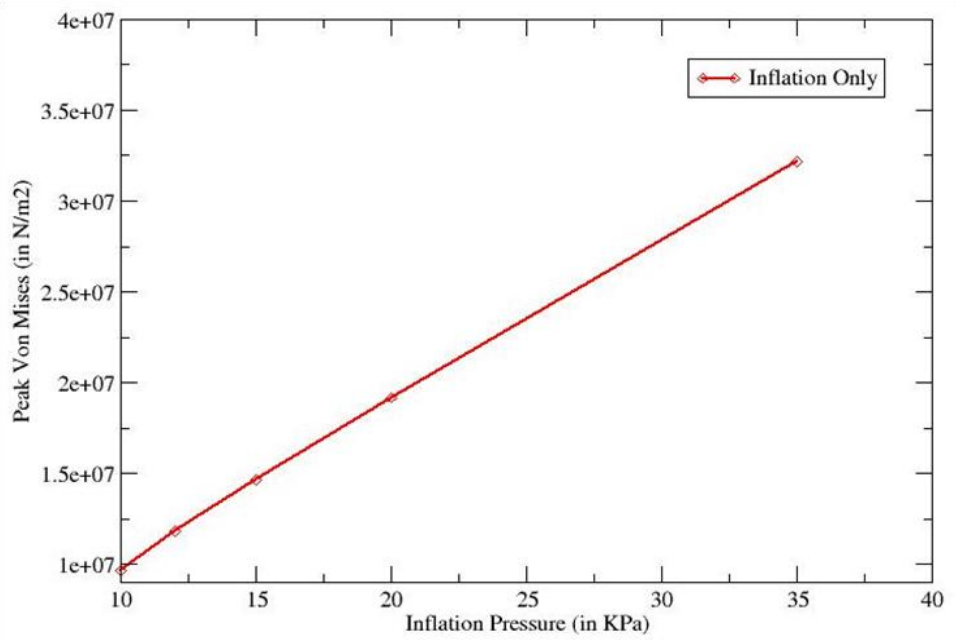

Figure 34. von Mises stress over the FEM model due to toroids internal pressure only.

4.3 Summary

A three-dimensional computational CFD model for the IAD model configuration was developed. A reacting thermally perfect CO2 model was used to simplify the Mars atmosphere. Steady state Euler simulation was conducted successfully at 30 degrees angle of attack, and the aerodynamic forces and moments were predicted. In addition, a computational structural nonlinear FEM model of the IAD model was developed using quad shell elements. A modified version of the FEM model was also developed that takes into consideration the axial straps of the toroids. Extensive FEM simulations were conducted with various internal pressures and using the CFD calculated loads and constant averaged loads.

5 AEROELASTIC AND DYNAMIC ANALYSIS OF THE DOUBLE STACK IAD CONFIGURATION

The models developed for the nominal double stack IAD configuration were used to conduct aero-structural and dynamic simulations at 30 degrees angle of attack and bank angle rate of 5 deg/sec^2. Simulations were carried out for up to 4 seconds. First, a dynamic moving body CFD simulation was conducted with an assumption that the entire IAD was rigid. This provides a set of baseline aerodynamic data to compare against. Then, several aero-structural simulations were conducted in this effort;

1. ***Dynamic fluid-structure interaction simulation with average constant CFD loading***. In this case, the average CFD loads on several patches of the model are applied to the FEM model and the structural responses are computed during the dynamic maneuver.
2. ***Dynamic fluid-structure interaction simulation with one-way coupling***. In this case, the CFD solves for the transient aerodynamic loads and transfer them to the FEM model every time step to solve for structural responses. The deflections are not fed back into the CFD model.
3. ***Dynamic fluid-structure interaction simulation with two-way coupling***. In this case, the CFD and FEM solvers are exchanging transient aerodynamic loads and aeroelastic deflections every time step.

The simulations for the three different coupling methods were executed over a cluster of computers of 20 CPU (5 nodes with 2 dual-core AMD Opteron 2218 processors each). The computational costs for conducting the simulations are shown in Table 6 (assuming no network interruptions). The computational cost is reported as time per single iteration of simulation. The time step for the simulations is 0.0001 s.

Table 5 Total clock time required for the three different methods of coupling on 20 CPUs

Method	Computation Time / Time Step
Averaged CFD Loading	22.68 seconds
One – Way FSI Coupling	68.04 seconds
Two-Way Coupling	75.60 seconds

5.1 Aerodynamic Forces for the Aeroelastic Dynamic Maneuver

As mentioned before, three aeroelastic dynamic simulations were conducted using average constant CFD loads, one-way FSI coupling, and two-way FSI coupling. All simulations assumed flexible structural model with banking maneuver of 5 deg/sec^2. All simulations were started from an undeformed initial state. Figure 35 shows the simulation time period for all the conducted aeroelastic dynamic simulations. The aeroelastic dynamic simulation with average constant CFD loading was conducted for about 4 seconds of simulation. The one-way coupling simulation case we conducted for about 3.2 seconds of simulation. The two-way coupling simulation case we conducted for about 2.1 seconds of simulation.

The histories of the aerodynamic forces and moments during the aeroelastic dynamic simulation are shown in Figure 36 - Figure 40. The results of the two-way coupling are compared to the aerodynamic coefficients of aerodynamic simulation with rigid-body motion for comparison. The histories of the lift and drag coefficients during the aeroelastic dynamic simulation are shown in Figure 36 and Figure 37, respectively. The history of the side force coefficient is shown in Figure 38. The figure shows that the aerodynamic loads coefficients fluctuates around mean values that are very close to the values of the aerodynamic forces for rigid body motion. The mean value of the drag coefficients is almost flat similar to the rigid body motion simulation. The histories of the moment coefficients during the aeroelastic dynamic simulation are shown in Figure 39 and Figure 40, respectively. The aerodynamic moment values are also very close to the values of rigid-body motion and have the same trend.

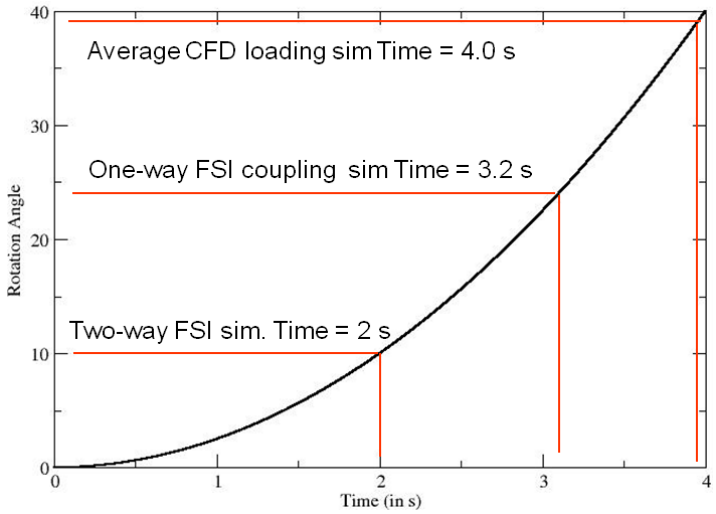

Figure 35. Bank maneuver simulation period for all considered aeroelastic simulations

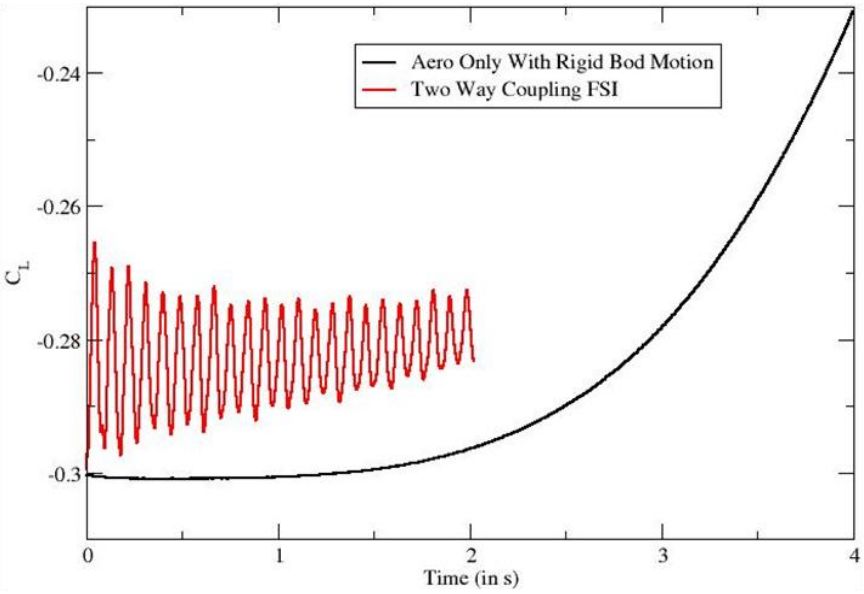

Figure 36. History of coefficient of lift during the aeroelastic dynamic simulation

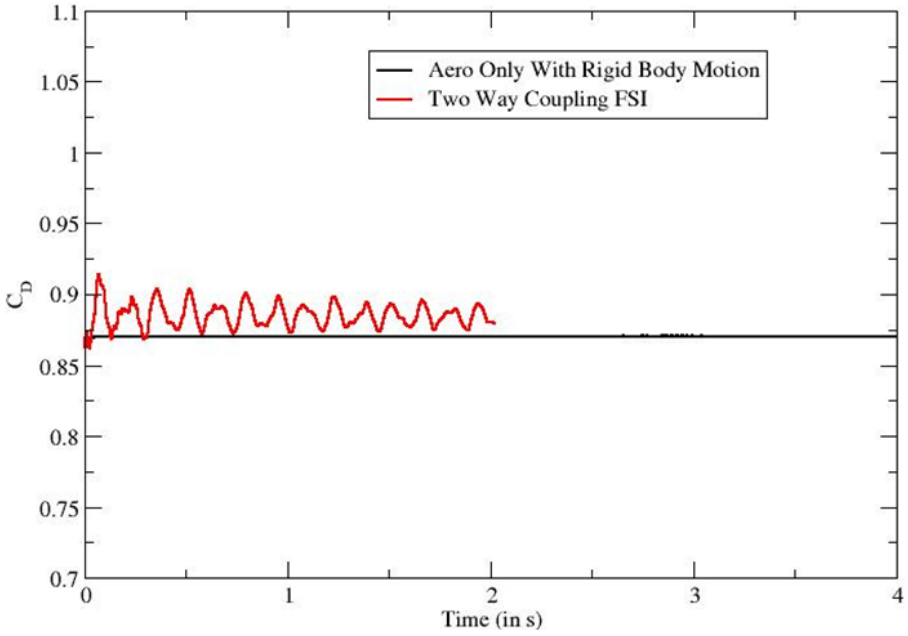

Figure 37. History of coefficient of drag during the aeroelastic dynamic simulation

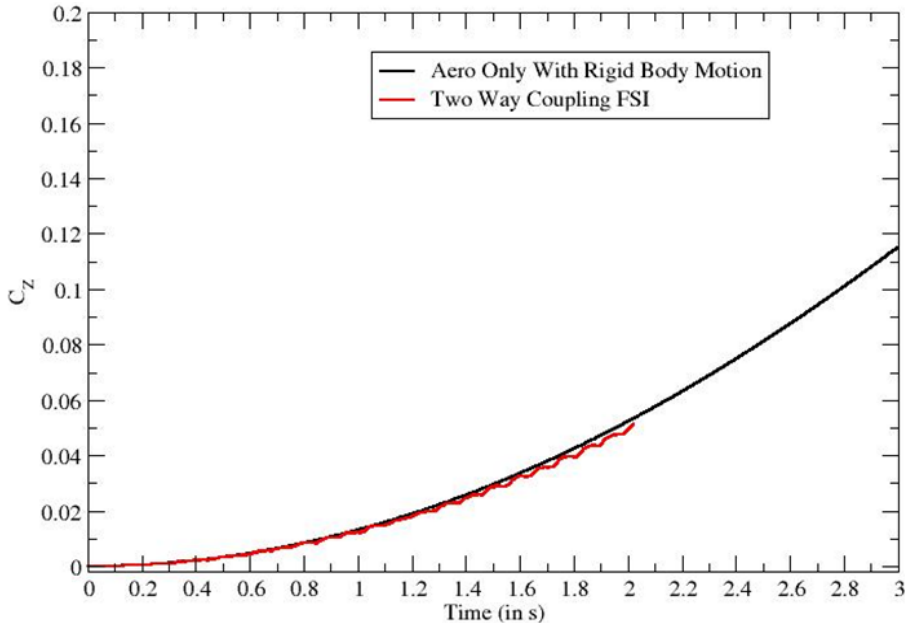

Figure 38. History of coefficient of side force during the aeroelastic dynamic simulation

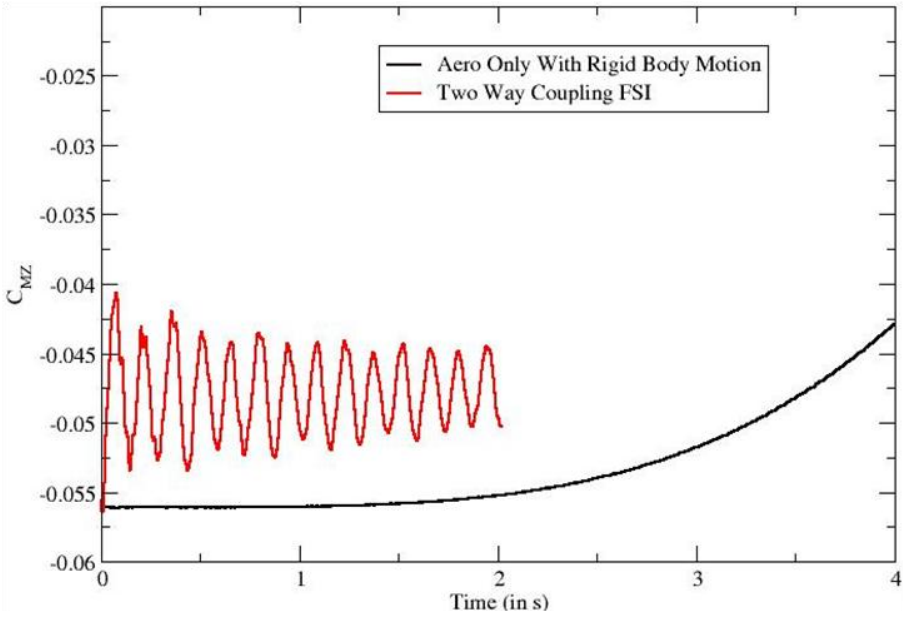

Figure 39. History of banking moment coefficient during the aeroelastic dynamic simulation

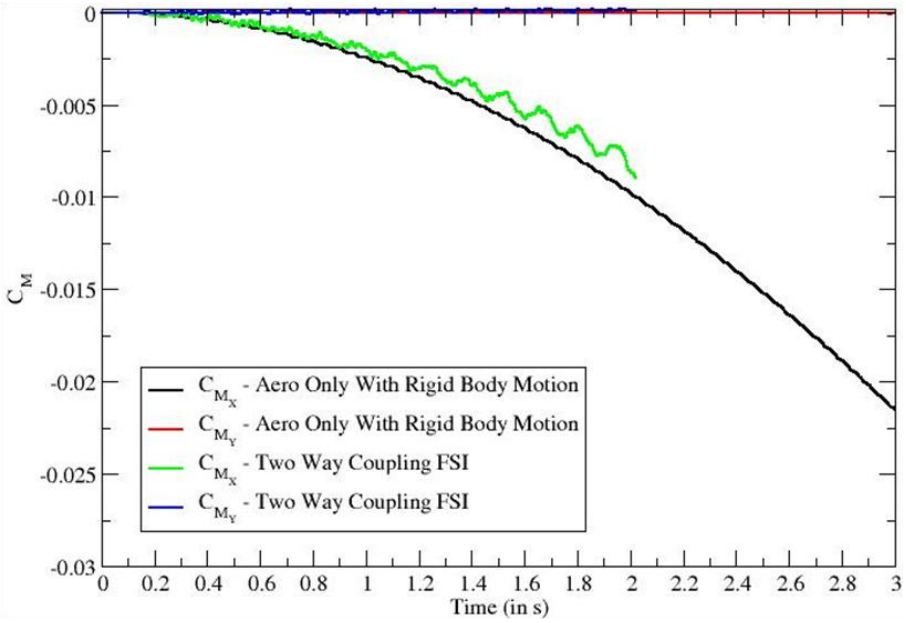

Figure 40. History of side moment coefficients during the aeroelastic dynamic simulation

5.2 Aeroelastic Structural Deformations

At first, the structural deformations for the case of average constant loading on the model are presented. The structural deformations are monitored at three points as shown in Figure 41; one

on the outer edge of the model, the second on the mid surface, and the third on the inner side of the model.

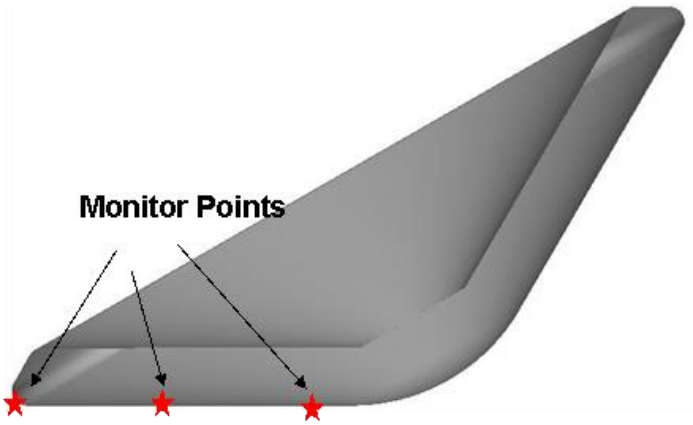

Figure 41. Monitor Point Locations on the Model

Comparison of the main component of structural deformation (y-component) for the three conducted simulations is shown in Figure 42. The contribution of the rigid body motion in this figure is zero as indicated previously. The figure shows that the model is fluctuating around a fairly constant mean. This mean value is very close to the steady state deformation value computed in Task 1. The results of the three simulations are comparable to each other. The mean value of aeroelastic deformation of the two-way coupling is slightly higher than the other two simulations and also shows damping over several cycles.

Figure 43 and Figure 44 show comparisons of the x- and z- components of structural deformations for the three conducted simulations. The components due to rigid-body motion are also shown in the figures for comparison. The figures show that the aeroelastic deformations for the conducted simulations are comparable to each other and that they are very close to the rigid-body motion case. The two-way coupling case shows faster damping of the x-component of deformation. No significant change is shown in the z-component of structural deformation between all the considered simulations. The contribution of the aeroelastic deformation only for the z-component for the two-way coupling simulation is shown in Figure 45.

The previous simulations were conducted using the original thickness of the gores (skin) which is about 26.5 mil. However, the actual model contains 18 radial straps of 12 mm thickness and modulus of elasticity of 14 GPa. The structural model considered in this study do not model the radial straps. If the effect of straps were taken into consideration, the thickness of the gores may have to be increased to about 200 mil. The structural deformations for the skin thickness of 26.5 mil are shown in Figure 46. The structural deformations for the skin thickness of 200 mil are shown in Figure 47. Since the model is exhibiting banking maneuver, the x- and z-components of deflections contain both the aeroelastic deformations and the rigid body motion contribution. The y-component of deflection contains only the aeroelastic deformation since the model is not moving in this direction. The figures show that both cases are stable and as obvious the 200 mil thickness case produced less aeroelastic deflections than the 26.5 mil thickness case. The effect of different model thickness will be discussed in more details in the next chapter.

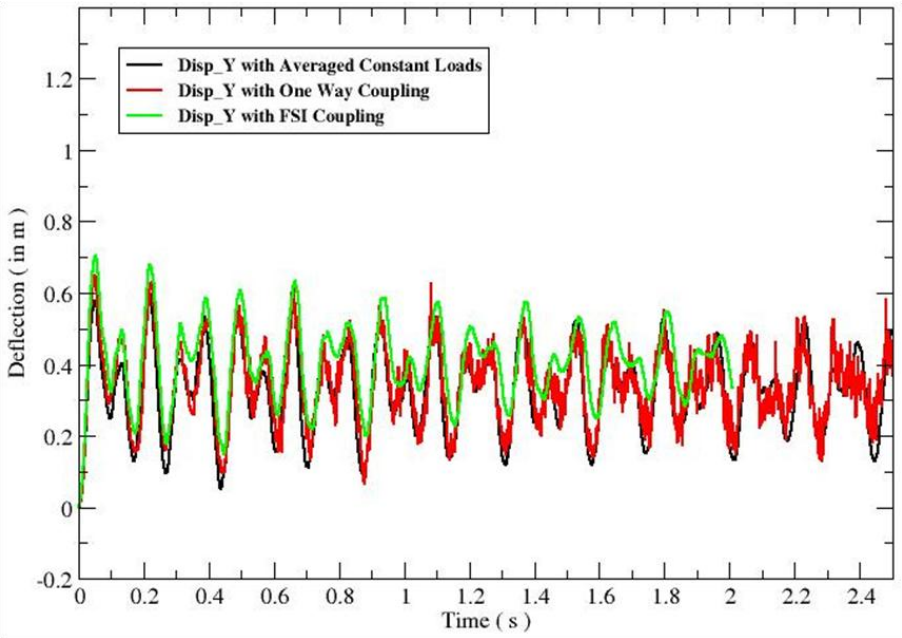

Figure 42. Comparison of y-component of structural deformation for the conducted simulations

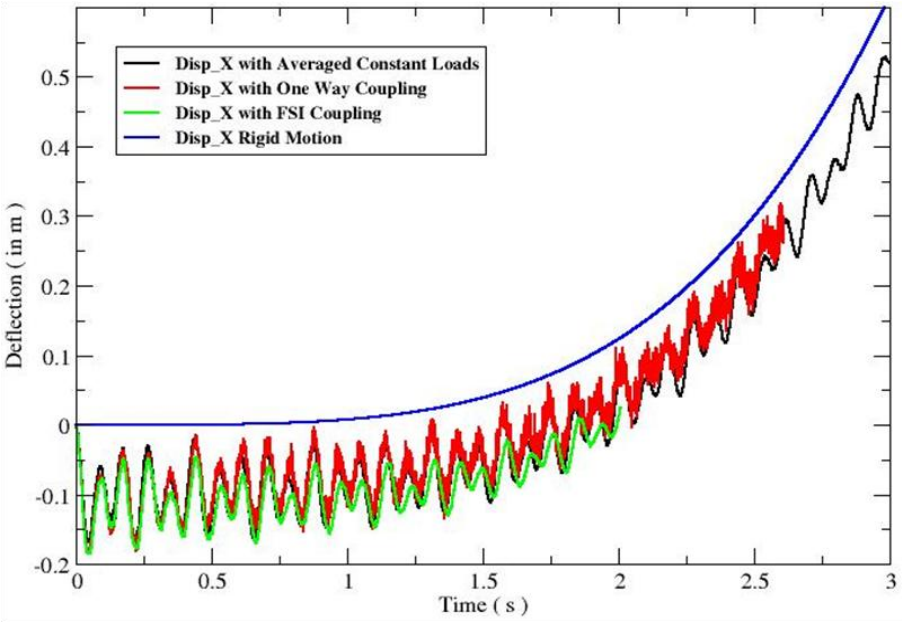

Figure 43. Comparison of x-component of structural deformation for the conducted simulations

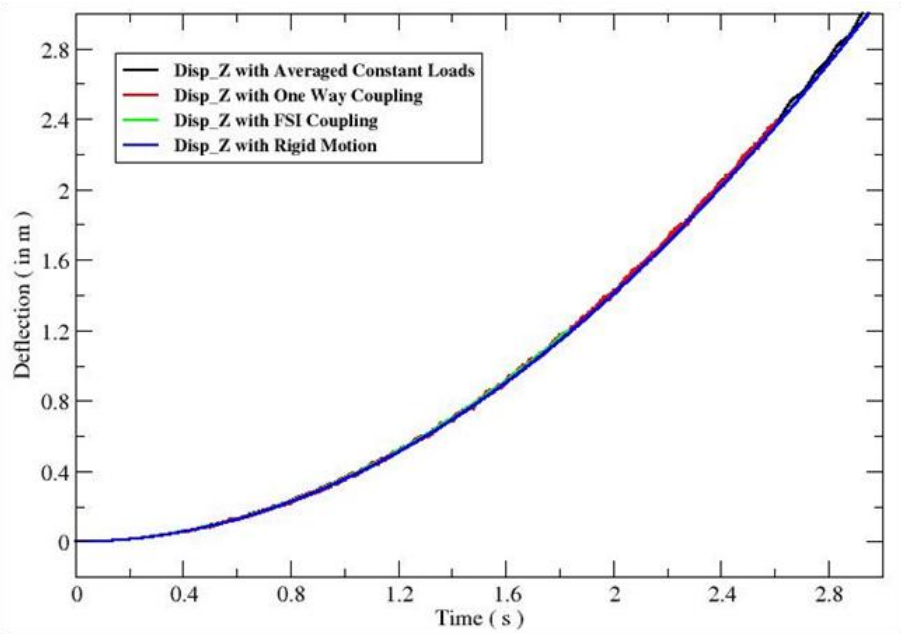

Figure 44. Comparison of z-component of structural deformation for the conducted simulations

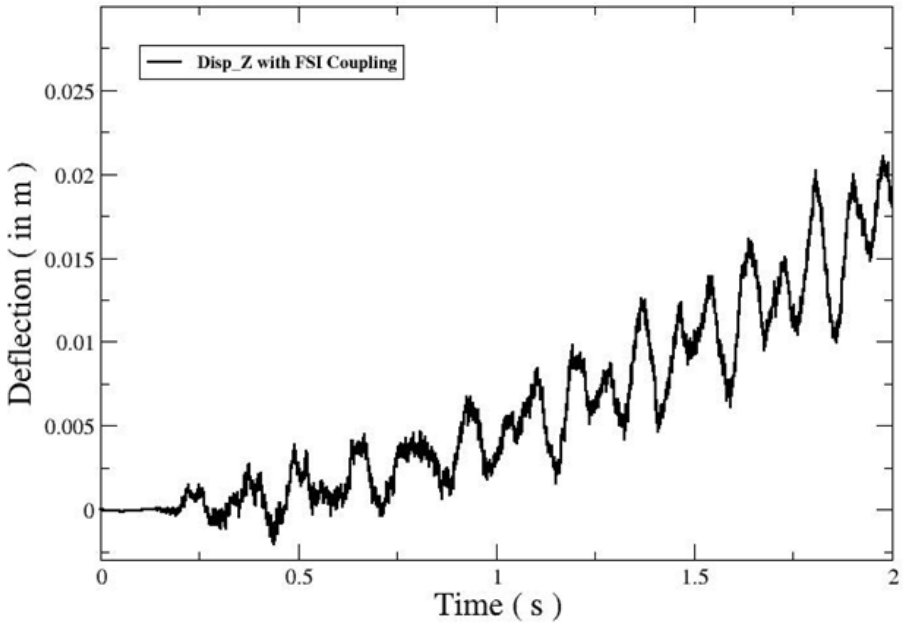

Figure 45. Contribution of aeroelastic deformation only for the two-way coupling simulation.

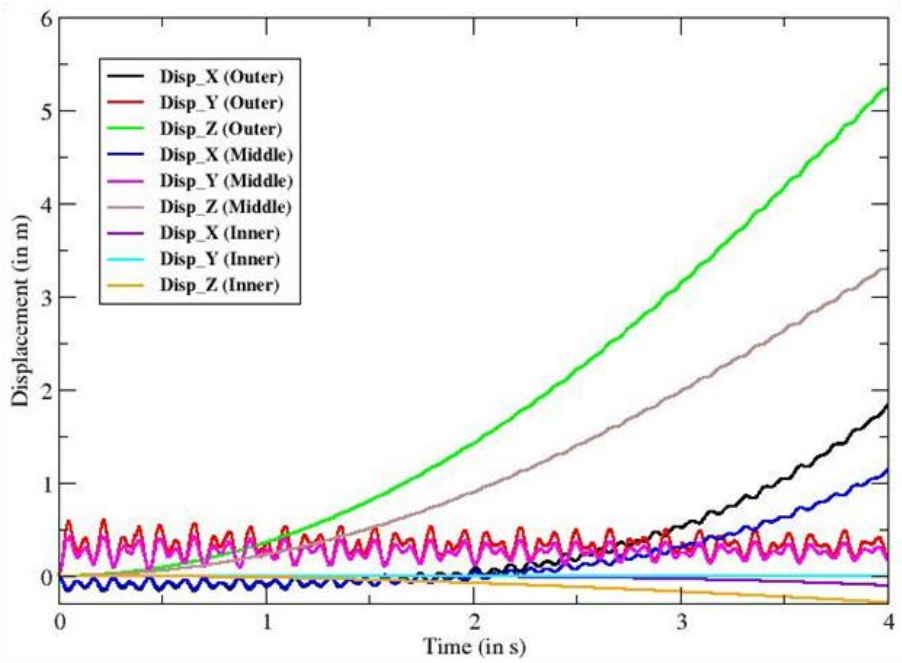

Figure 46. Structural deformation of the average constant CFD loading simulation at skin thickness of 26.5 mil.

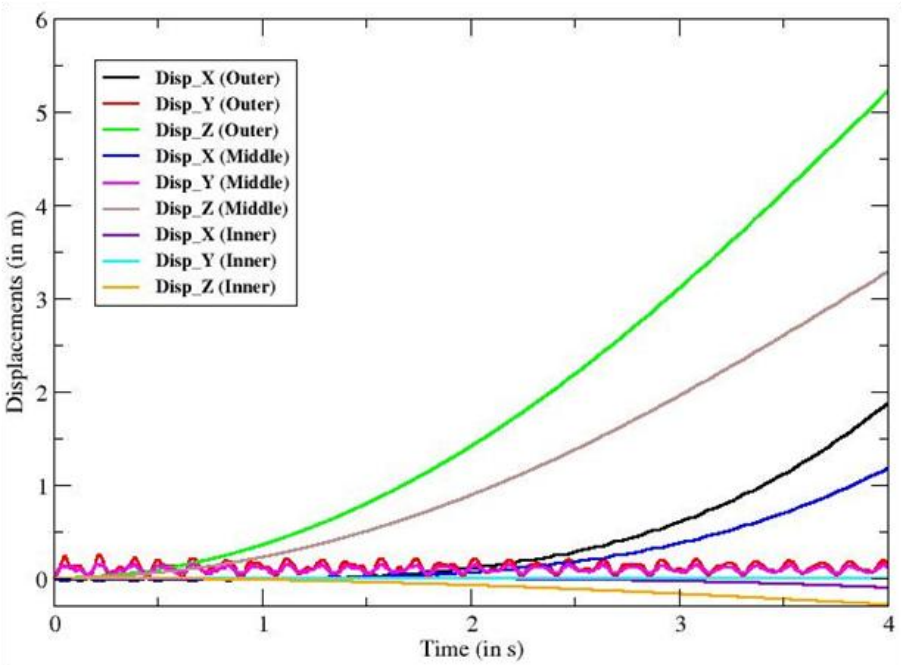

Figure 47. Structural deformation of the average constant CFD loading simulation at skin thickness of 200 mil.

5.3 Aeroelastic Structural Stresses

Snapshots of von Mises stresses on the front surface of the toroids (without skin) are shown in Figure 48. The figure shows that the von Mises stress is cyclic, similar to the structural deformations, and is fluctuating between a maximum value of 4.9 E+08 N/m^2 and a minimum value of 1.5 E+08 N/m^2. Since the yield stress of the Kevlar material is 35 GPa, the stress levels are way below the yield stress of the material. The peak stress levels occur at the windward side of the front surface of the toroids. Snapshots of von Mises stresses on the back surface of the toroids (without skin) are shown in Figure 49. Similar to the front surface, the stresses are also cyclic but they fluctuate around values less than those of the front surface. The peak stress levels occur around the inner circle of the surface, near the adapter location. Snapshots of von Mises stresses on the front surface of the skin are shown in Figure 50. The values of stresses on the skin are almost one-order of magnitude less than those values on the toroids. The von Mises stress on the skin is also cyclic, and is fluctuating between a maximum value of 1.4 E+08 N/m^2 and a minimum value of 5.4 E+07 N/m^2. The peak values of stresses occur around the inner circle of the model near the location of the adapter.

The variation of the peak value of the von Mises stress versus time over the model is shown in Figure 51. The peak values of stresses occur over the front surface of the toroids. The figure shows clearly the cyclic nature of the stress variation which is in similar trend to the structural deformation of the model.

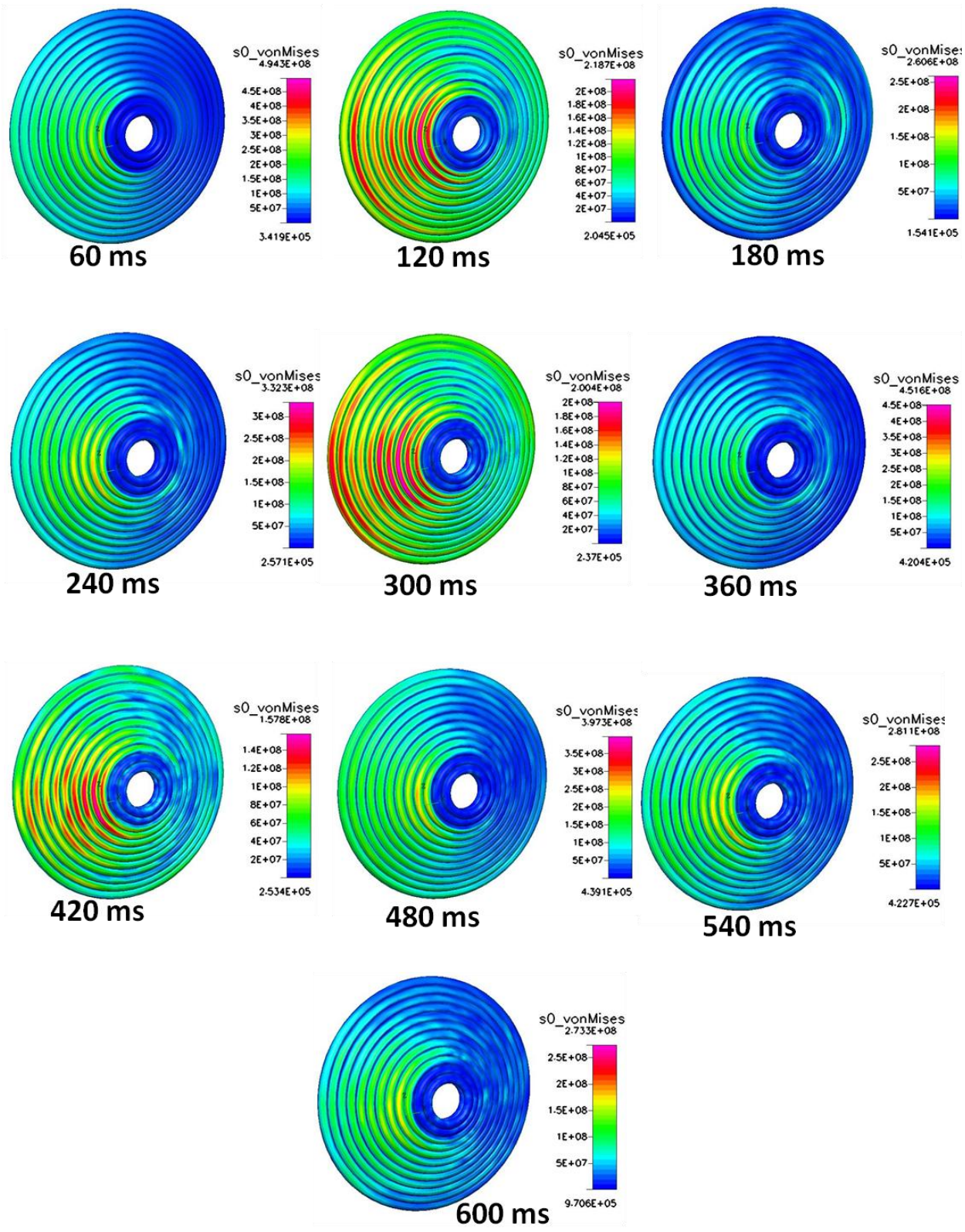

Figure 48. Snapshots of von Mises stresses on the front surface of the toroids

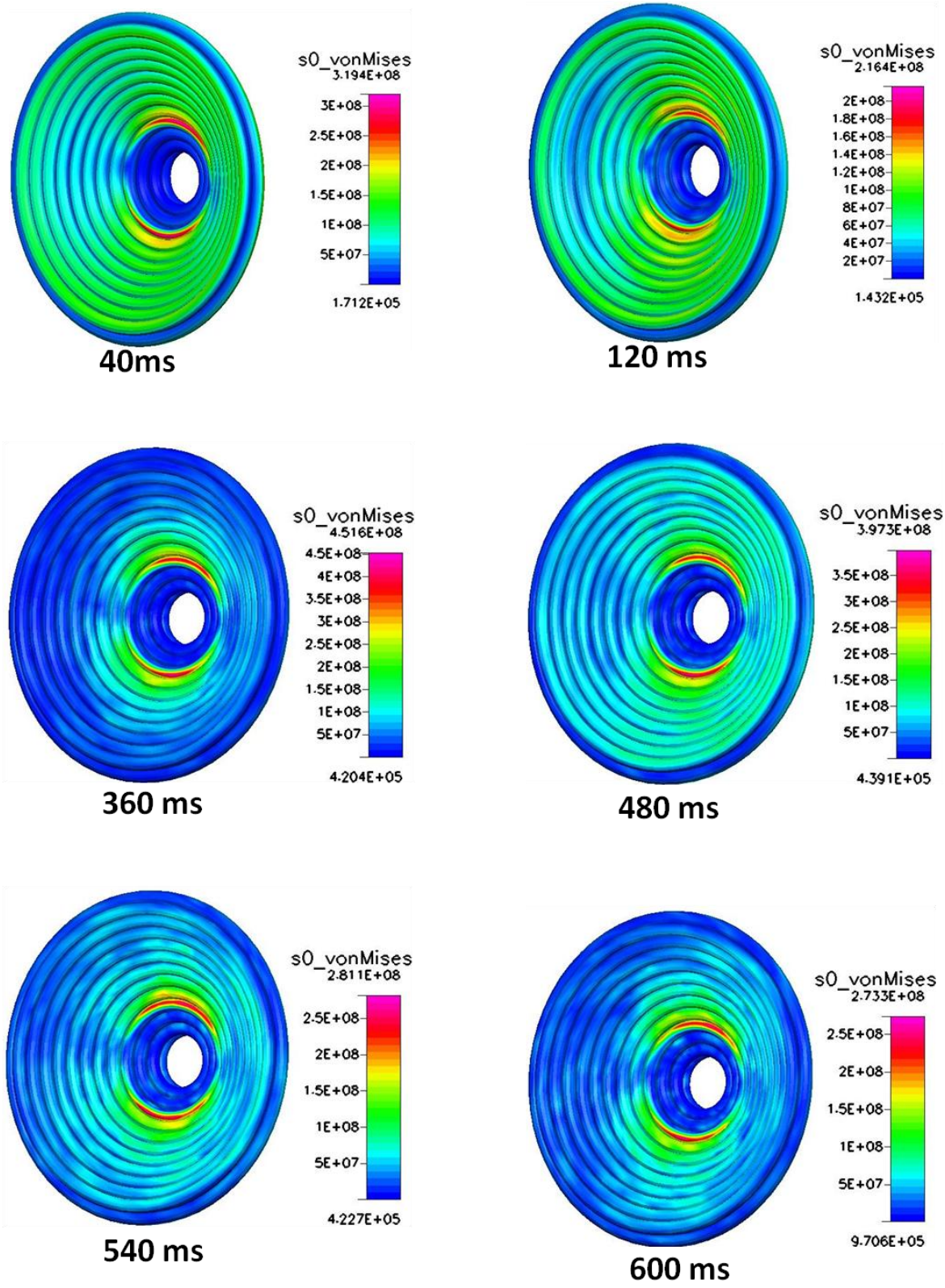

Figure 49. Snapshots of von Mises stresses on the back surface of the toroids

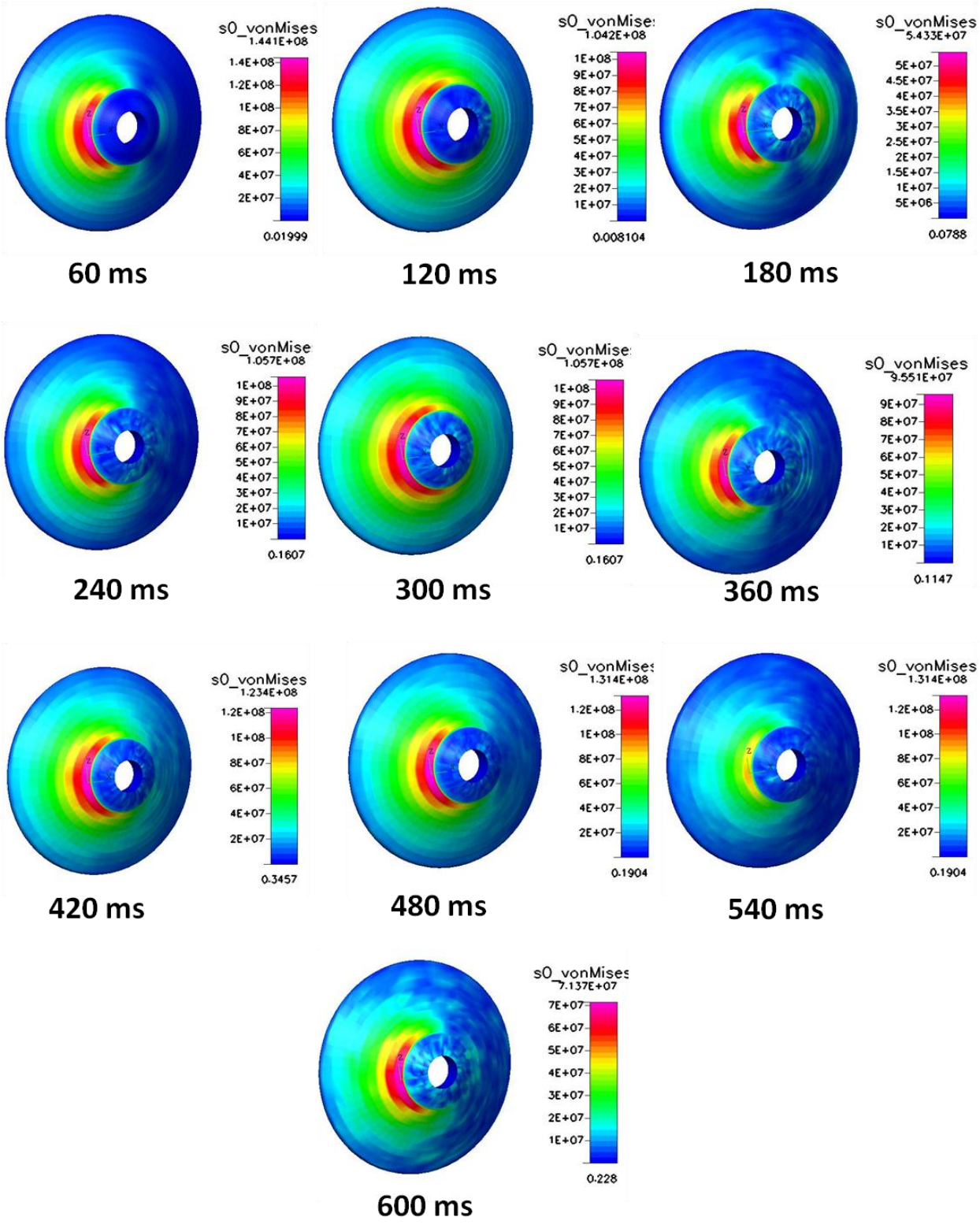

Figure 50. Snapshots of von Mises stresses on the front surface of the gores

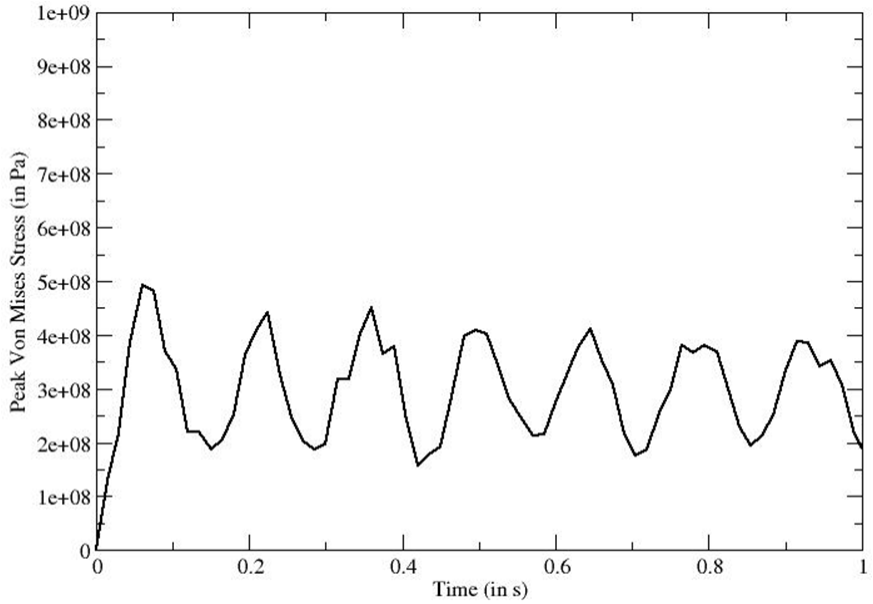

Figure 51. Variation of peak von Mises stress versus time

5.4 Summary

The aeroelastic responses of the model were computed for three simulations; using average constant CFD loading, using one-way FSI coupling from the fluid to the structure, and using two-way FSI coupling. The structural responses of the three simulations were comparable. The structural deformations and stresses were cyclic over the model and they fluctuates around an almost constant mean values. Although the von Mises stress levels on the gores and toroids were far less than the yield stress of the materials of the gores and toroids, it was seen that the peak tip deflections of the IAD were quite large (~0.7 m). We determined in consultation with the technical monitor that this was most likely the effect of ignoring the presence of the radial straps.

6 AEROELASTIC AND DYNAMICS ANALYSIS OF A MODIFIED DOUBLE STACK IAD CONFIGURATION INCLUDING RADIAL STRAPS

In the previous chapter, the tip deflections of the IAD were larger than expected. They were of the order of 0.6 to 0.7 m in the flow direction. This is most likely the effect of ignoring the presence of the radial straps. In this part of the study, the effect of modeling the radial straps is simulated. The effect of inflation pressure on the peak deflections is also simulated. Aero-structural and dynamic simulations of the IAD model at 30 degrees angle of attack and bank angle rate of 5 deg/sec^2 were conducted. Simulations were carried out for up to 4 seconds. An effort was also made to speed up the computation by coarsening the CFD grid. The following aero-structural simulations were conducted in this effort:

1. ***Effect of toroid inflation pressure on the dynamic response of the using average constant CFD loading***. In this case, the average CFD loads on several patches of the model are applied to the FEM model and the structural responses are computed during the dynamic maneuver for various toroid internal pressures.
2. ***Effect of coarsening the CFD grid***. In this case, the two-way coupled FSI case from task was re-run with a coarser CFD grid. The solutions of the fine and coarse grid were then compared.
3. ***Effect of radial straps***. In this case, the effect of radial straps was accounted for, both by a) increasing the thickness of the cover (skin) and b) by increasing thickness and its material properties.

6.1 Effect of Toroids Inflation Pressure on IAD Dynamics

In order to attempt to reduce the deflection, the effect of the increase in the toroids inflation pressure on the IAD dynamic was simulated. The inflation pressure of the toroids was increased by 50% and 100% from the baseline 15 KPa, to 22.5 KPa and 30 KPa respectively. All simulations were started from an undeformed initial state. The aeroelastic dynamic simulation with average constant CFD loading was conducted for about 4 seconds of simulation.

The plot of displacement in the y-direction (direction of flow) at the outer edge of the IAD for the three inflation pressures applied is shown in Figure 52. The displacement in x-direction is shown in Figure 53. Since the model is performing a banking maneuver, the x-component of deflection contains both the aeroelastic deformations and the rigid body motion contribution. The y-component of deflection contains only the aeroelastic deformation since the model is not moving in this direction. The contribution of the aeroelastic deformation only for the x-component is shown in Figure 54.

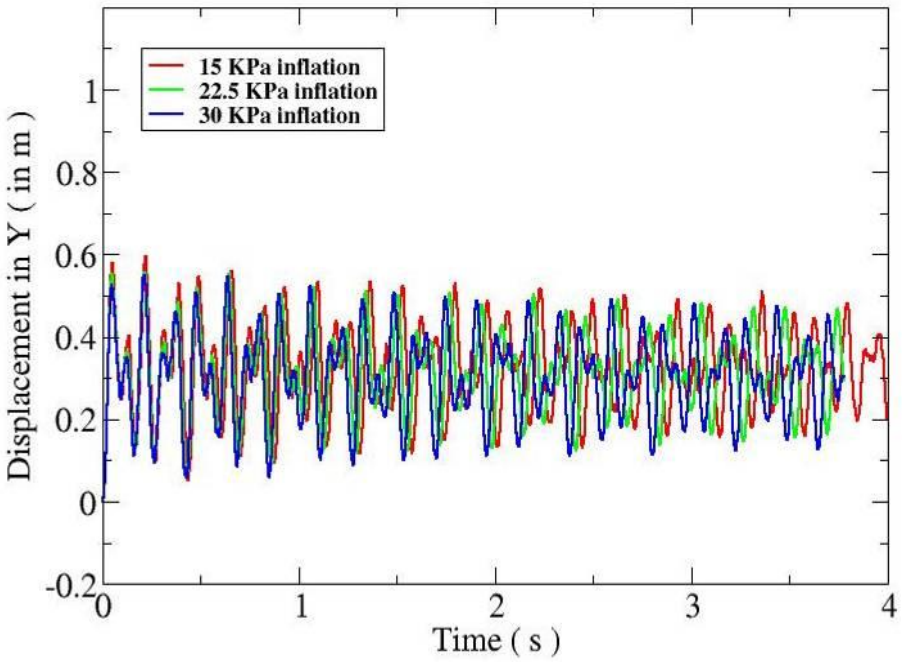

Figure 52 Comparison of y-component of structural deformation for various inflation pressures.

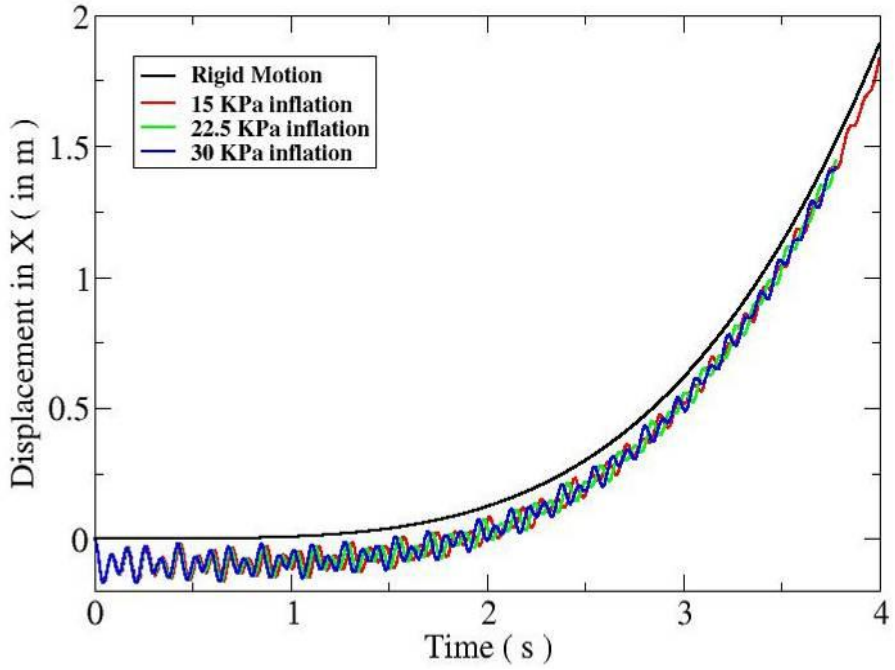

Figure 53 Comparison of x-component of structural deformation for various inflation pressures.

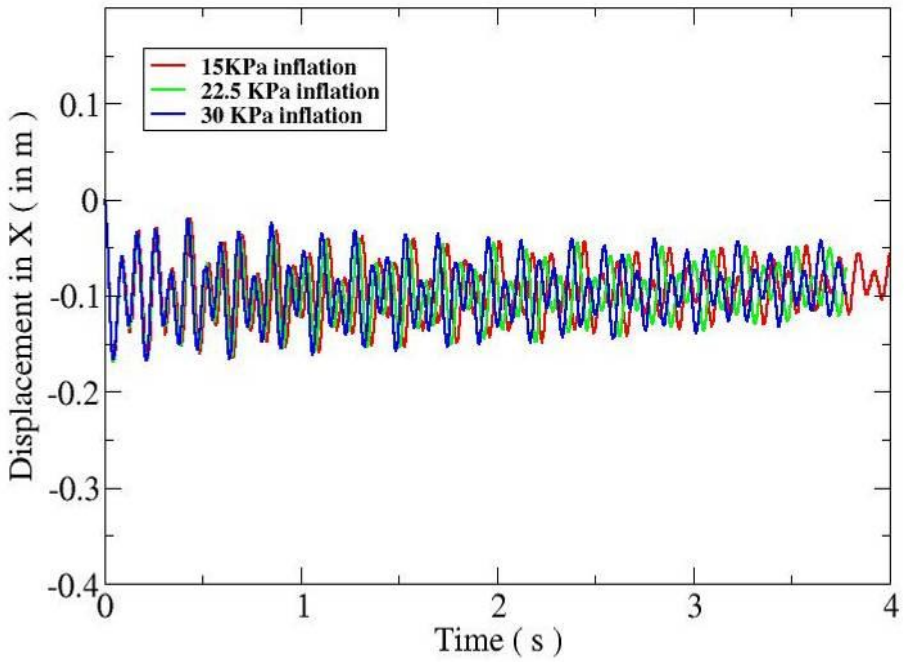

Figure 54 Comparison of aeroelastic component of structural deformation in the x-direction for various inflation pressures.

The results show that the overall deformation of the model is reduced by about 4 to 7 % in response to increase in inflation pressure of 50 to 100%. This is keeping in line with the results obtained in task 1 for steady state deformation response to increase in pressure.

6.2 Effect of Coarse Grid on the Solution

In task 2, it was seen that the CFD solution with a grid of 2.4 million cells was very stable and robust, even during large structural deflections. However, the aeroelastic analysis with a fine CFD grid required about 4 weeks, on a cluster of 20 CPUs (5 nodes with 2 dual-core AMD Opteron 2218 processors each), assuming no network interruptions, to complete 4 seconds of simulations. Therefore, to speed up the solution, the CFD grid was reduced from 2.4 M to 1.6 M, primarily in the circumferential direction. The CSD grid was kept the same as before. Then, the two-way coupled FSI simulation from task 2 was rerun using the new grid to see the effect of the coarse grid on solution quality.

6.2.1 Effect of Grid Coarsening on Aerodynamic Forces and Moments

The histories of the aerodynamic forces and moments during the aeroelastic dynamic simulation are shown in Figure 55 - Figure 60. The results of the two-way coupling methods using the fine and coarse CFD grids are compared with each other along with the aerodynamic coefficients of aerodynamic simulation with rigid-body motion for reference. The histories of the lift and drag coefficients during the aeroelastic dynamic simulation are shown in Figure 55 and Figure 56, respectively. The history of the side force coefficient is shown in Figure 57. The histories of the

side moment coefficients and banking moment coefficients are shown in Figure 58, Figure 59 and Figure 60. All results indicate very close agreement between the fine and coarse grid solutions. The coefficient of drag, which is the primary aerodynamic coefficient of interest, is unaffected by the reduction in grid. The effect on the magnitude, phase or frequency of the oscillations of all the aerodynamic coefficients was minimal.

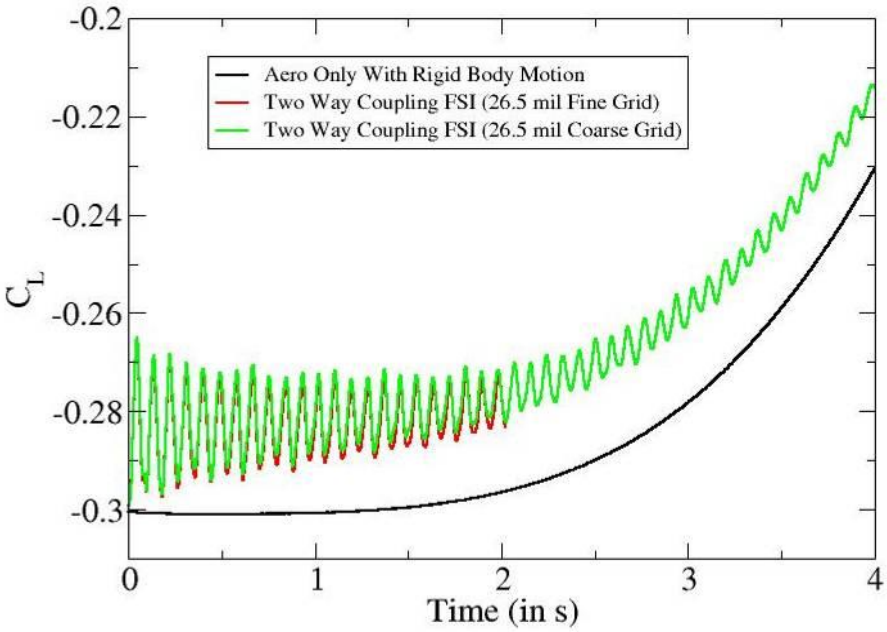

Figure 55. History of coefficient of lift during the aeroelastic dynamic simulation for coarse and fine grids

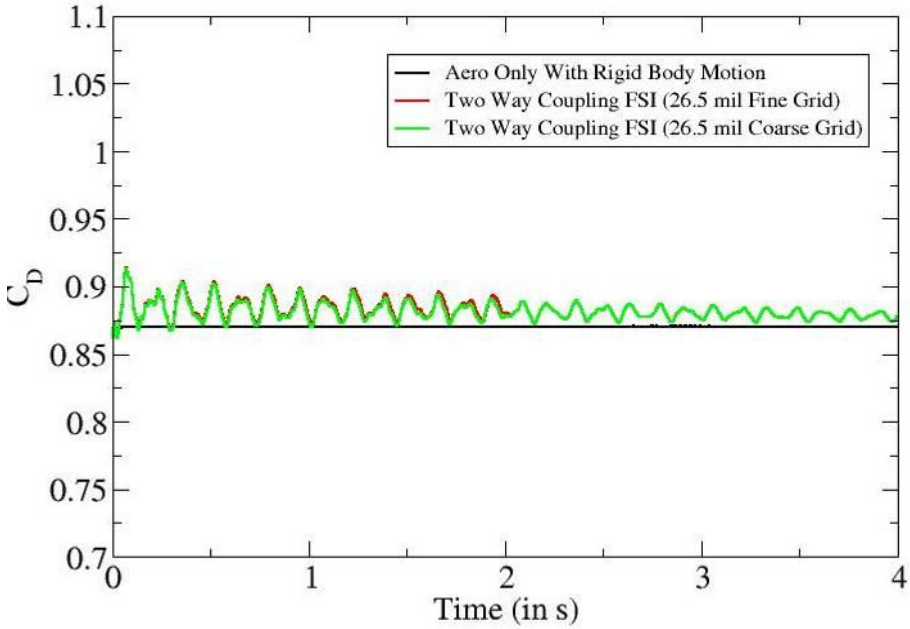

Figure 56. History of coefficient of drag during the aeroelastic dynamic simulation for coarse and fine grids

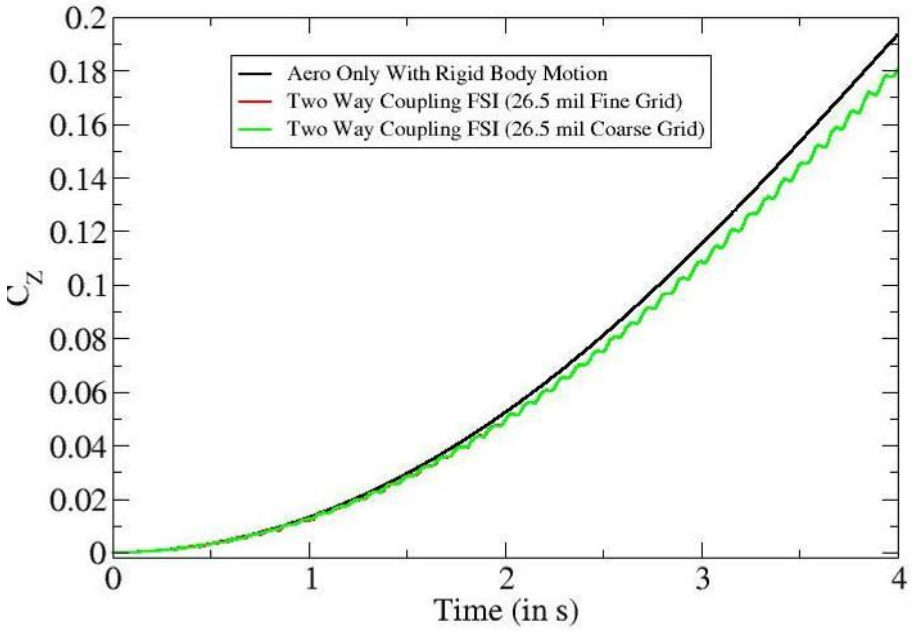

Figure 57. History of coefficient of side force coefficient during the aeroelastic dynamic simulation for coarse and fine grids

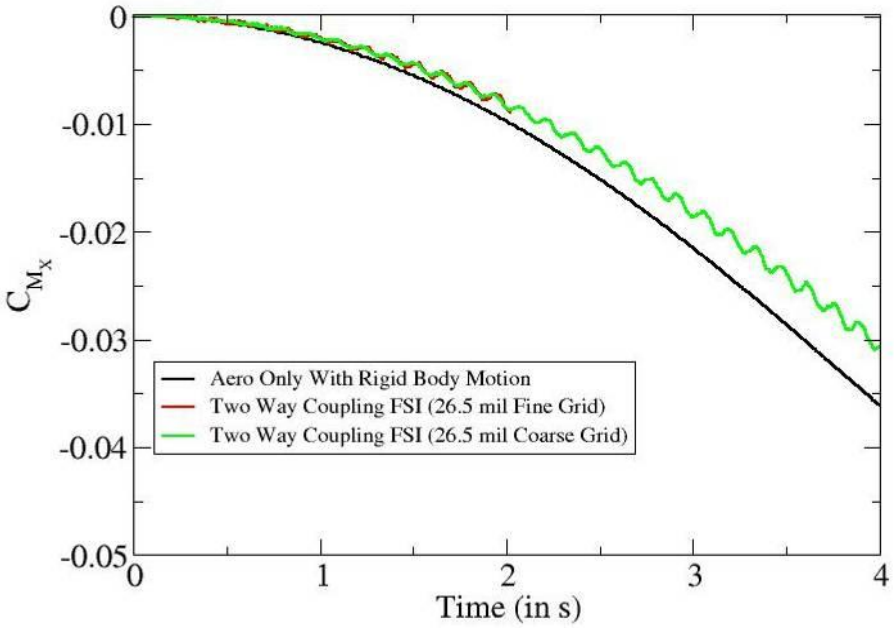

Figure 58. History of side moment coefficient in the x-direction during the aeroelastic dynamic simulation for coarse and fine grids

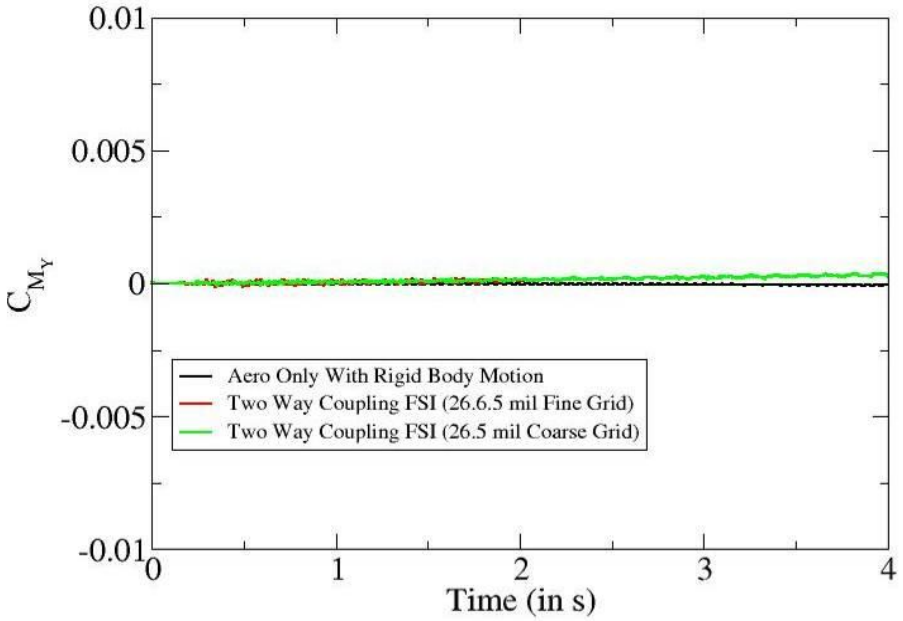

Figure 59. History of side moment coefficient in the y-direction during the aeroelastic dynamic simulation for coarse and fine grids

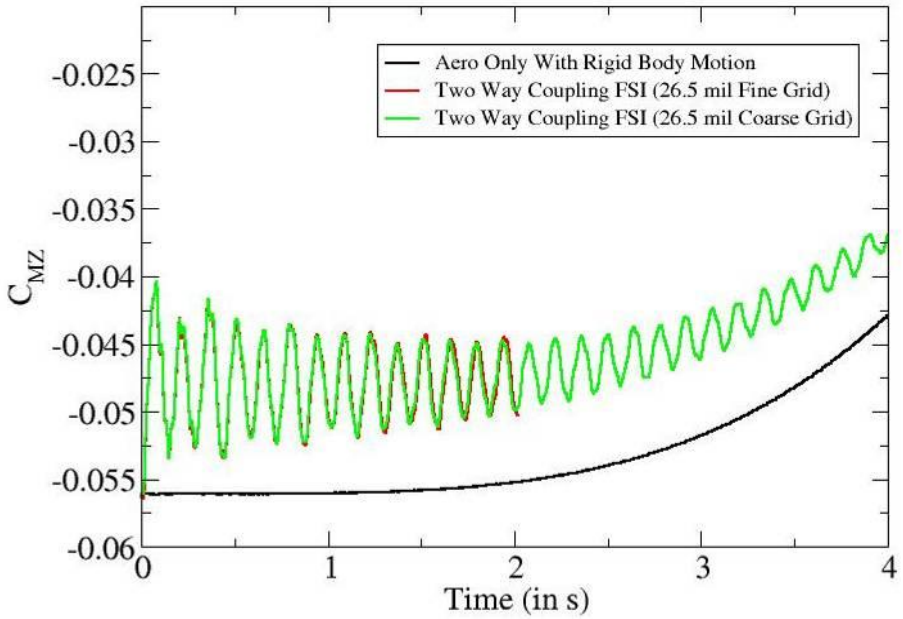

Figure 60. History of banking moment coefficient during the aeroelastic dynamic simulation for coarse and fine grids

6.2.2 Effect of Grid Coarsening on Structural Deformations

The plot of displacement in the y-direction (direction of flow) for the three inflation pressures applied is shown in Figure 61. The displacement in x-direction is shown in Figure 62. The results

show that the displacements using the coarse and fine grid results are nearly the same. The displacement in the y-direction, which is the direction of flow, is unaffected by the coarse grid.

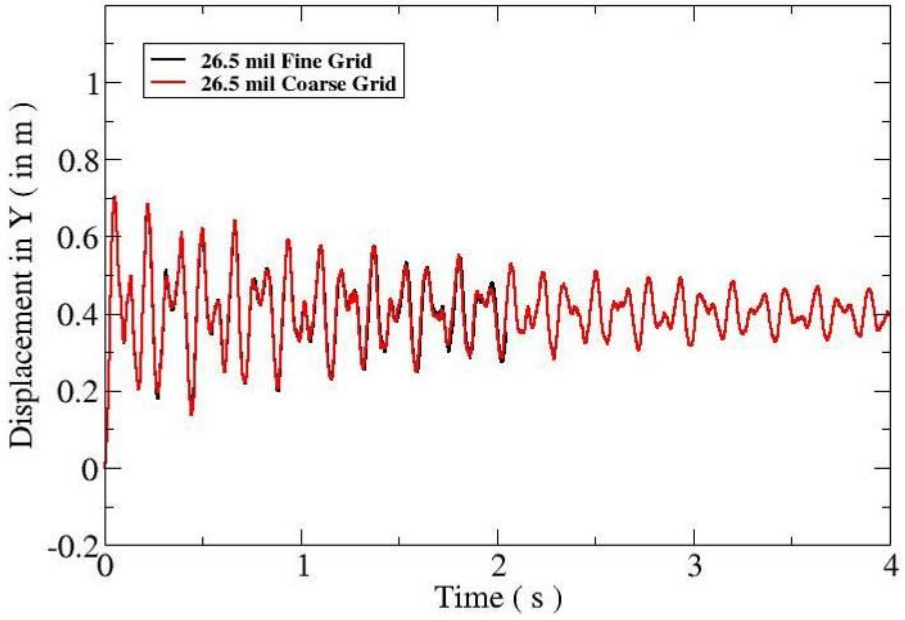

Figure 61 Comparison of y-component of structural deformation for various inflation pressures.

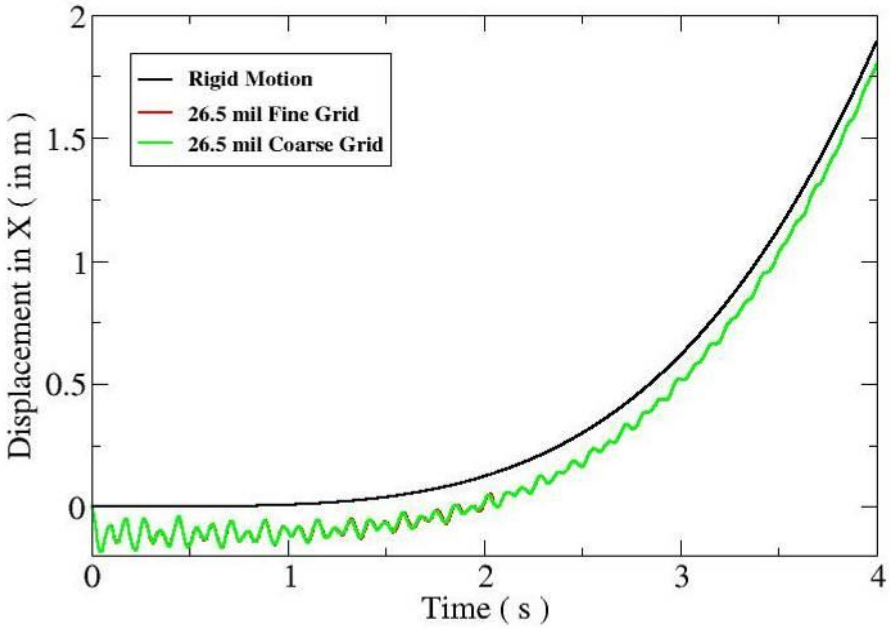

Figure 62 Comparison of x-component of structural deformation for various inflation pressures.

The coarse grid show very good agreement with the fine grid results. The coarse grid allows us to run the full 4 seconds of simulation in about 2 weeks on a cluster of 16 CPUs (4 nodes with 2 dual-core AMD Opteron 2218 processors each), assuming no network interruptions. This is

nearly a 100% speed up improvement in the FSI simulations compared to the fine grid. The coarse grid is used for simulations from this point onwards.

6.3 Effect of Modeling Radial Straps

As mentioned before, it was seen in the previous chapter that the tip deflections of the IAD were larger than expected. It is strongly believed that the large deflections were due to ignoring the effect of radial straps. The radial straps are made of the more rigid Kevlar material and they have substantial mass and thickness. Therefore, an attempt was made to present a more consistent model with the actual design by developing an equivalent mechanical model to the radial straps.

Instead of modeling the radial straps by adding the strap geometry to the existing structural model, after consultation with the program technical monitor, the effect of the radial straps was simulated using two methods;

a) Developing an equivalent mechanical model by increasing the thickness of the gores to account for both the area of the straps and higher modulus of elasticity of the straps Upilex material. In the model, the equivalent thickness of the gores was about 200 mil with Upilex E of 3.7E+9 Pa.

b) Developing an equivalent mechanical model by increasing the thickness of the gores to account for the area of the straps, and computing an equivalent modulus of elasticity (E) to account for the different E between the Upilex of the gores and Kevlar of the straps. In this model, the equivalent thickness of the gores was about 54 mil, and the equivalent modulus of elasticity was about 19.6E+9 Pa.

The dynamic FSI simulations conducted in this section were performed with an inflation pressure of 15 KPa. All simulations were started from an undeformed initial state. The aeroelastic dynamic simulations with constant averaged CFD loads and with two-way FSI coupling were conducted for about 4 seconds of simulation. The results were compared to the model without radial straps (26.5 mil) and also with the rigid body motion.

6.3.1 Aerodynamic Forces and Moments

The histories of the aerodynamic forces and moments during the aeroelastic dynamic simulation are shown in Figure 63 - Figure 68. The results of the two-way coupling methods using the two radial strap models are compared with the case without radial straps and with the aerodynamic coefficients of aerodynamic simulation with rigid-body motion for reference. The histories of the lift and drag coefficients during the aeroelastic dynamic simulation are shown in Figure 63 and Figure 64, respectively. The history of the side force coefficient is shown in Figure 65. The histories of the side moment coefficients and banking moment coefficients are shown in Figure 66, Figure 67, and Figure 68.

The results show that there is a significant reduction in oscillation of the aerodynamic coefficients about their mean when the radial straps are taken into consideration. All the results

show damping of the oscillations as the simulation progresses, which may indicate that the structure model is aeroelastically stable. It is believed that the oscillations damping is because of aerodynamic damping as well as the dynamic motion of the model. The results also indicate that the radial strap model with the 54 mil thickness and high E is more rigid than the others and is consequently the closest to the reference rigid body motion solution.

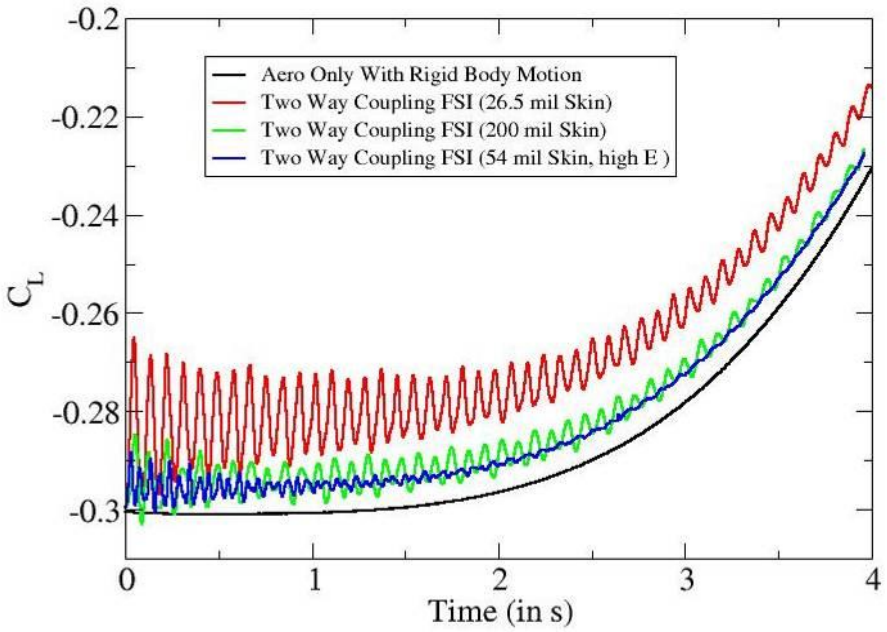

Figure 63. History of coefficient of lift during the aeroelastic dynamic simulation for various radial strap models

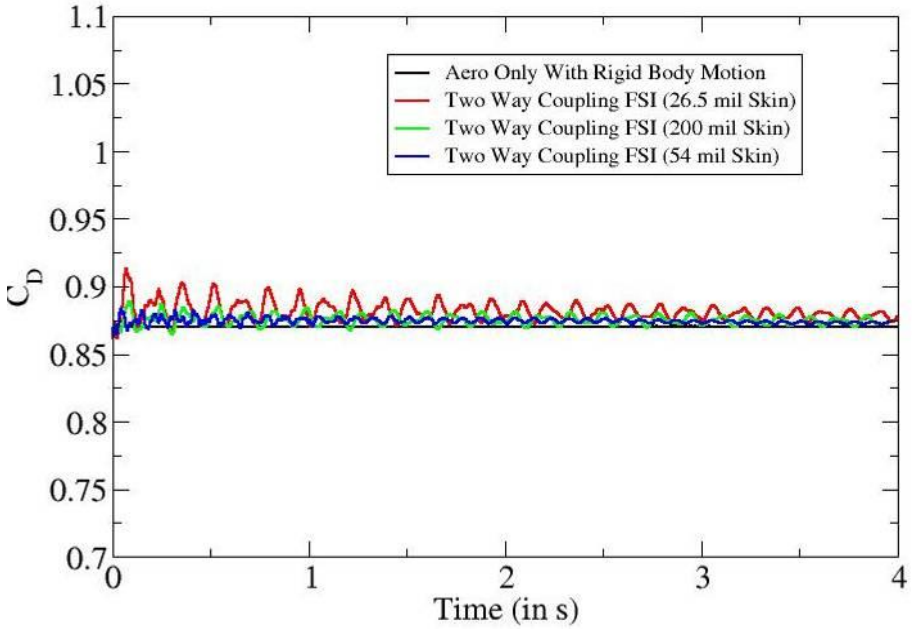

Figure 64. History of coefficient of drag during the aeroelastic dynamic simulation for various radial strap models

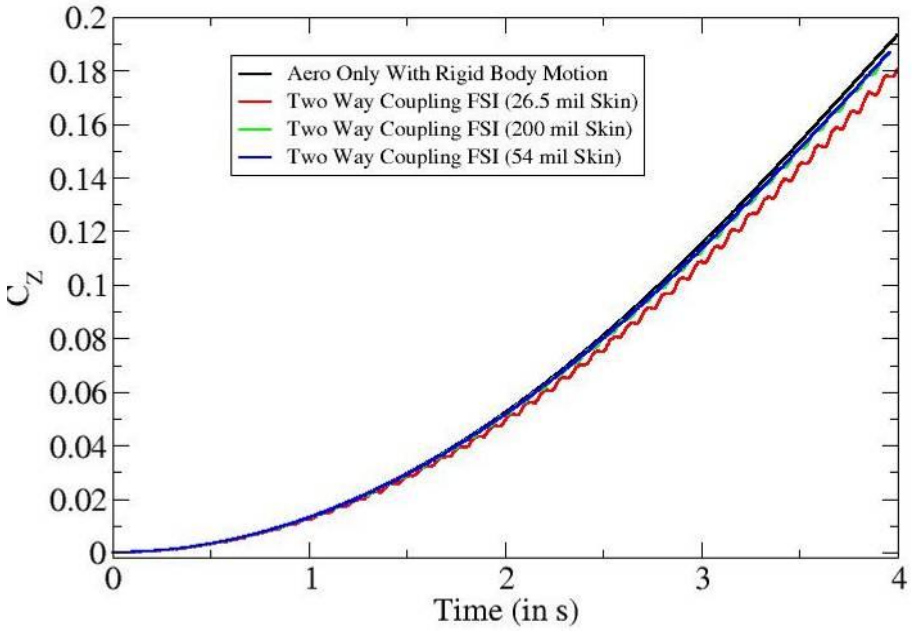

Figure 65. History of side force coefficient during the aeroelastic dynamic simulation for various radial strap models

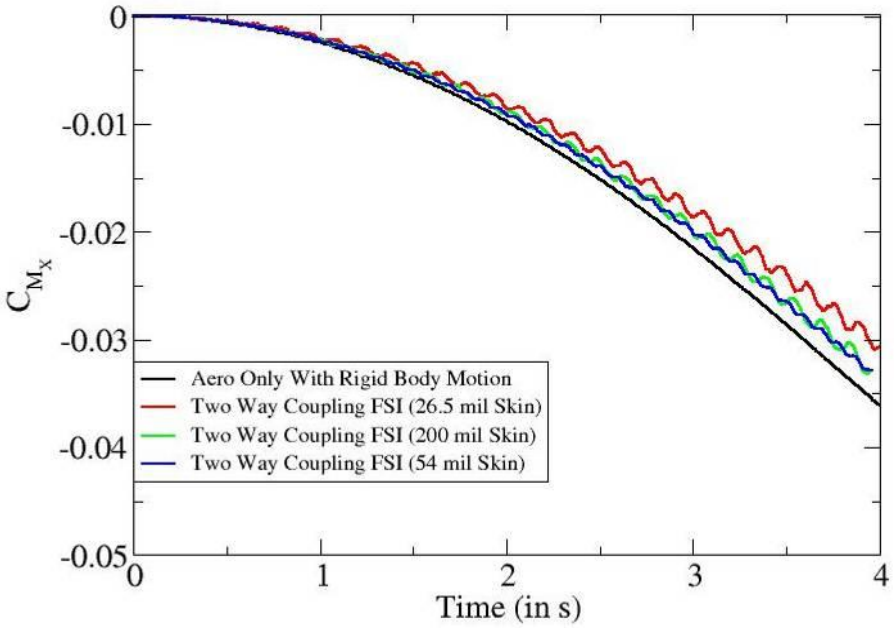

Figure 66. History of side moment coefficient in the x-direction during the aeroelastic dynamic simulation for various radial strap models

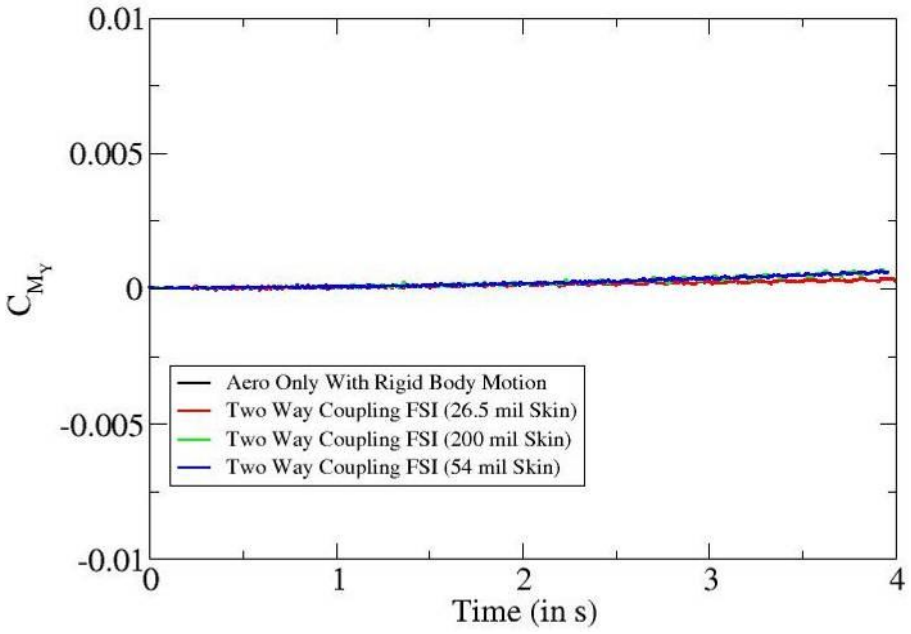

Figure 67. History of side moment coefficient in the y-direction during the aeroelastic dynamic simulation for various radial strap models

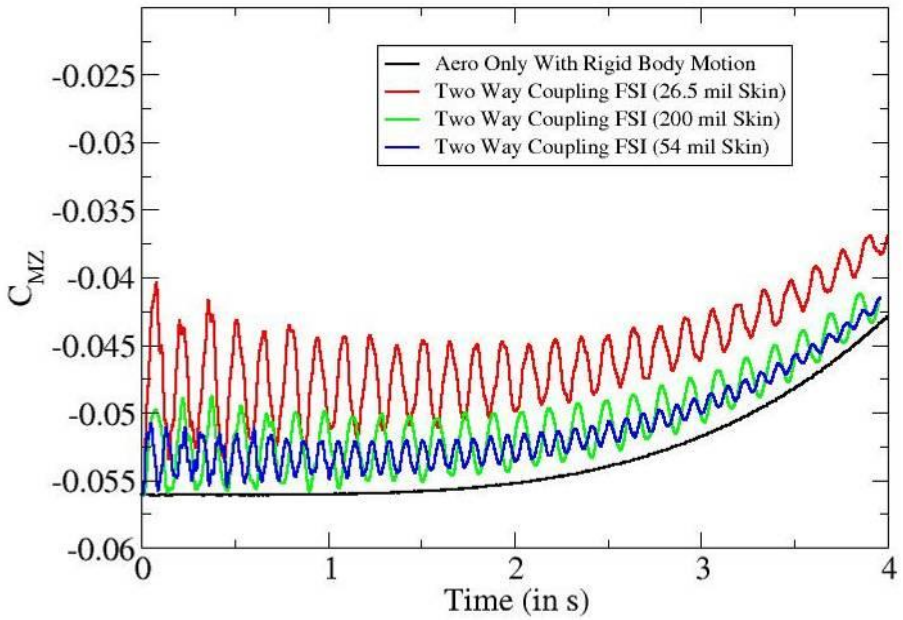

Figure 68. History of banking moment coefficient during the aeroelastic dynamic simulation for various radial strap models

6.3.2 Aeroelastic Structural Deformations

In this section, two sets of results are presented. First, the results obtained using CFD-averaged constant loads are shown. These will then be compared with the results obtained using the two-way coupling FSI to see the effects of the aerodynamic damping on the solution.

CFD-Averaged Constant Loads

The trace of displacement in the y-direction (direction of flow) at a point on the outer edge of the IAD for the two radial strap models is compared with the structural model without the radial strap and is shown in Figure 69. The displacement in x-direction is shown in Figure 70. As mentioned before, since the model is performing a banking maneuver, the x- and z-components of deflections contain both the aeroelastic deformations and the rigid body motion contribution. The y-component of deflection contains only the aeroelastic deformation since the model is not moving in this direction. The contribution of the aeroelastic deformation alone for the x-component and the z-component are shown in Figure 71 and Figure 72 respectively.

The results show that there is a significant reduction in oscillation of the x, y, and z component of displacement about their mean when the radial straps are taken into consideration. The results also indicate that the radial strap model with the 54 mil thickness and high E is more rigid than the others and is consequently the closest to the reference rigid body motion solution.

The aeroelastic deformation alone for the z-component in Figure 72 shows increasing amplitude of oscillations as the solution progresses. This increase is also present for both radial strap models although the magnitude of oscillations is smaller than the case without the radial strap. This increase in amplitude may be due to the effect of increasing rotational velocity of the IAD due to the constant acceleration of 5 deg/s^2 that is applied to the rigid front shield.

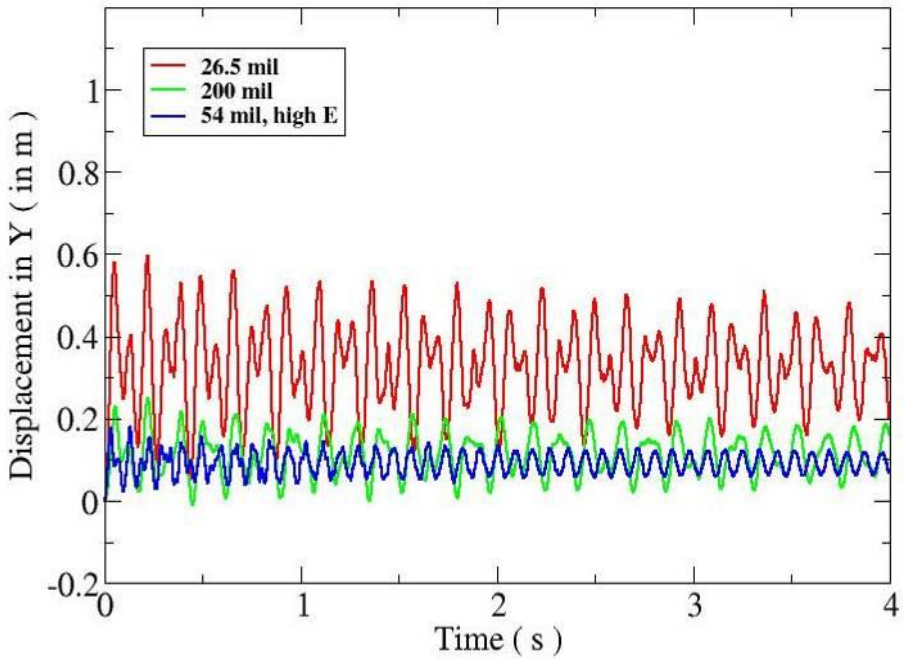

Figure 69 Comparison of y-component of structural deformation for various radial strap models.

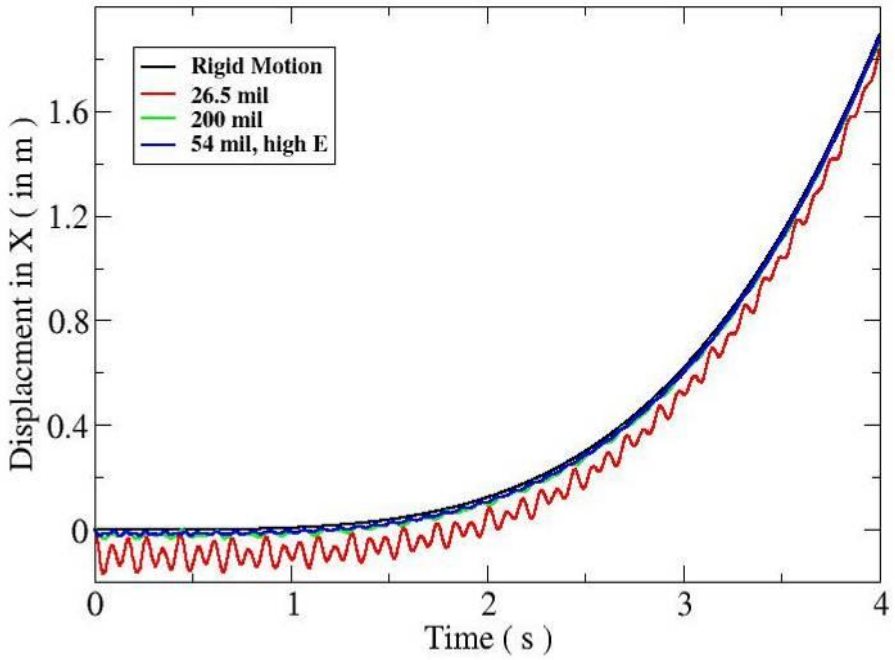

Figure 70 Comparison of x-component of structural deformation for various radial strap models.

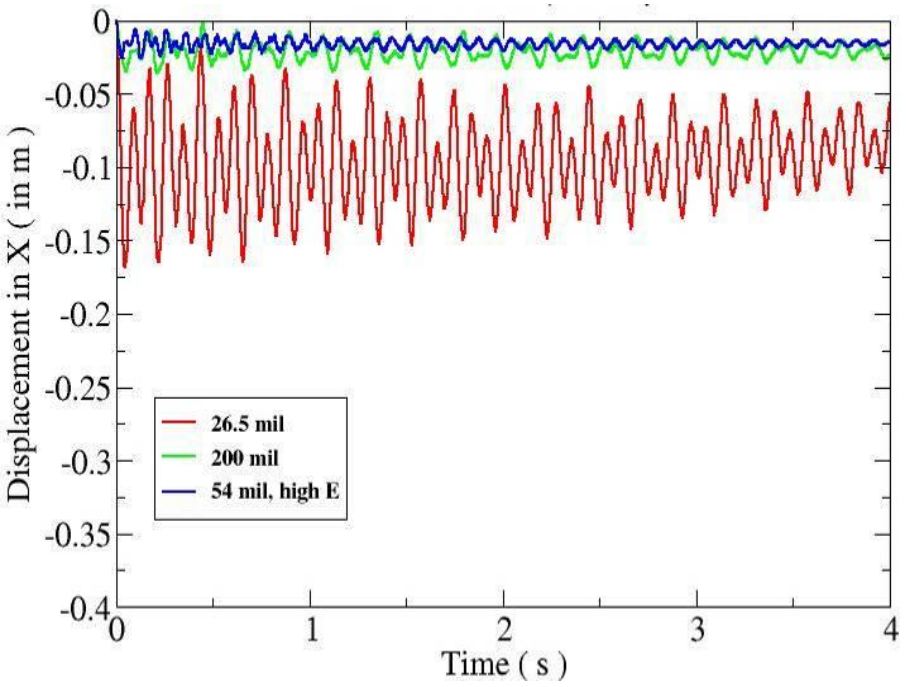

Figure 71 Comparison of aeroelastic component of structural deformation in the x-direction for various radial strap models.

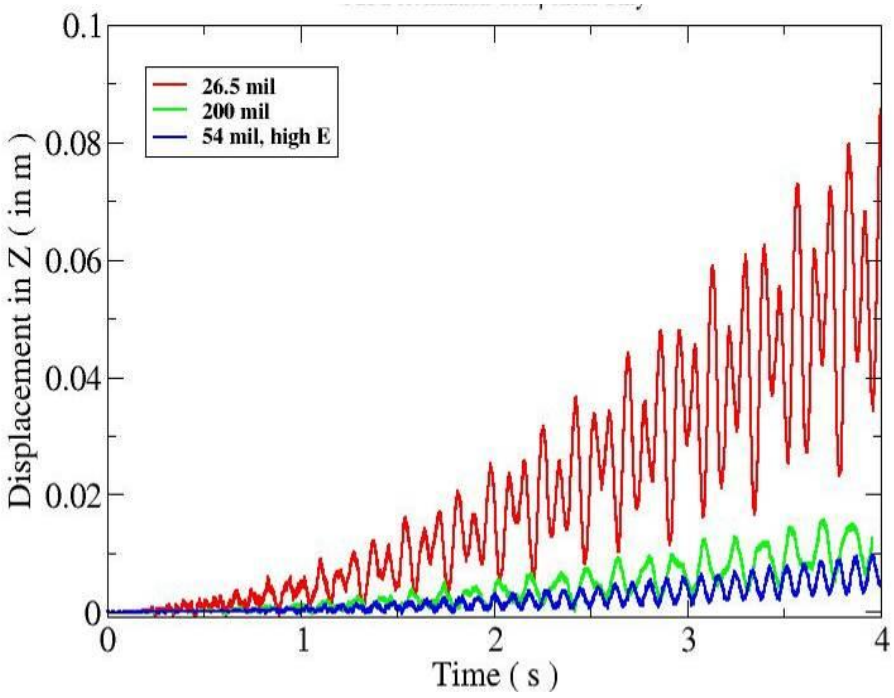

Figure 72 Comparison of aeroelastic component of structural deformation in the z-direction for various radial strap models.

Two-Way FSI Coupling

The trace of displacement in the y-direction (direction of flow) at a point on the outer edge of the IAD for the two radial strap models is compared with the structural model without the radial strap and is shown in Figure 73. The displacement in x-direction and z-direction are shown in Figure 74 and Figure 75, respectively. The contribution of the aeroelastic deformation alone for the x-component and the z-component are shown in Figure 76 and Figure 77, respectively.

The results show that there is a further reduction in oscillation of the x, y, and z component of displacement about their mean compared to the cases with averaged constant CFD loading. That is clearly due to aerodynamic damping. The results also indicate that the radial strap model with the 54 mil thickness and high E is more rigid than the others and is consequently the closest to the reference rigid body motion solution.

As seen before in the test with constant CFD-averaged loads, the aeroelastic deformation alone for the z-component in Figure 77 shows increasing amplitude of oscillations as the solution progresses. However, due to the effect of aerodynamic damping, the amplitude of oscillations are smaller compared to the results from the constant averaged CFD loads.

Fast Fourier Transforms (FFT) of aeroelastic component of the x-displacement and the y-displacement were performed. The plots of the power spectral density (PSD) of all the cases considered in this subtask are shown in Figure 78 and Figure 79. The first and second modes of the IAD for the various models are shown in Table 6.

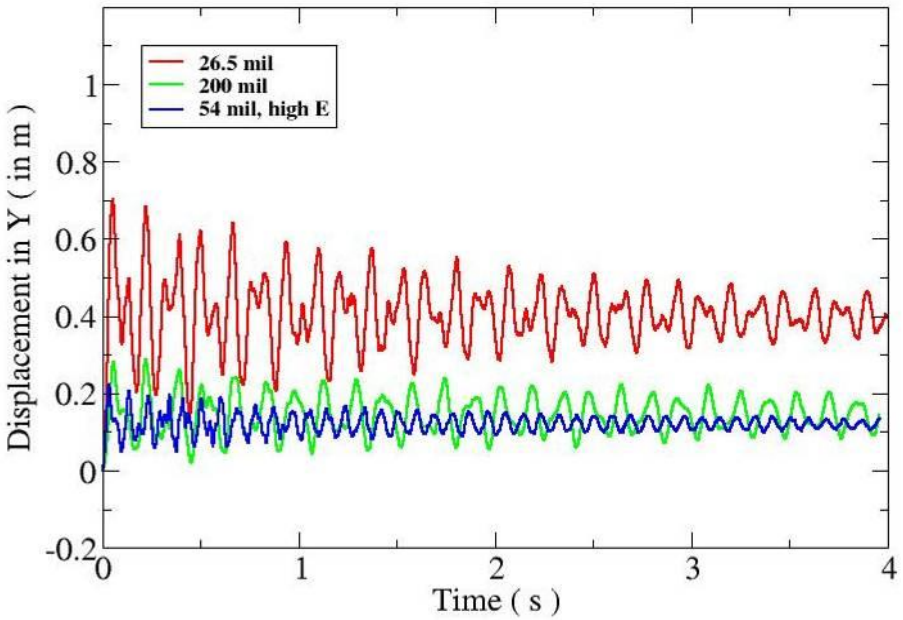

Figure 73 Comparison of y-component of structural deformation for various radial strap models.

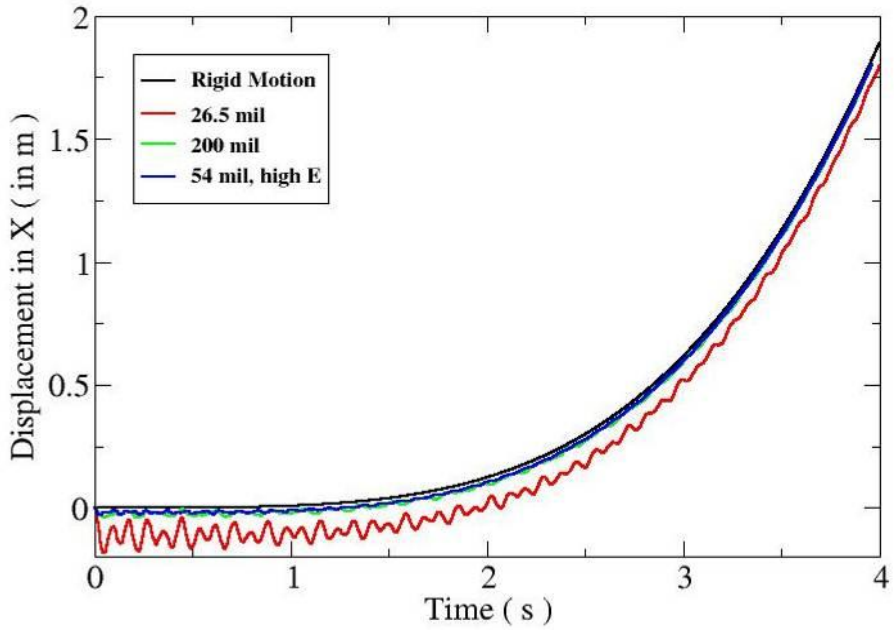

Figure 74 Comparison of x-component of structural deformation for various radial strap models.

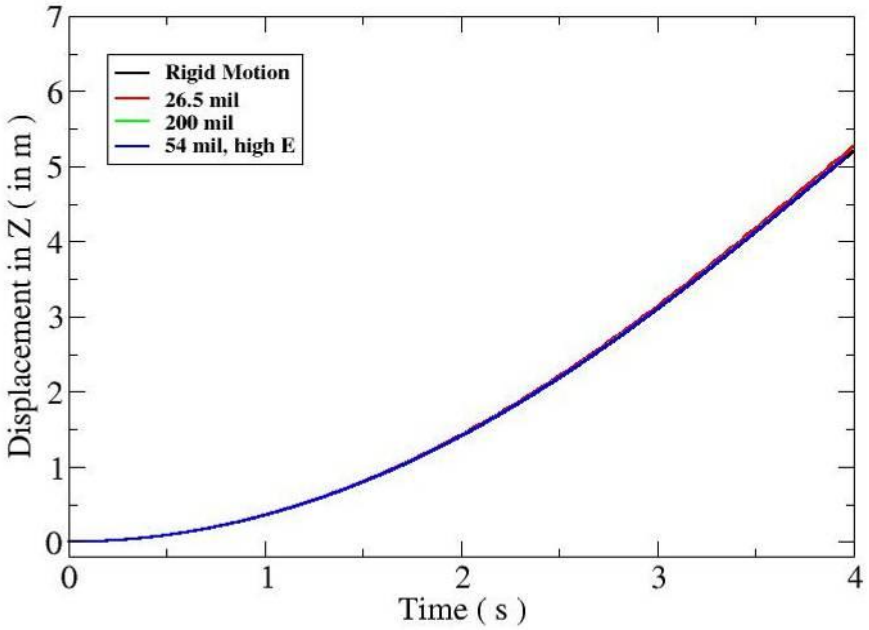

Figure 75 Comparison of z-component of structural deformation for various radial strap models.

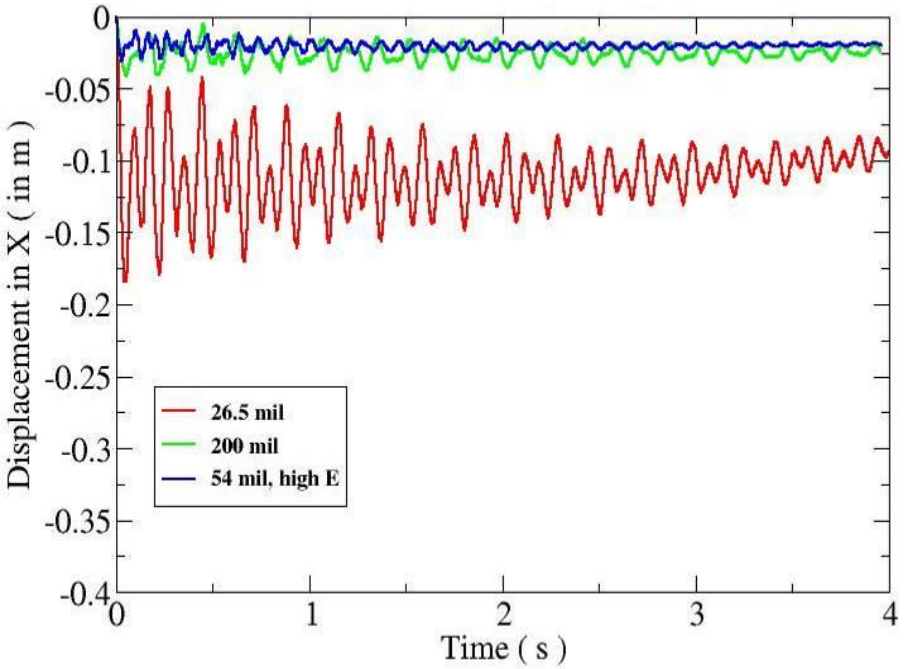

Figure 76 Comparison of aeroelastic component of structural deformation in the x-direction for various radial strap models.

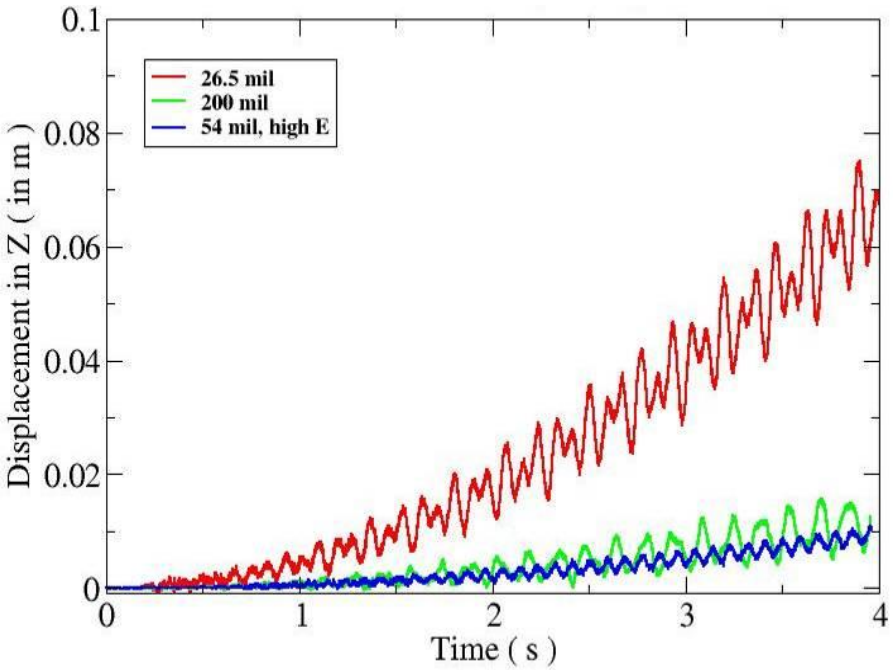

Figure 77 Comparison of aeroelastic component of structural deformation in the z-direction for various radial strap models.

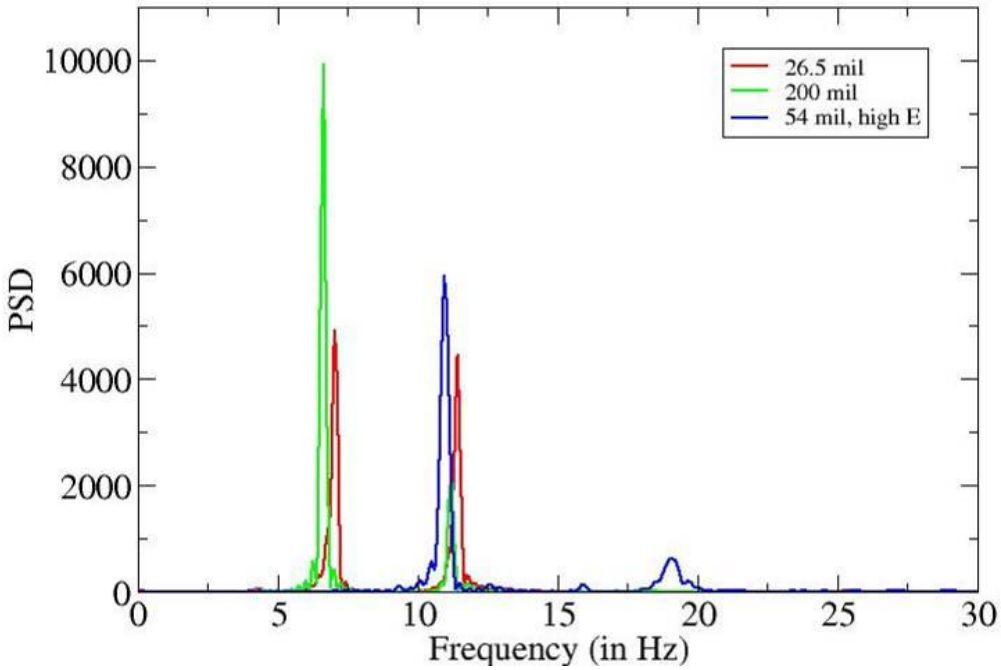

Figure 78 Comparison of PSD based on y-component of structural deformation for various radial strap models.

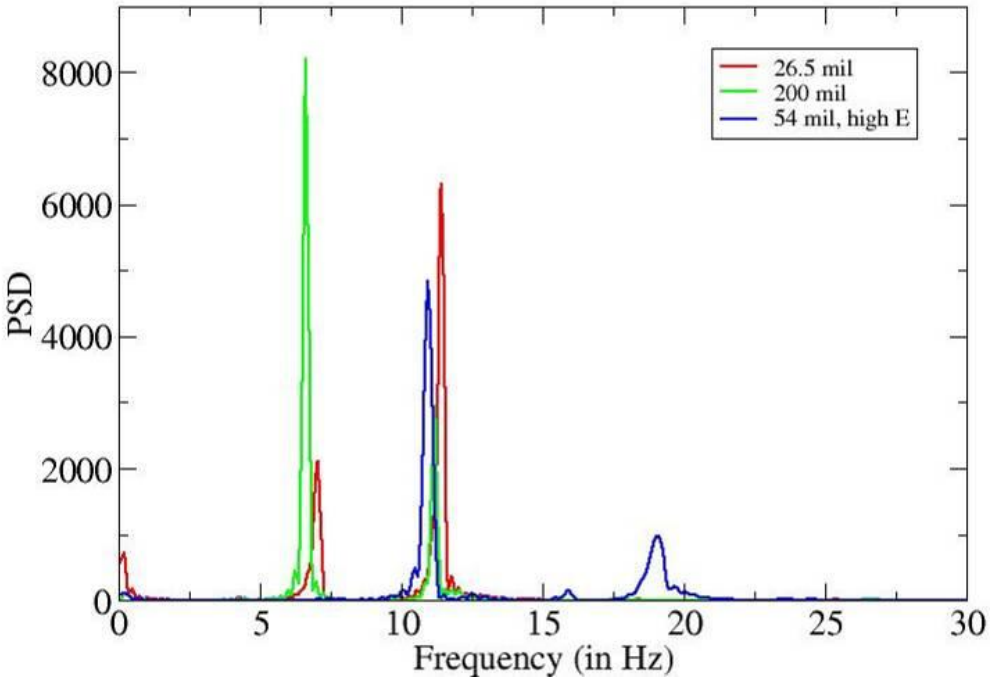

Figure 79 Comparison of PSD based on aeroelastic component of structural deformation in the x-direction for various radial strap models.

Table 6 First two modes of the IAD for various strap models

Model	26.5 mil	200 mil	54 mil, high E
1st, 2nd Frequencies (Hz)	7.069, 11.44	6.63, 11.17	10.94, 19.1

6.3.3 Structural von Mises Stresses

In this section, von Mises stress results obtained using the two-way coupling are presented. The time trace of von Mises stress results on the toroids is presented in Figure 80. The figure also shows that the von Mises stress is cyclic, similar to the structural deformations. The stress in the baseline 26.5 mil model is fluctuating between a maximum value of 5 E+08 N/m^2 and a minimum value of 1.5 E+08 N/m^2. Since the yield stress of the Kevlar material is 35 GPa, the stress levels are way below the yield stress of the material. As seen in the previous sections, the effect of increasing the skin thickness is to reduce the overall deformation of the IAD. This is reflected in the factor-of-two reduction for the stress developed in the toroids for the cases with the thicker skin and high E.

The time history of von Mises stress results on the cover (skin/gore) is presented in Figure 81. The von Mises stress on the skin is also cyclic, and is fluctuating between a maximum value of 1.5 E+08 N/m^2 and a minimum value of 5E+07 N/m^2 for the baseline 26.5 mil case. In case of the cover, a factor-of-ten reduction is seen in the stress for the 200 mil skin case when compared to the baseline 26.5 mil case. The stress developed in the 54 mil skin is higher due to the higher

Young's Modulus (E) of 19.6E+9 used in that case. Even though the strain developed in the 54 mil case is small, the higher E implies that the stress is also numerically higher.

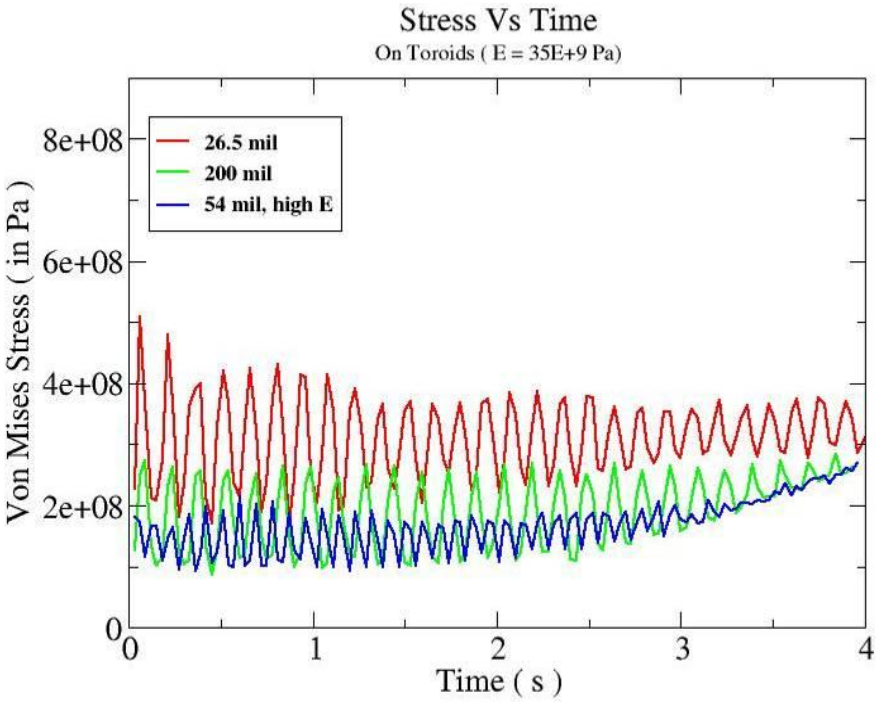

Figure 80 Comparison of von Mises stresses on the toroids for various radial strap models.

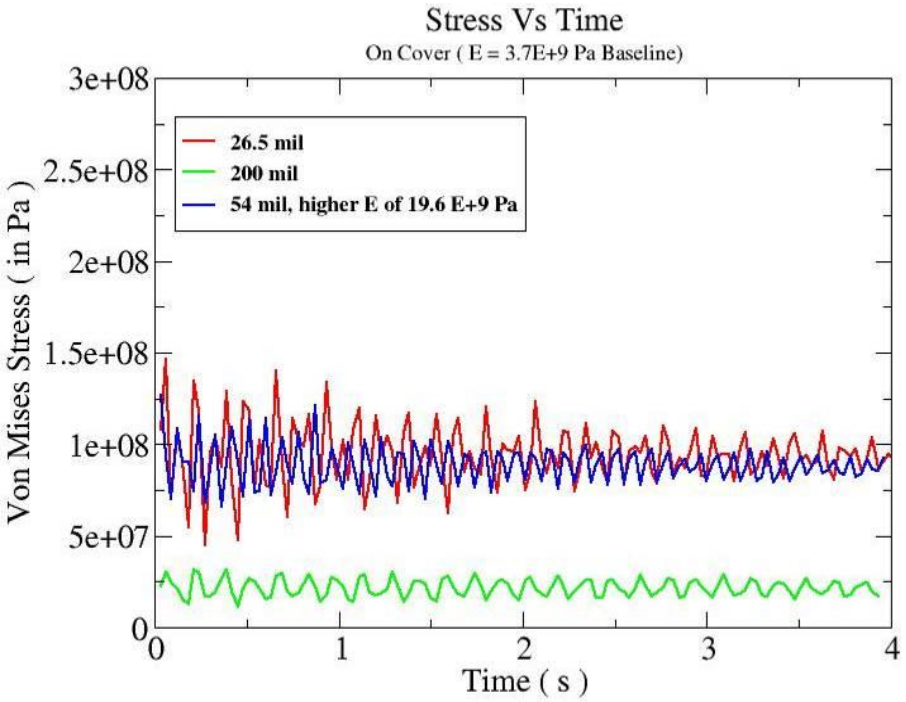

Figure 81 Comparison of von Mises stresses on the cover (gores/skin) for various radial strap models.

Snapshots of peak von Mises stresses on the front surface of the toroids and the cover (gore/skin) for the various models are shown in Figure 82. The peak stress levels occur at the windward side of the front surface of the toroids. For the cover, the peak values of stresses occur around the inner circle of the model near the location of the adapter.

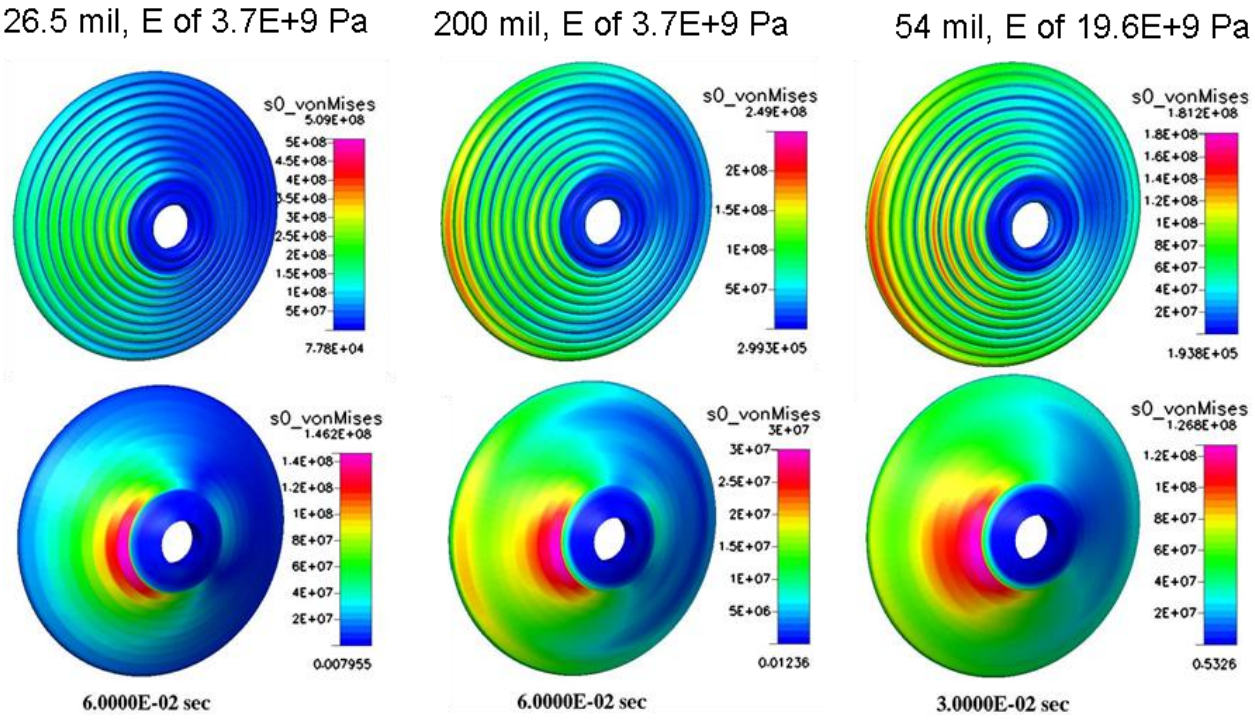

Figure 82 Snapshots of peak von Mises stresses on the toroids and cover (gores/skin) for various radial strap models.

6.4 Summary

To speed up the computation, coarser models were developed for dynamic fluid structure coupling of IAD. Their fidelity was verified vs. the fine grid model. Simulations were conducted to investigate the effect of increasing the toroid inflation pressure. It was seen that it only has a small impact on overall deformation, keeping in line with the steady results obtained in Task 1. Aeroelastic response of the IAD was tested after adding the radial straps to the IAD by making changes to the thickness and material properties of the IAD Cover (gore/skin). Both CFD constant averaged loads and two-way FSI coupling were used. It was seen that the deflections of the IAD are reduced dramatically when effect of radial straps are added to the model. But as noted in the previous chapter, even without the straps, von Mises stresses are still far less than the yield stress of the Gores and toroids materials.

7 AEROELASTIC AND DYNAMIC ANALYSIS OF A SINGLE STACK IAD CONFIGURATION

In this effort, CFDRC developed three-dimensional computational models based on a modified design for the IAD. The main design change involved using a single row of toroids, instead of two rows of toroids used in the previous tasks. The new model is referred to in this report as a single stack(ed) model. The other design changes were to the thicknesses of the toroids and the cover of the IAD model. Materials and their properties were unchanged. These models were then used to conduct aero-structural and dynamic simulations of the IAD model at 30 degrees angle of attack and bank angle rate of 5 deg/sec^2. Simulations were carried out for up to 4 seconds. An effort was also made to understand the effect of inflation pressure and the dynamic maneuver. The following aero-structural simulations were conducted in this effort:

4. ***Effect of toroid inflation pressure and banking maneuver on the dynamic response of the IAD the using average constant CFD loading***. In this case, the average CFD loads on several patches of the model are applied to the FEM model and the structural responses are computed during the dynamic maneuver for various toroid internal pressures. The results were compared with the double stack model as well.
5. ***Effect of the single stack IAD model on the dynamic response of the IAD using two-way aeroelastic FSI coupling***. In this case, the dynamic response of single stack model was compared with the double stack model for the same banking maneuver and loads.

7.1 Computational Fluid Dynamics Model for Single Stack IAD Configuration

The computational grid model of the single stack IAD was developed using the grid generator CFD-GEOM. The overall computational grid is shown in Figure 83. As shown in the figure, the computational grid model of the IAD is overset over a background grid to enable the dynamic bank maneuvering. The computational grid of the IAD model is shown in red, while the background grid is shown in blue. Although the geometrical model is symmetric, the computational grid was developed and the simulations were conducted on a full 360 degrees three-dimensional model due to the banking dynamic maneuver that will be considered in this effort. The CFD grid of the modified single stack IAD model is compared with the nominal double stack model in Figure 84.

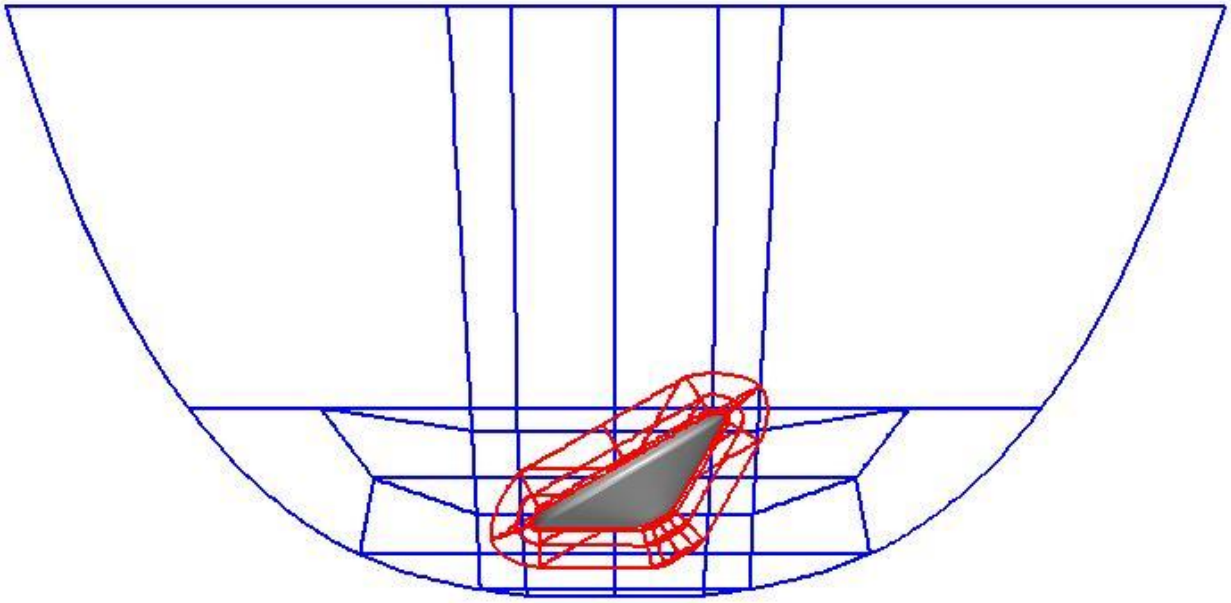

Figure 83. Overall computational grid boundaries for the modified design.

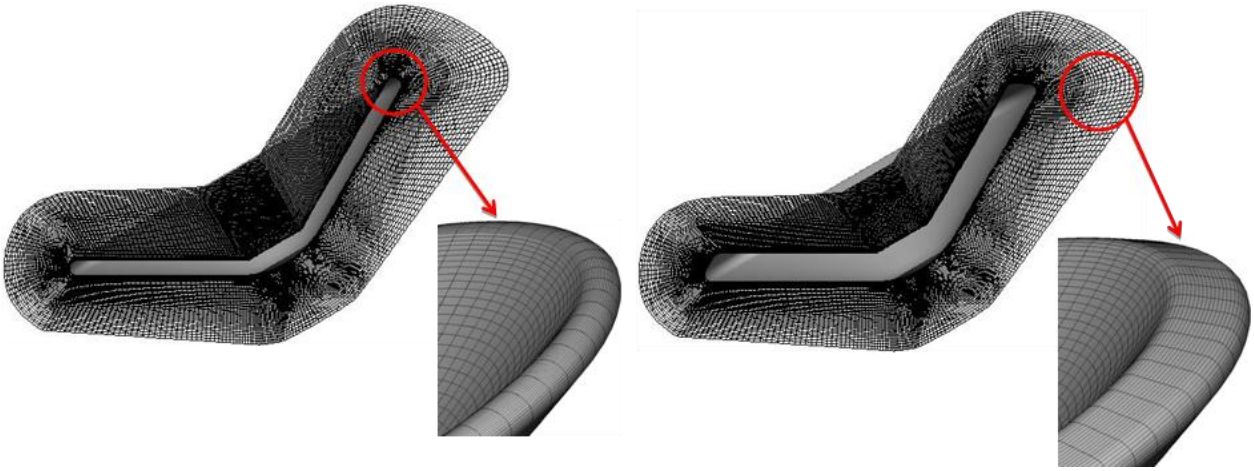

(a) Single stack model (b) Double stack model

Figure 84 Single and double stack CFD models

7.2 Computational Structural Dynamics Model for Single Stack IAD Configuration

The computational structural FEM model of the single stack IAD configuration is compared with the double stack configuration in Figure 85. The new model consists of 18,500 quad shell elements of non-zero thickness. The toroids are modeled with 12 quad shell elements each. The toroids are connected together through one of the 12 elements, and they are also connected with the gores (the outside skin/cover) through one segment.

The toroids are made of Kevlar and the gores are made of Upilex. The material properties of the Kevlar and the thickness of the toroids are shown in Table 7. The material properties of the

Upilex and the thickness of the gores are shown in Table 8. A high temperature knock down factor of 0.5 is used for the toroids modulus of elasticity. The toroid thickness is assumed to be 8.6 mil to take account of the 6 circumferential straps that are present in each toroid. The notional toroids inflation pressure is assumed to be 30 KPa. To account for the 18 radial straps over the cover, the thickness of the cover is set to 53.2 mil and the effective young's modulus increased to 18.5 GPa.

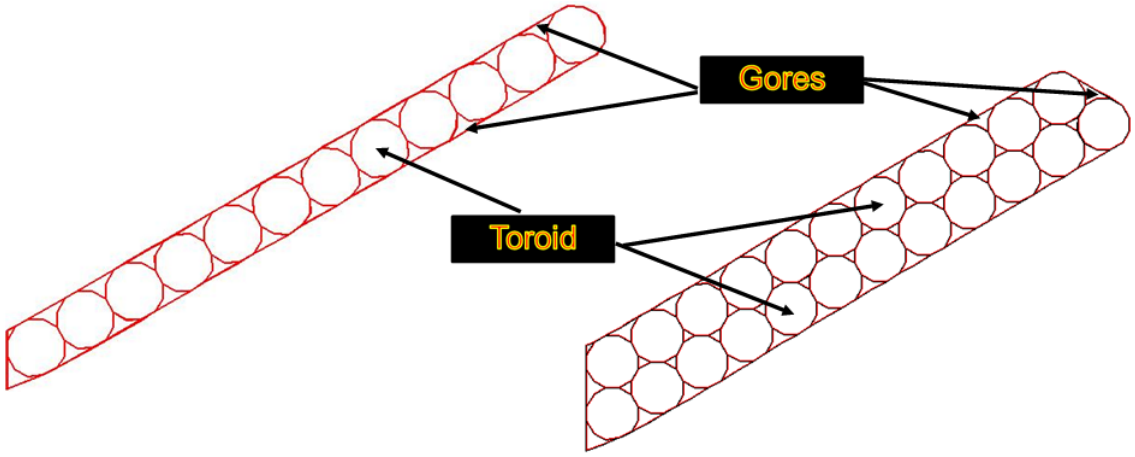

Figure 85. Computational FEM model of the single stack IAD configuration compared to the double stack configuration.

Table 7. Material properties of the toroids for the single stack IAD configuration.

Kevlar Properties for Toroids	
Max E	70 E+09 Pa
Design E	35 E+09 Pa
Density	1440 Kg/m^3
Poisson ratio	0.1
Toroids thickness	5.13 Mil (w/o circumferential straps)

Table 8. Material properties of the gores for the single stack IAD configuration.

Upilex Properties for Gores	
E	3.7 E+09 Pa
Density	1470 Kg/m^3
Poisson ratio	0.34
Gores thickness	26.536 Mil

7.3 Steady State Aerodynamic Simulation Results of Single Stack IAD Configuration

The previously described aerodynamic model with the flow and flight conditions for the simulation previously given in Table 3 was used to simulate the aerodynamic flowfield around the new single stack IAD model.

The overall pressure and mach contours over the symmetry plane of the whole computational domain are shown in Figure 86 and Figure 87, respectively. A maximum pressure of about 8500 Pa occurs over the front shield of the model and in front of the oncoming flow. The surface pressure contours over the front of the IAD surface is shown in Figure 88. The maximum pressure occurs nears the windward side of the model and decreases toward the leeward side. The pressure profiles on the front surface for the double stack and single stack models are nearly identical. The pressure in the back of the model is very small compared to the front side. There are small differences in pressure profiles between the single and double stack models as shown in Figure 89.

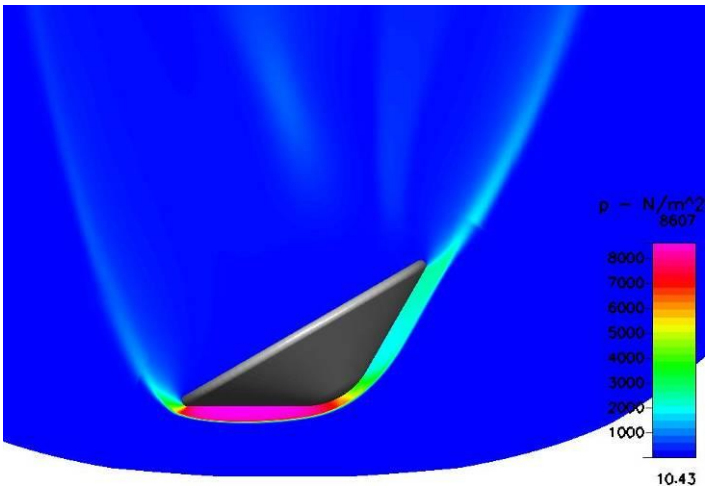

Figure 86 Steady state pressure field around the single stack IAD model

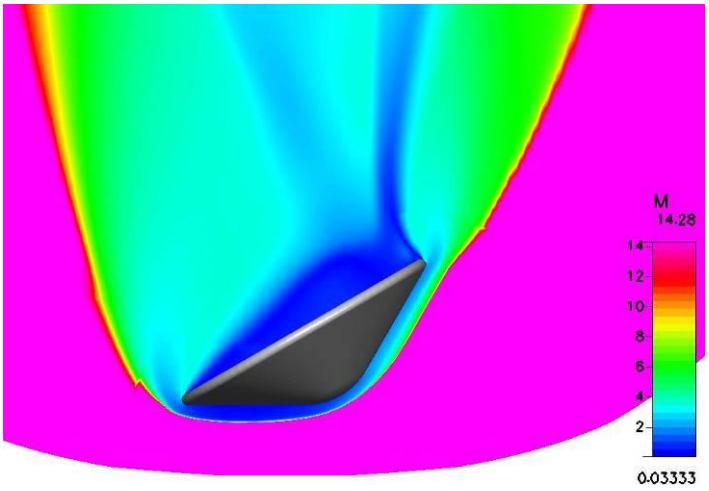

Figure 87 Steady state Mach number field around the single stack IAD model

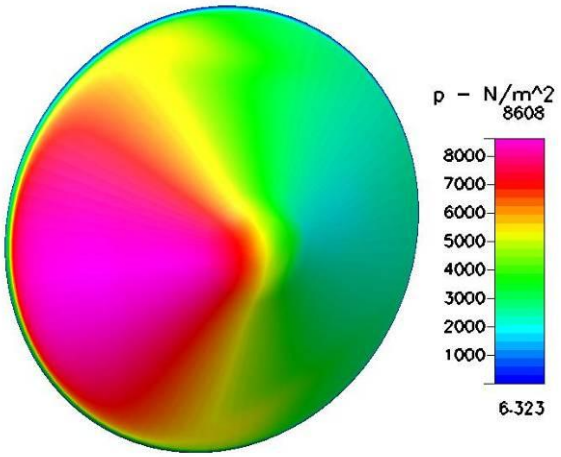

Figure 88 Pressure contours on the front surface of the single stack IAD model

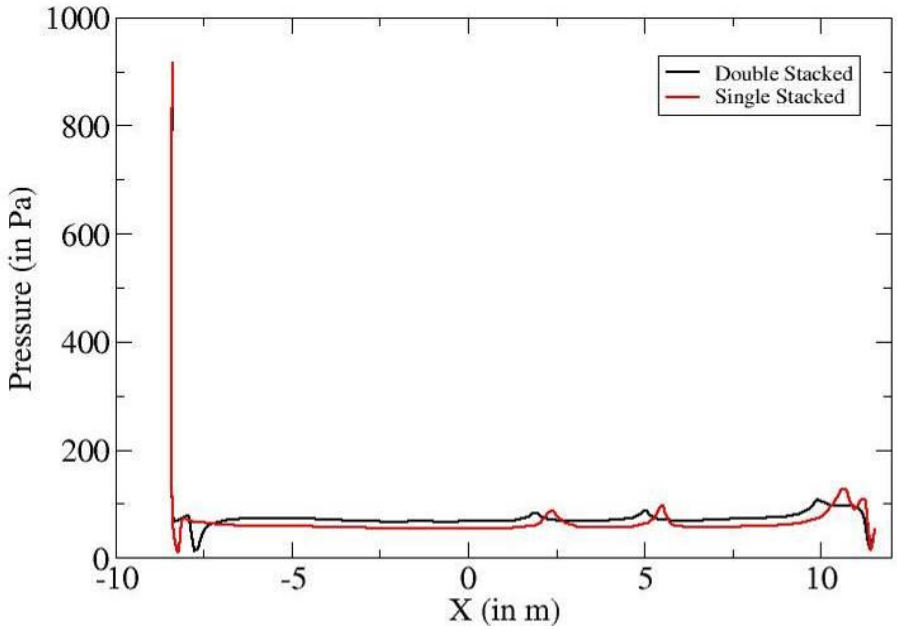

Figure 89 Comparison of pressure profiles on the back of the single stack and double stack models

7.4 Transient FEM Simulation of the Single Stack IAD Dynamics

In this subtask, transient FEM simulations of the single stack IAD model were conducted at different inflation pressures using the average constant CFD loading. The inflation pressures considered were 15 and 30 KPa. The results were compared against the rigid body motion and the double stack IAD model with the radial strap model that was developed in Task 3. All simulations were started from an undeformed initial state. The aeroelastic dynamic simulation with average constant CFD loading was conducted for about 4 seconds of simulation.

7.4.1 Comparison of Structural Deformations

The plot of displacement in the y-direction (direction of flow) at the outer edge of the IAD for the three inflation pressures applied is shown in Figure 90. The displacement in x-direction and z-direction are shown in Figure 91 and Figure 92. Since the model is performing a banking maneuver, the x- and z-components of deflections contain both the aeroelastic deformations and the rigid body motion contribution. The y-component of deflection contains only the aeroelastic deformation since the model is not moving in this direction. The contribution of the aeroelastic deformation only for the x and z components are shown in Figure 93 and Figure 94.

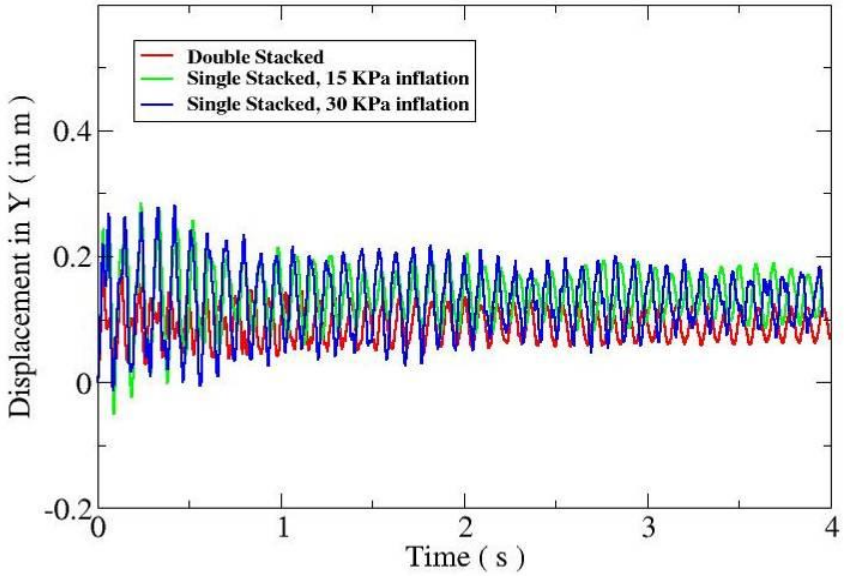

Figure 90 Comparison of y-component of structural deformation for double and single stack configurations with two different inflation pressures.

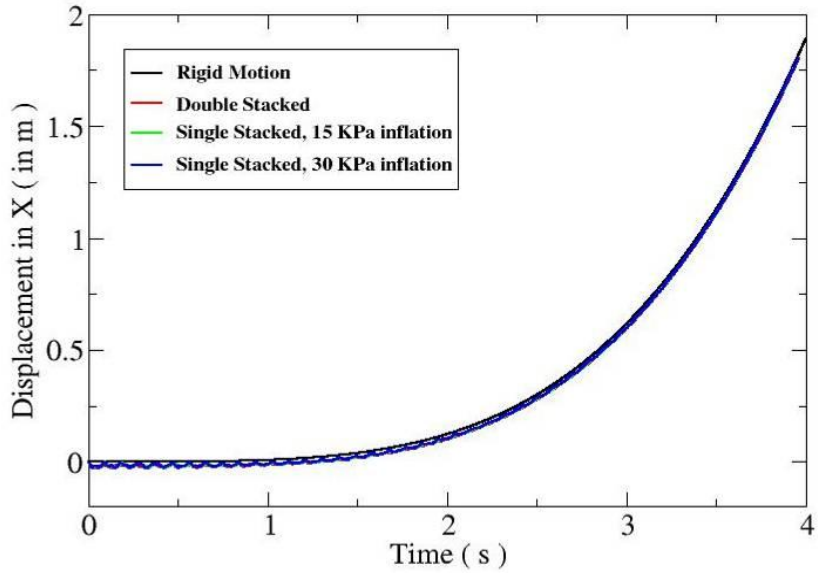

Figure 91 Comparison of x-component of structural deformation for double and single stack configurations with two different inflation pressures.

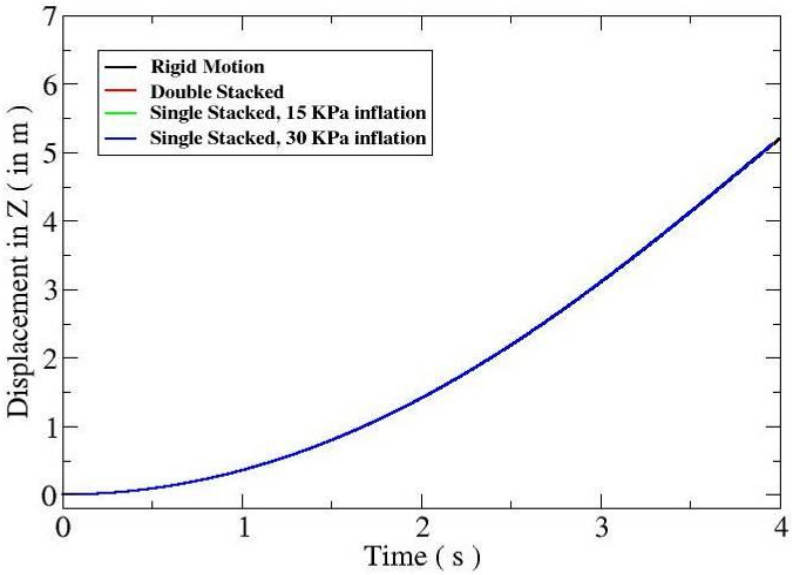

Figure 92 Comparison of z-component of structural deformation for double and single stack configurations with two different inflation pressures.

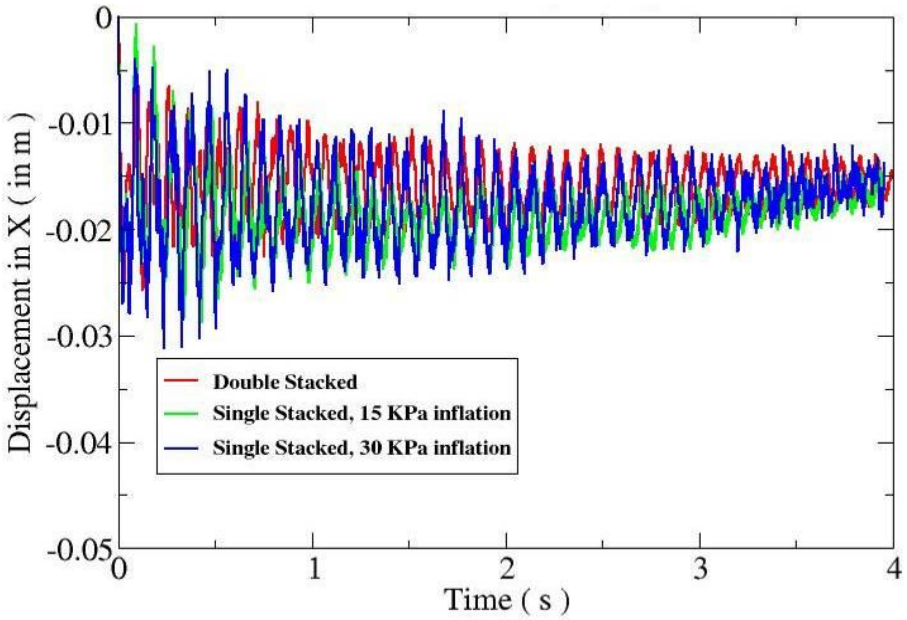

Figure 93 Comparison of aeroelastic component only of structural deformation in the x-direction for double and single stack configurations with two different inflation pressures.

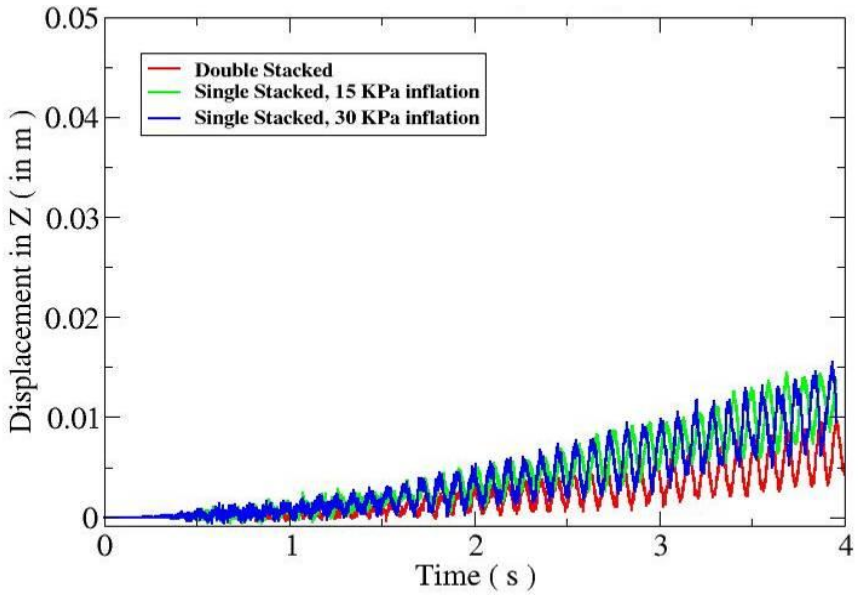

Figure 94 Comparison of aeroelastic component only of structural deformation in the z-direction for double and single stack configurations with two different inflation pressures.

Just like results in previous chapters, the results show that the overall deformation of the model is reduced by about 4 to 7 % in response to an increase in inflation pressure of 50 to 100%. This is keeping in line with the results obtained in task 1 for steady state deformation response to increase in pressure.

Fast Fourier Transforms (FFT) of aeroelastic component of the y-displacement were performed. The plots of the power spectral density (PSD) of all the cases considered in this subtask are shown in Figure 95. It can be seen that the frequencies are quite similar.

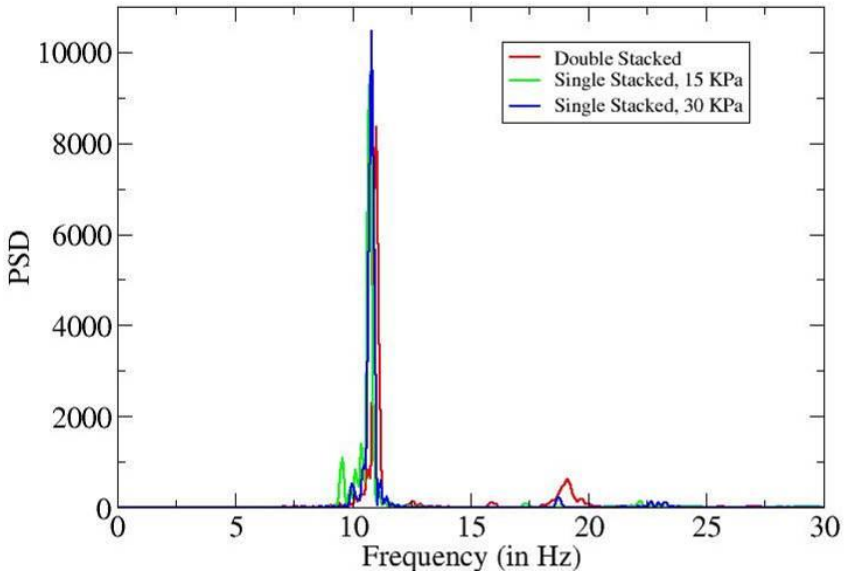

Figure 95 Comparison of PSD based on y-component of structural deformation for double and single stack configurations with two different inflation pressures.

The effect of the dynamic maneuver is discussed next. As seen before in previous tasks, the aeroelastic deformation alone for the z-component in Figure 94 shows increasing amplitude of oscillations as the solution progresses. To understand this, one case was run without any dynamic maneuver. The contribution of the aeroelastic deformation only for the x and z components are compared with the previous results and are shown in Figure 96 and Figure 97.

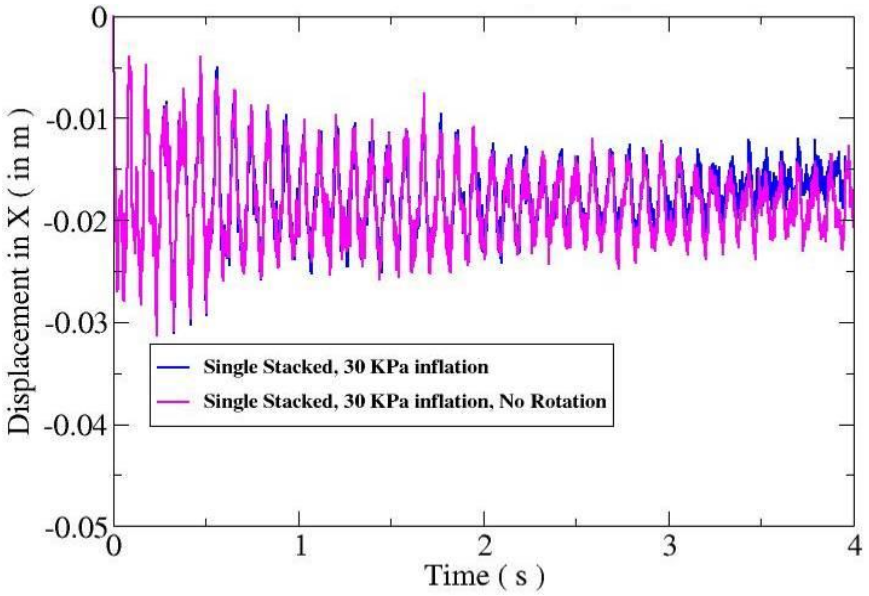

Figure 96 Comparison of aeroelastic component only of structural deformation in the x-direction with and without dynamic maneuver.

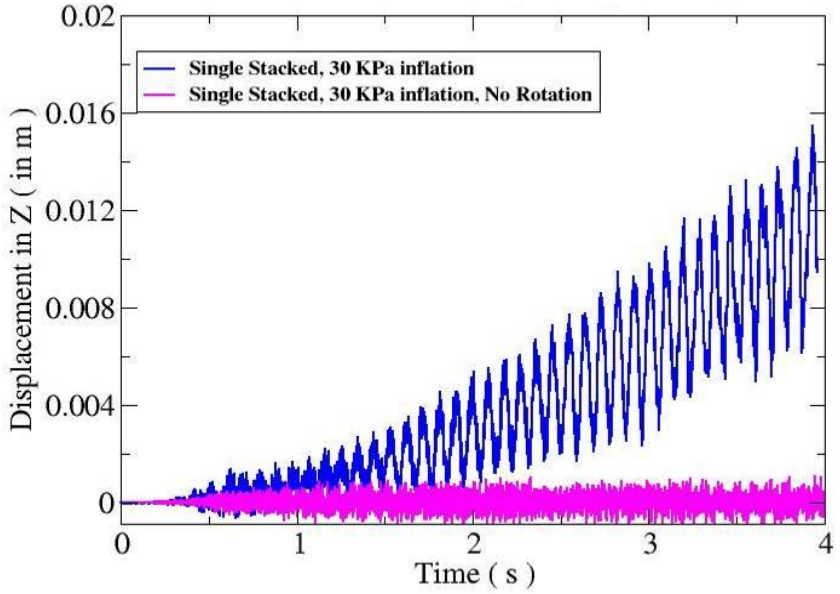

Figure 97 Comparison of aeroelastic component only of structural deformation in the z-direction with and without dynamic maneuver.

For the case without dynamic rotation, the magnitude of the high frequency oscillations in the z deflection component in Figure 97 is of the order of the thickness of the IAD cover and toroids. Therefore, it is clear that the increase in the mean displacement in the z-direction is primarily due to the effect of the dynamic maneuver.

7.4.2 Comparison of Structural von Mises Stress

In this section, von Mises stress results obtained using the averaged constant loads are presented. The time history of von Mises stress results on the toroids is presented in Figure 98. The figure also shows that the von Mises stress is cyclic, similar to the structural deformations. The stress in the baseline double stacked model is fluctuating between a maximum value of 2 E+08 N/m^2 and a minimum value of 1 E+08 N/m^2. Since the yield stress of the Kevlar material is 35 GPa, the stress levels are way below the yield stress of the material. As seen in the previous sections, the effect of the single stack model is to increase the overall deformation of the IAD. This is reflected in increase in the stress developed in the toroids for the single stack cases.

The time history of von Mises stress results on the cover (skin/gore) is presented in Figure 99. The von Mises stress on the skin is also cyclic, and is fluctuating between a maximum value of 1.25 E+08 N/m^2 and a minimum value of 7E+07 N/m^2 for the baseline double stack case. In case of the cover, a factor-of-two increase is seen in the stress for the single stack case.

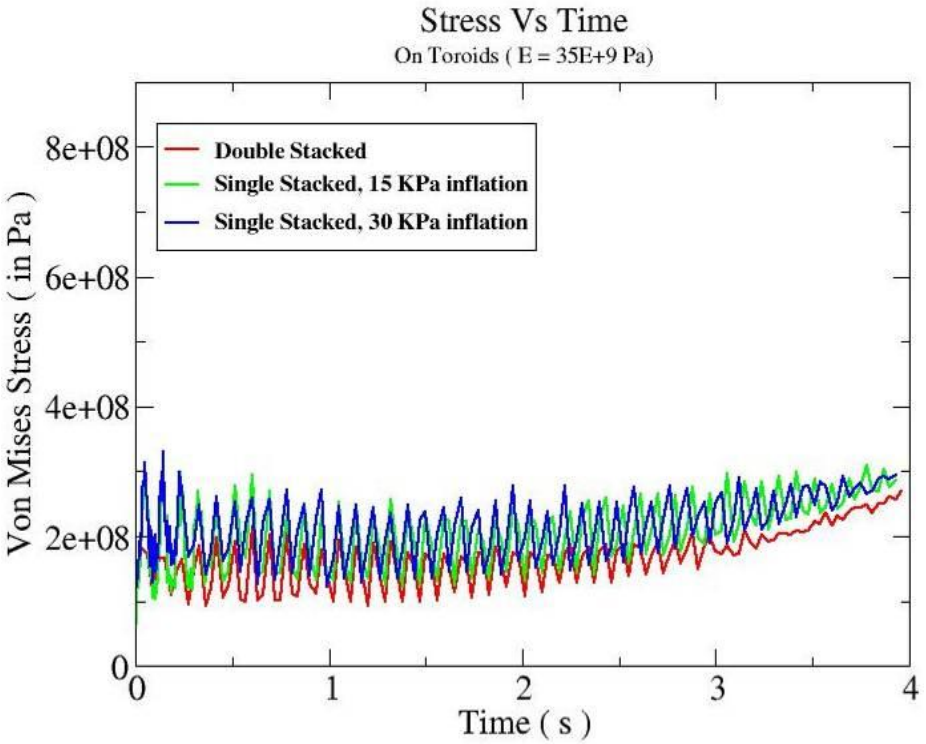

Figure 98 Comparison of von Mises stresses on the toroids for double and single stack configurations with two different inflation pressures.

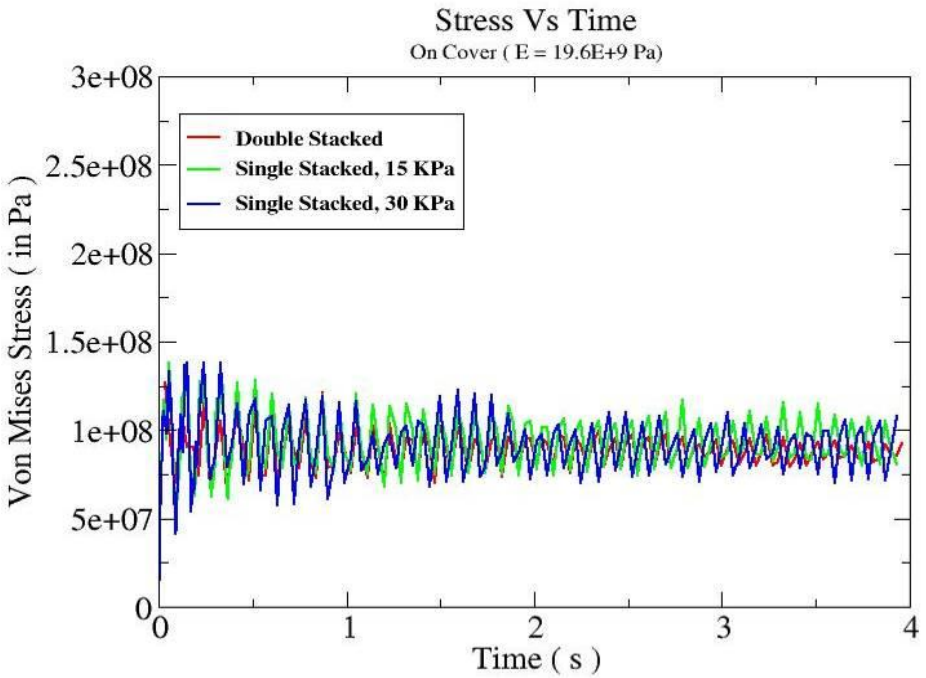

Figure 99 Comparison of von Mises stresses on the cover (gores/skin) for double and single stack configurations with two different inflation pressures.

7.5 Transient Two-Way FSI Simulation of the Single Stack IAD Dynamics

In this subtask, the single stack IAD model was run with a design inflation pressure of 30 KPa using two way FSI coupling. All simulations were started from an undeformed initial state. The simulations with two-way FSI coupling were conducted for 4 seconds of simulation. The results were compared to the double stack model with radial straps, with the rigid body motion and the results from the constant averaged CFD loads from the last subtask.

7.5.1 Aerodynamic Forces and Moments

The histories of the aerodynamic forces and moments during the aeroelastic dynamic simulation are shown in Figure 100 - Figure 105. The results of the two-way coupling methods using the single stack configuration is compared with the double stack case and with the aerodynamic coefficients of aerodynamic simulation with rigid-body motion for reference. The histories of the lift and drag coefficients during the aeroelastic dynamic simulation are shown in Figure 100 and Figure 101, respectively. The history of the side force coefficient is shown in Figure 102. The histories of the side moment coefficients and banking moment coefficients are shown in Figure 103, Figure 104 and Figure 105.

All the results show damping of the oscillations as the simulation progresses, due to aerodynamic damping, indicating the structure is aeroelastically stable. The results also indicate that the single stack configuration shows very little difference from the double stack configuration in terms of aerodynamic response and that they are both close to the reference rigid body motion solution.

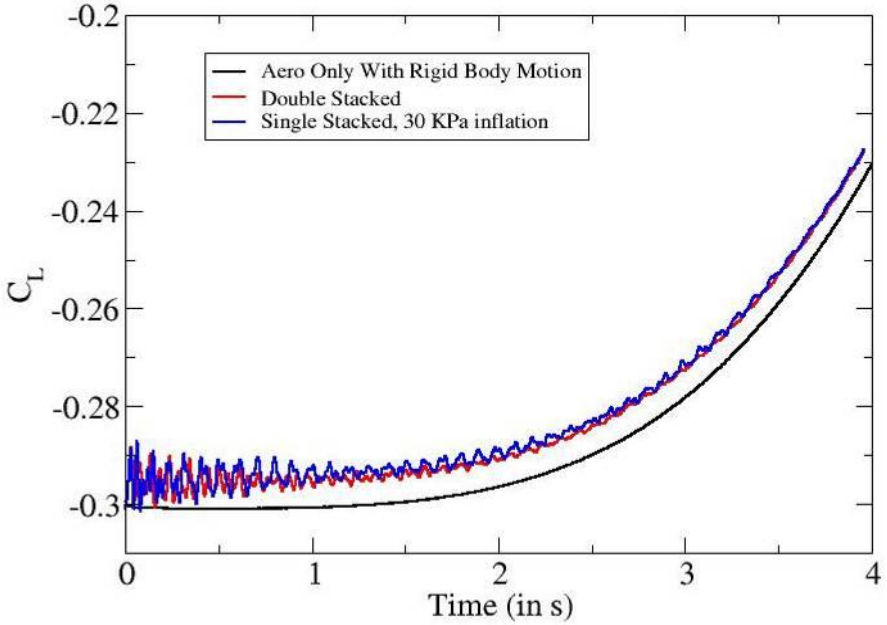

Figure 100. History of coefficient of lift during the aeroelastic dynamic simulation for single and double stack configurations

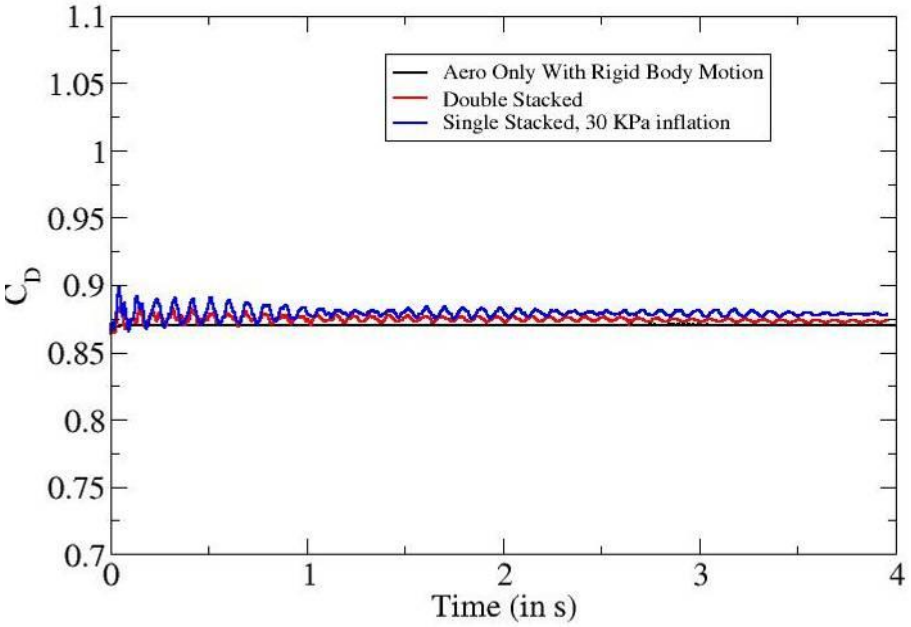

Figure 101. History of coefficient of drag during the aeroelastic dynamic simulation for single and double stack configurations

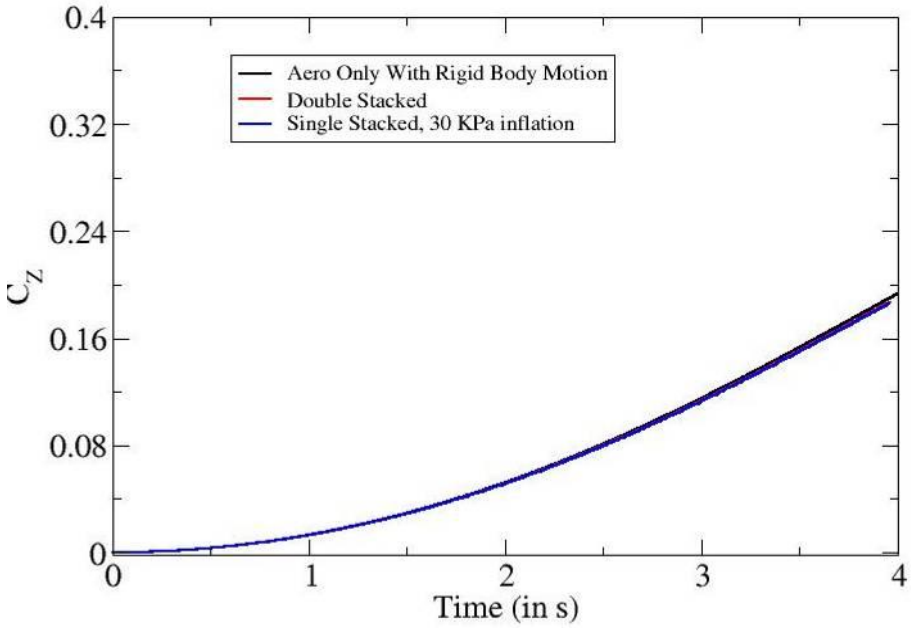

Figure 102. History of side force coefficient during the aeroelastic dynamic simulation for single and double stack configurations

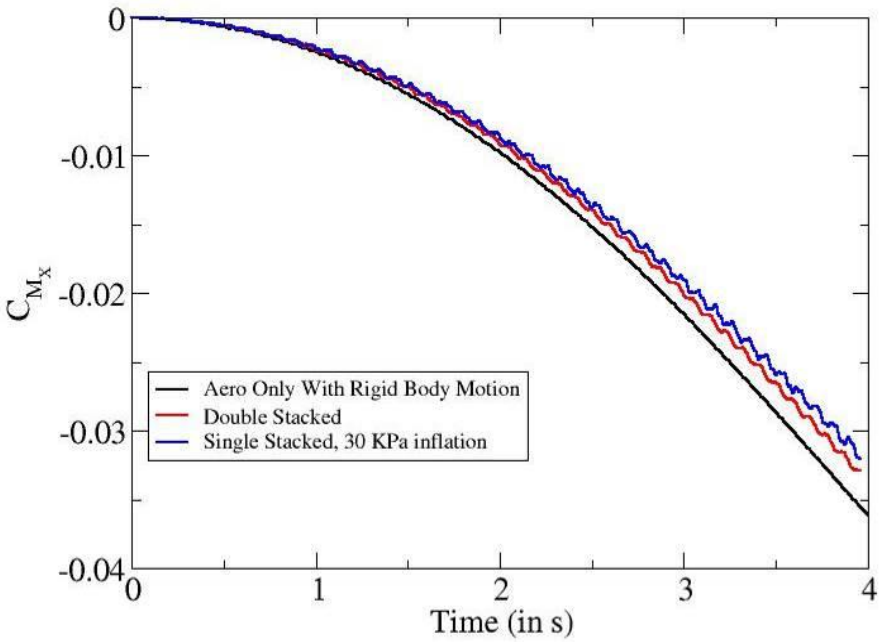

Figure 103. History of side moment coefficient in the x-direction during the aeroelastic dynamic simulation for single and double stack configurations

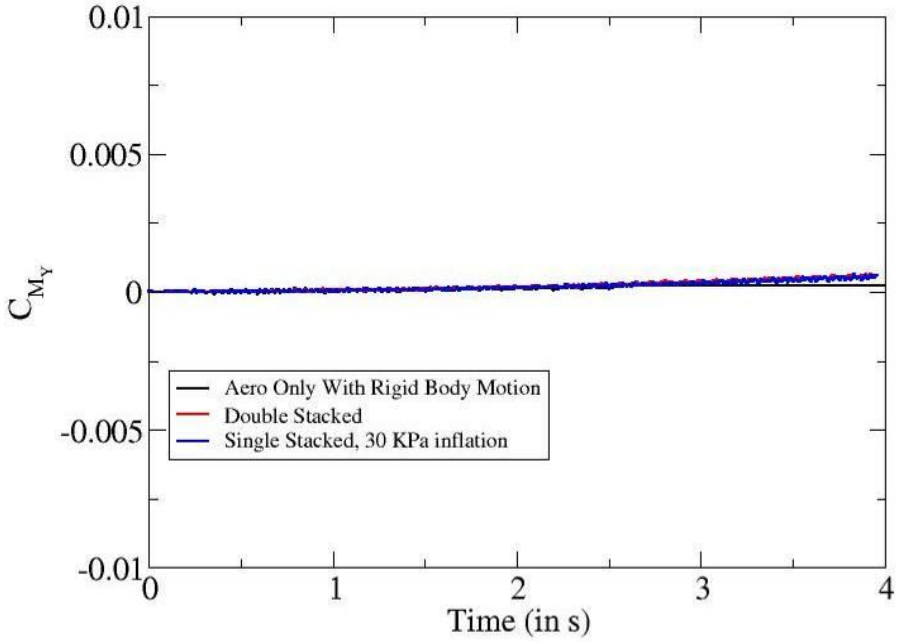

Figure 104. History of side moment coefficient in the y-direction during the aeroelastic dynamic simulation for single and double stack configurations

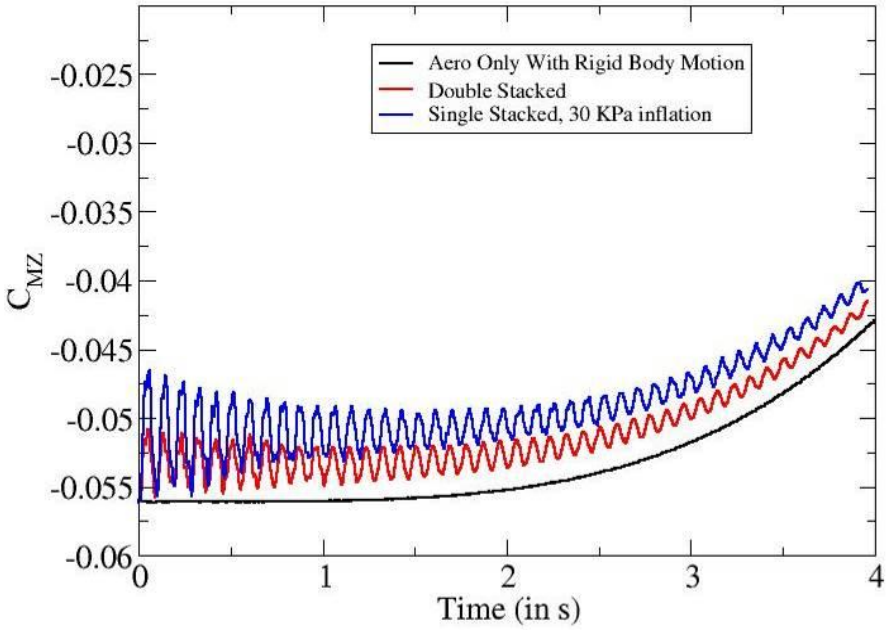

Figure 105. History of banking moment coefficient during the aeroelastic dynamic simulation for single and double stack configurations

7.5.2 Aeroelastic Structural Deformations

The history of displacement in the y-direction (direction of flow) at a point on the outer edge of the IAD for the single and double stack configurations are shown in Figure 106. The displacement in x-direction and z-direction are shown in Figure 107 and Figure 108, respectively. The contribution of the aeroelastic deformation alone for the x-component and the z-component are shown in Figure 109 and Figure 110, respectively.

The results show that there is a small increase in oscillation of the x, y, and z component of displacement about their mean for the single stack configurations. There is also reduction in amplitude as time passes due to the aerodynamic damping. The results also indicate that there are additional modes in the solution for the single stack configuration, especially when considering two-way FSI coupling.

As seen before in the test with constant CFD-averaged loads, the aeroelastic deformation alone for the z-component in Figure 110 shows increasing amplitude of oscillations as the solution progresses. However, due to the effect of aerodynamic damping, the amplitude of oscillations is smaller compared to the results from the constant averaged CFD loads.

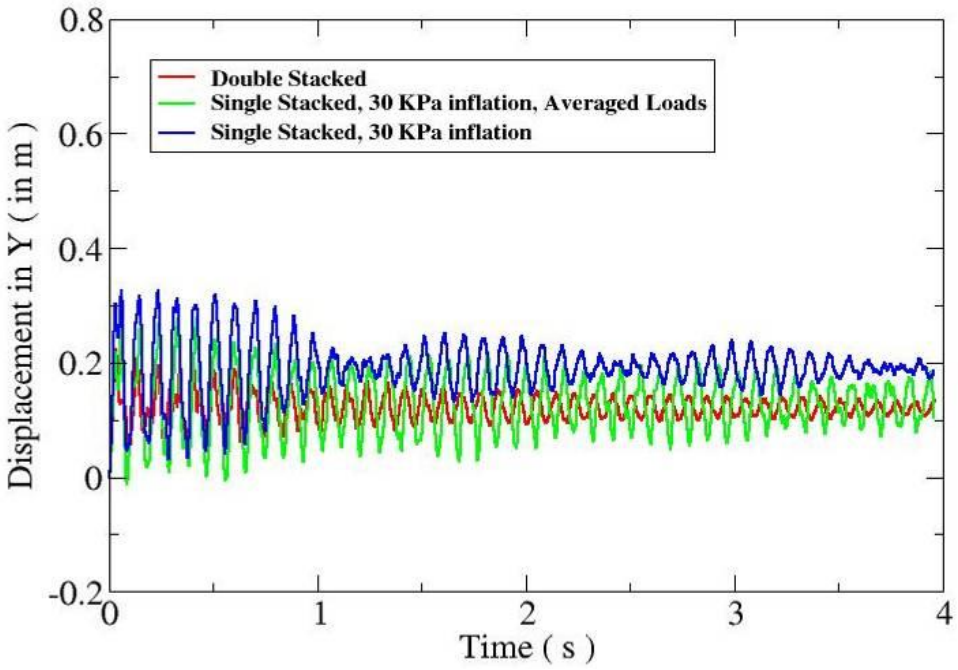

Figure 106 Comparison of y-component of structural deformation for single and double stack configurations.

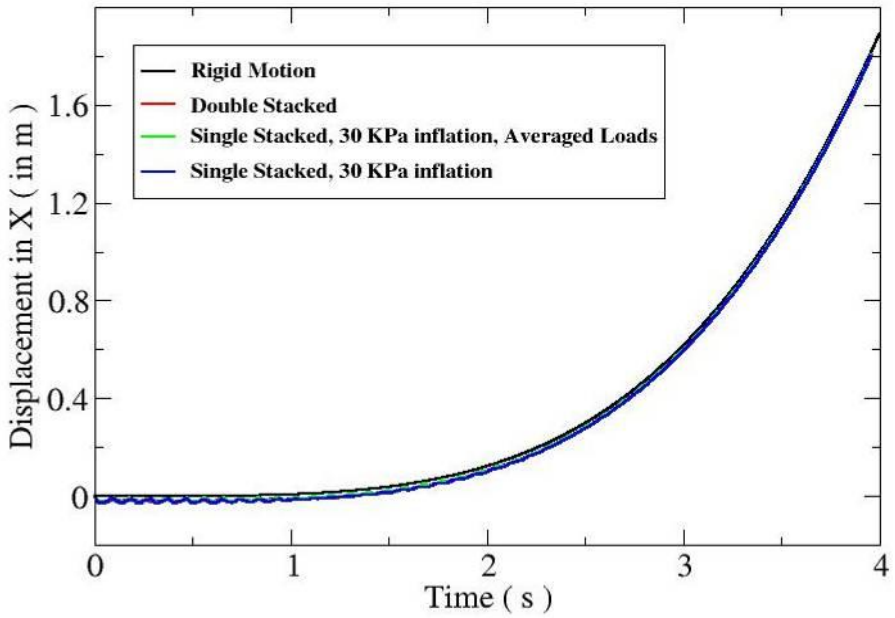

Figure 107 Comparison of x-component of structural deformation for single and double stack configurations.

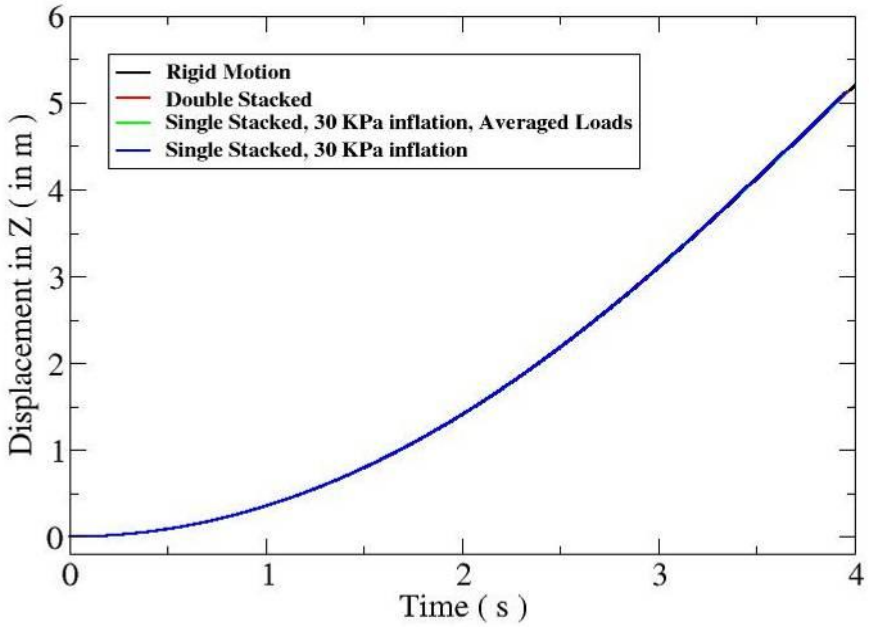

Figure 108 Comparison of z-component of structural deformation for single and double stack configurations.

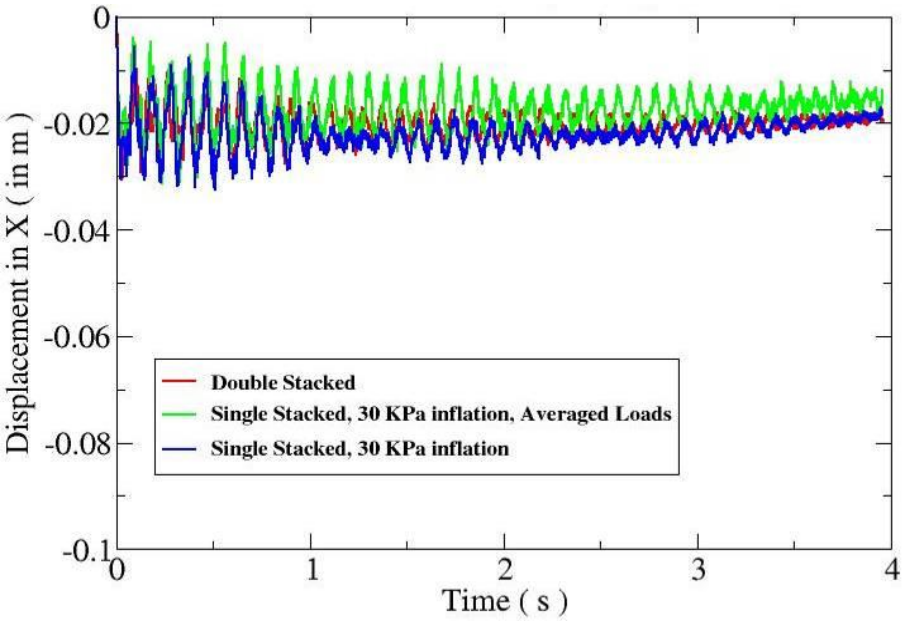

Figure 109 Comparison of aeroelastic component of structural deformation in the x-direction for single and double stack configurations.

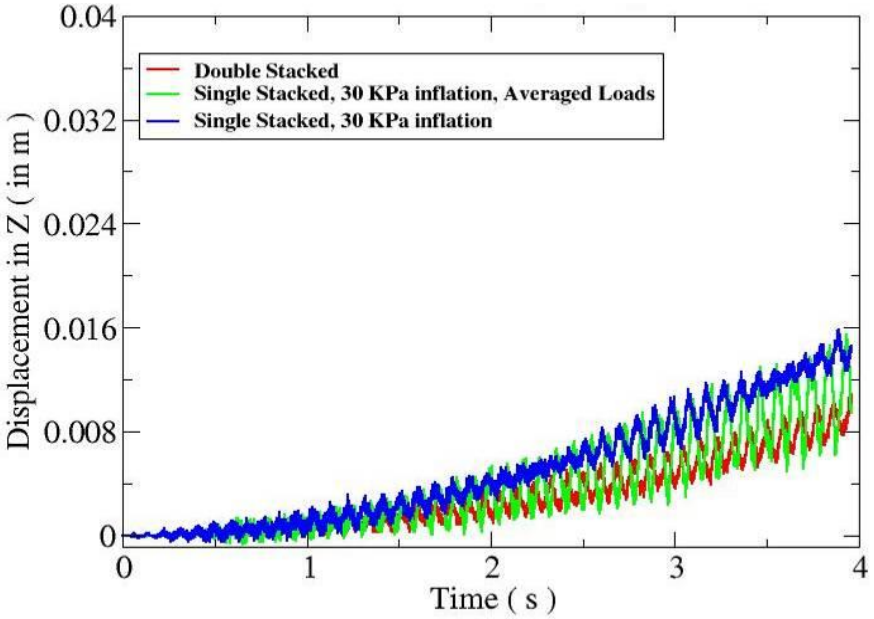

Figure 110 Comparison of aeroelastic component of structural deformation in the z-direction for single and double stack configurations.

Fast Fourier Transforms (FFT) of aeroelastic component of the x-displacement and the y-displacement were performed. The plots of the power spectral density (PSD) of all the cases considered in this subtask are shown in Figure 111 and Figure 112.

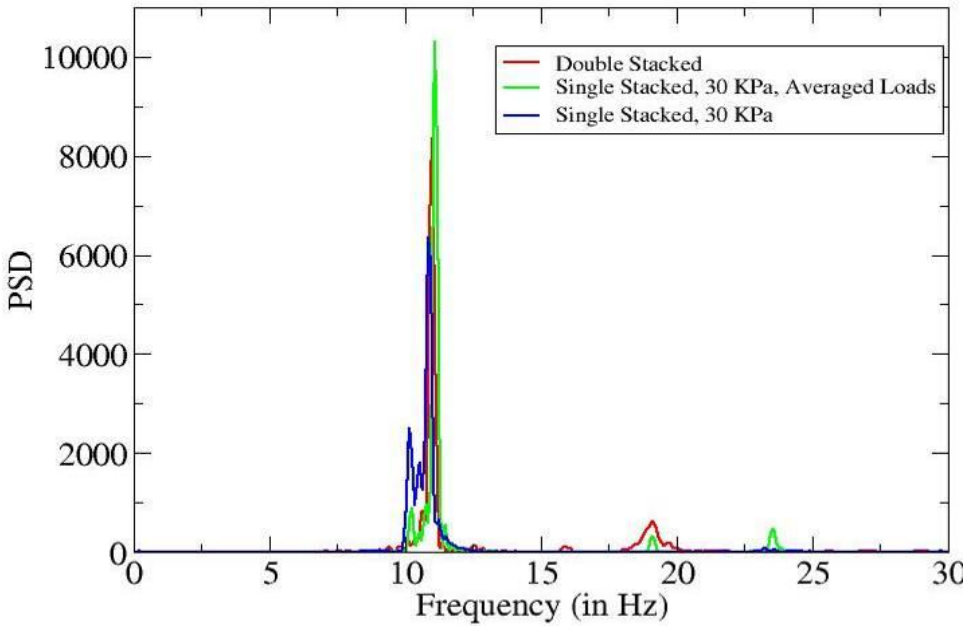

Figure 111 Comparison of PSD based on y-component of structural deformation for single and double stack configurations.

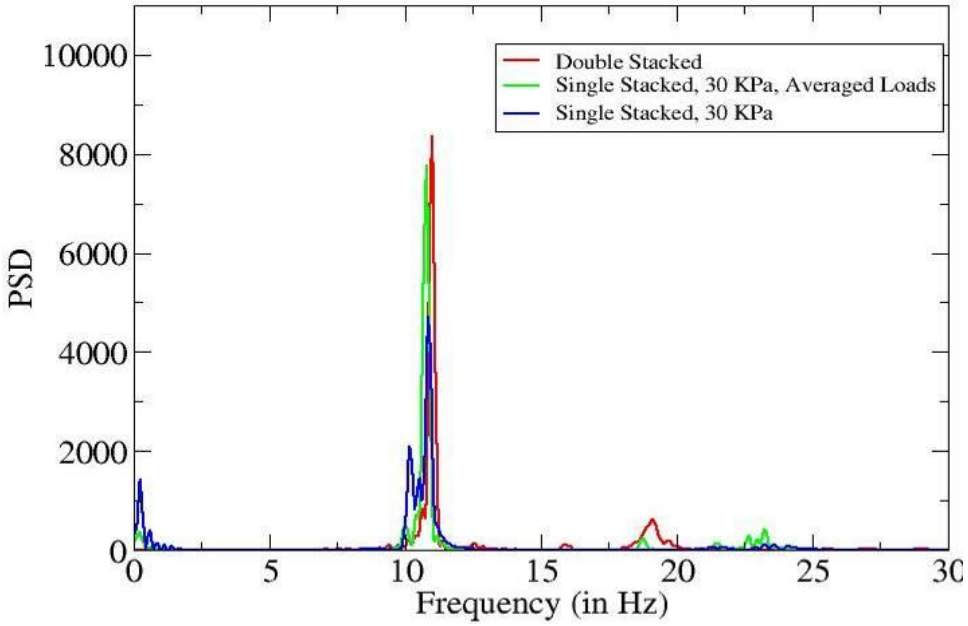

Figure 112 Comparison of PSD based on aeroelastic component of structural deformation in the x-direction for single and double stack configurations.

7.5.3 Aeroelastic Structural von Mises Stresses

In this section, von Mises stress results for the single stack configuration obtained using the two-way coupling are presented and are compared with the double stack model results and the results obtained using the constant averaged CFD loads. The time history of von Mises stress results on the toroids is presented in Figure 113. The figure also shows that the von Mises stress is cyclic, similar to the structural deformations. The stress in the single stack model is fluctuating between a maximum value of 3 E+08 N/m^2 and a minimum value of 2 E+08 N/m^2. Since the yield stress of the Kevlar material is 35 GPa, the stress levels are way below the yield stress of the material.

The time history of von Mises stress results on the cover (skin/gore) is presented in Figure 114. The von Mises stress on the skin is also cyclic, and is fluctuating between a maximum value of 1.5 E+08 N/m^2 and a minimum value of 5E+07 N/m^2. Snapshots of peak von Mises stresses on the front surface of the IAD are shown in Figure 115. The peak stress levels occur at the windward side of the front surface of the toroids. For the cover, the peak values of stresses occur around the inner circle of the model near the location of the adapter.

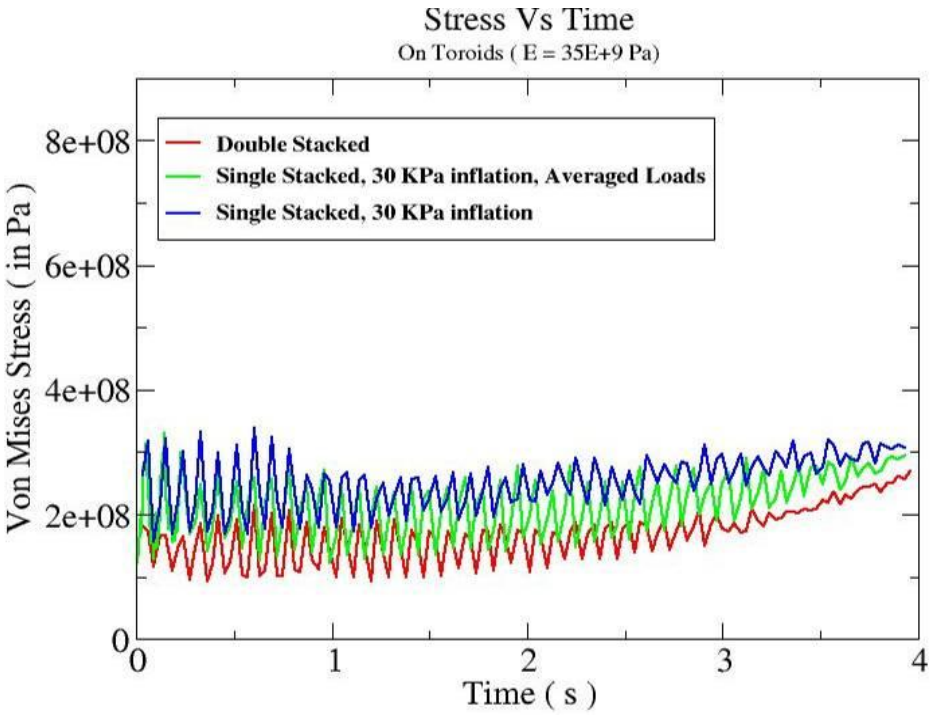

Figure 113 Comparison of von Mises stresses on the toroids for single and double stack configurations.

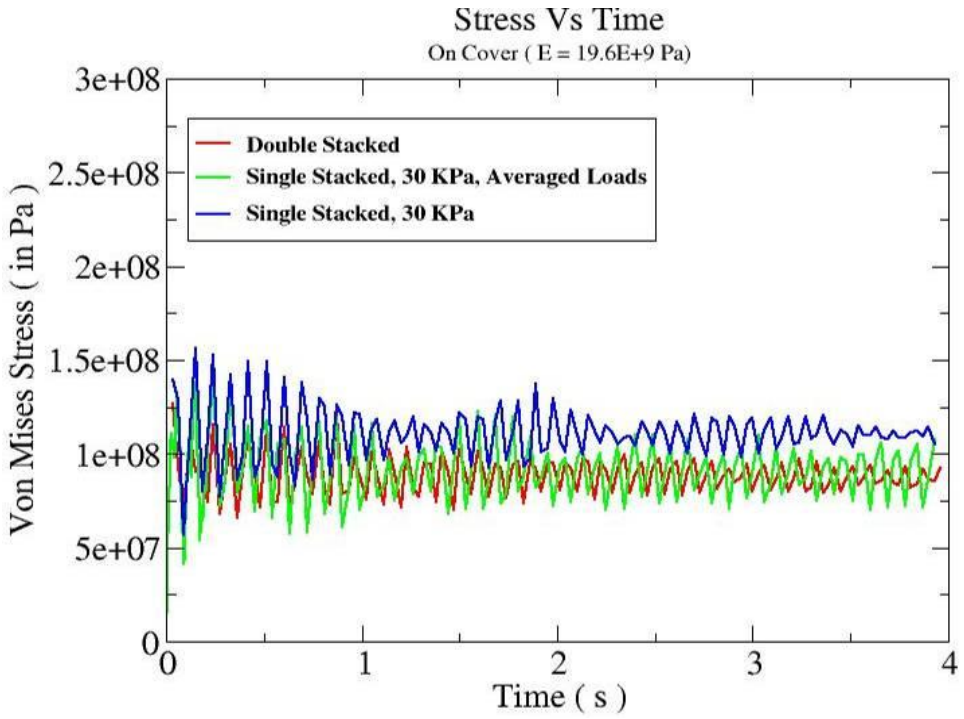

Figure 114 Comparison of von Mises stresses on the cover (gores/skin) for single and double stack configurations.

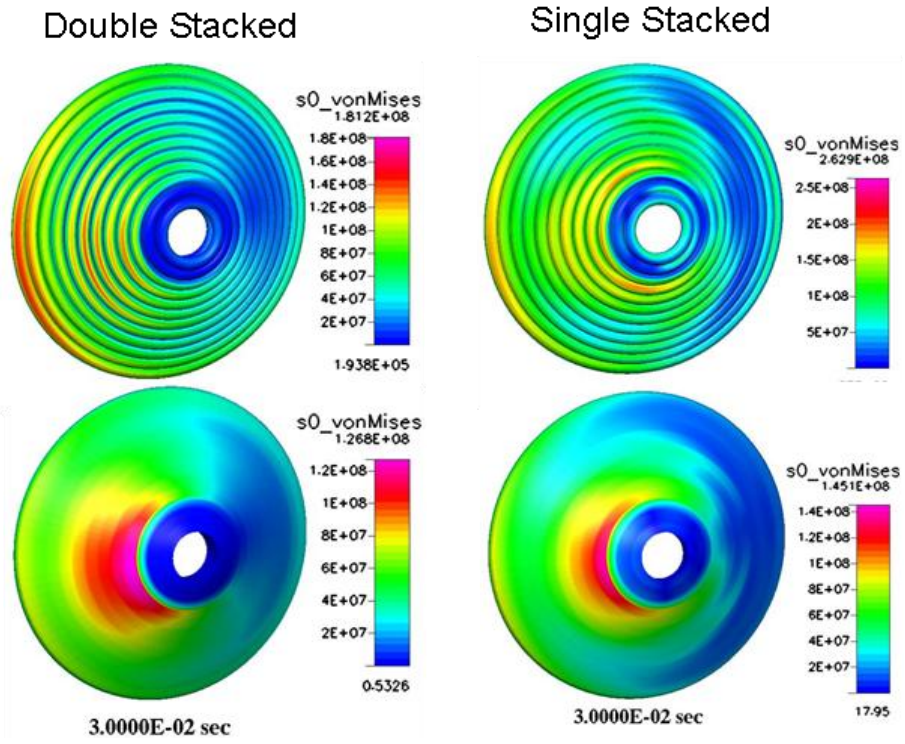

Figure 115 Snapshots of peak von Mises stresses on the toroids and cover (gores/skin) for single and double stack configurations.

7.6 Summary

A new configuration was modeled using a single stack of toroids instead of the double stack used in previous tasks. Additional changes in skin thickness and properties were incorporated into the new model. Steady state CFD tests were run to provide new load models. The aeroelastic response was then computed for two different internal pressures using constant averaged loads and two-way FSI coupling and compared with previous models. It was seen that the aerodynamic response of the single stack configuration was very similar to the double stack configuration. There were small increases in the displacements and in the von Mises stresses. The von Mises stresses are still far less than the yield stress of the Gores and toroids materials.

8 EFFECT OF DYNAMIC PRESSURE ON THE AEROELASTIC RESPONSE OF A SINGLE STACK IAD CONFIGURATION

In this effort, CFDRC studied the effect of flow dynamic pressure on the aeroelastic response of the IAD. These tests will help to give NASA engineers a degree of confidence in the factor of safety assumptions in the model. The single stack model developed previously was used to conduct aero-structural and dynamic simulations of the IAD model at 30 degrees angle of attack and bank angle rate of 5 deg/sec^2. Simulations were carried out for up to 4 seconds. An effort was also made to understand the effect of aero loads on buckling of the IAD and of a single toroid. The following aero-structural simulations were conducted in this effort:

1. ***Effect of dynamic pressure on the response of the IAD the using two-way FSI coupling***. In this case, the dynamic response of single stack model at the reference dynamic pressure (Q_{ref} = 5143 Pa) was compared with the response for half the dynamic pressure and for 1.5 times the reference dynamic pressure for the same banking maneuver.
2. ***Effect of dynamic pressure and loads on the buckling tendency of the IAD***. In this case, the average CFD loads on several patches of the model equivalent to 1.5, 2, 3 and 4 times the reference dynamic pressure (Q_{ref} = 5143 Pa) are applied to the FEM model and the structural responses are computed during the dynamic maneuver. A set of cases was also run to find the response of a single toroid to buckling loads.

8.1 Steady State CFD Results for Various Dynamic Pressures

The previously developed aerodynamic models with the flow and flight conditions for the simulation given in Table 3 was used to simulate the aerodynamic flowfields around the new single stack IAD model at two different dynamic pressures. In order to change the dynamic pressure, the density of the flow was changed, in turn changing the static pressure. For the 0.5 times reference dynamic pressure ($0.5*Q_{ref}$) case, the pressure used was 18.85 Pa and for the 1.5 * Q_{ref} case, the pressure used was 56.57 Pa.

The surface pressure contours over the front of the IAD surface for the various dynamic pressures are shown in Figure 116. At the reference dynamic pressure case, the maximum pressure of about 8500 Pa occurs over the front shield of the model and in front of the oncoming flow. This peak value is only about 4200 Pa for the $0.5*Q_{ref}$ case and is 12,700 Pa for the 1.5 * Q_{ref} case.

The maximum pressure occurs nears the windward side of the model and decreases toward the leeward side. The pressure profiles on the front surface for the various dynamic pressures are shown in Figure 117 The pressure differences in the back of the model is very small compared to the front side. The plot of coefficient of pressure shows that the profiles are near identical to each other as seen in Figure 118.

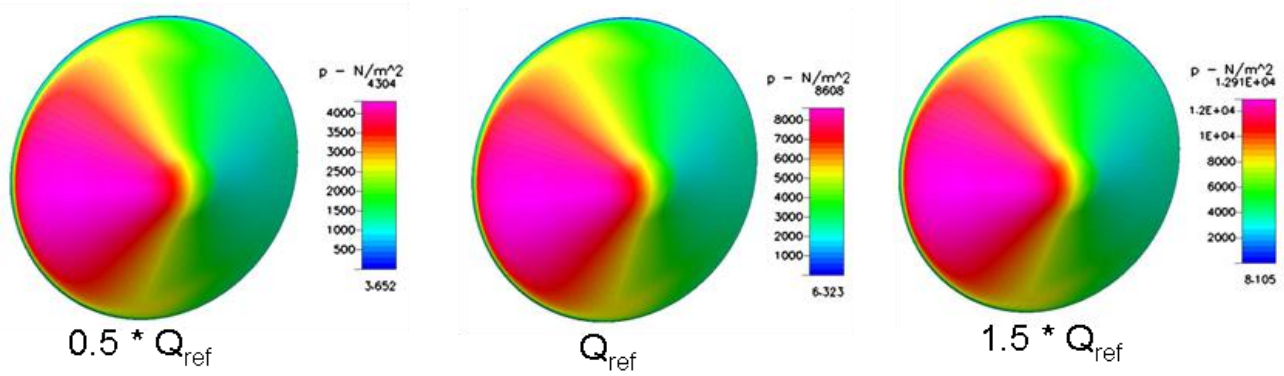

Figure 116 Pressure contours on the front surface of the single stack IAD model

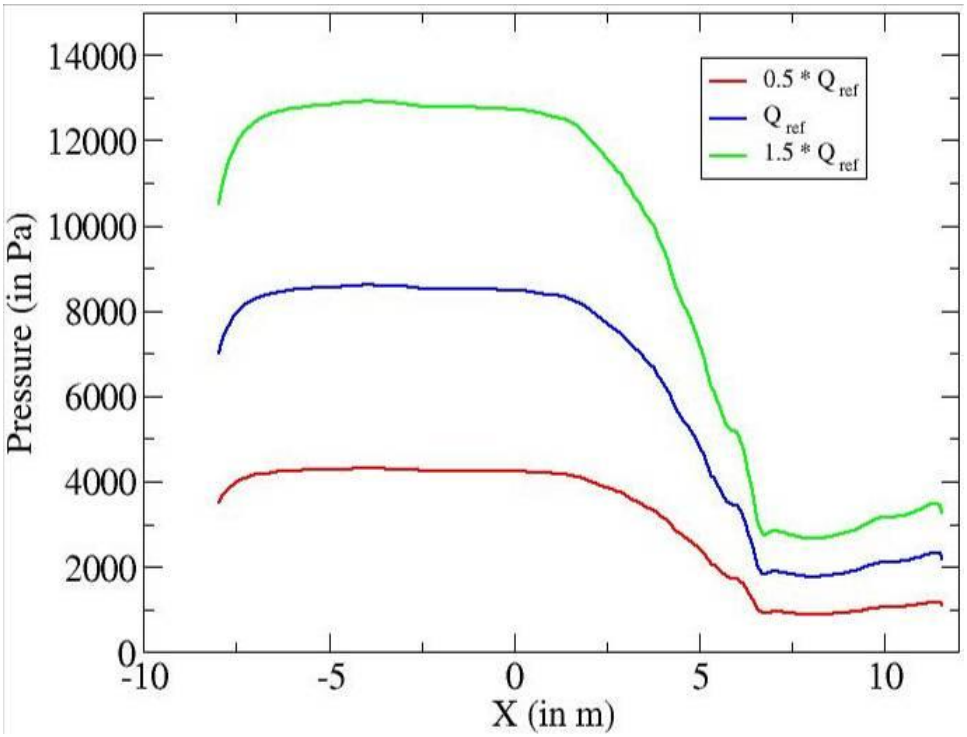

Figure 117 Comparison of pressure profiles on the front of the single model for various dynamic pressures

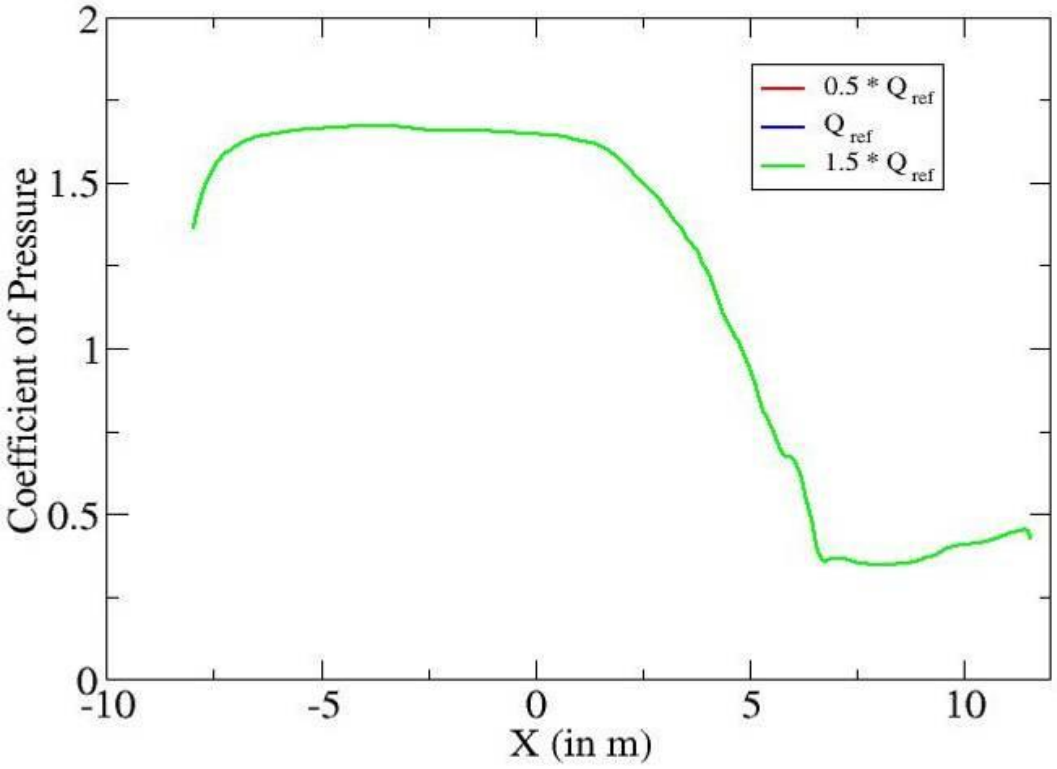

Figure 118 Comparison of coefficient of pressure on the front of the single model for various dynamic pressures

8.2 Transient Two-Way FSI Simulation of the Single Stack IAD Dynamics

In this subtask, the single stack IAD model was run with a design inflation pressure of 30 KPa using two way FSI coupling for two different flow dynamic pressures ($0.5*Q_{ref}$ and $1.5*Q_{ref}$). All simulations were started from an undeformed initial state. The simulations with two-way FSI coupling were conducted for 4 seconds of simulation. The results were compared to the single stack model at the reference dynamic pressure and with the results from the rigid body motion.

8.2.1 Aerodynamic Forces and Moments

The histories of the aerodynamic forces and moments during the aeroelastic dynamic simulation are shown in Figure 119 - Figure 124. The results of the two-way coupling methods using the single stack configuration with the two different dynamic pressures is compared with the results obtained using the reference dynamic pressure and also with the aerodynamic coefficients of aerodynamic simulation with rigid motion for reference. The histories of the lift and drag coefficients during the aeroelastic dynamic simulation are shown in Figure 119 and Figure 120, respectively. The history of the side force coefficient is shown in Figure 121. The histories of the side moment coefficients and banking moment coefficients are shown in Figure 122, Figure 123 and Figure 124.

All the results show damping of the oscillations as the simulation progresses, due to aerodynamic damping, indicating the structure is aeroelastically stable. Multiple modes can be seen for the higher dynamic pressures. Also, at higher dynamic pressures, both the variation and mean value of the aerodynamic coefficients is larger.

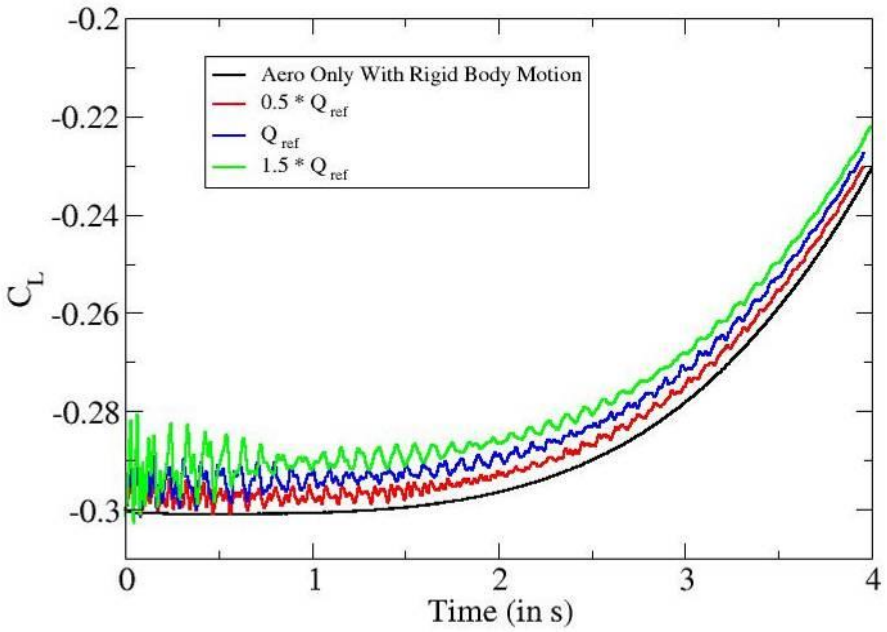

Figure 119. History of coefficient of lift during the aeroelastic dynamic simulation for various dynamic pressures

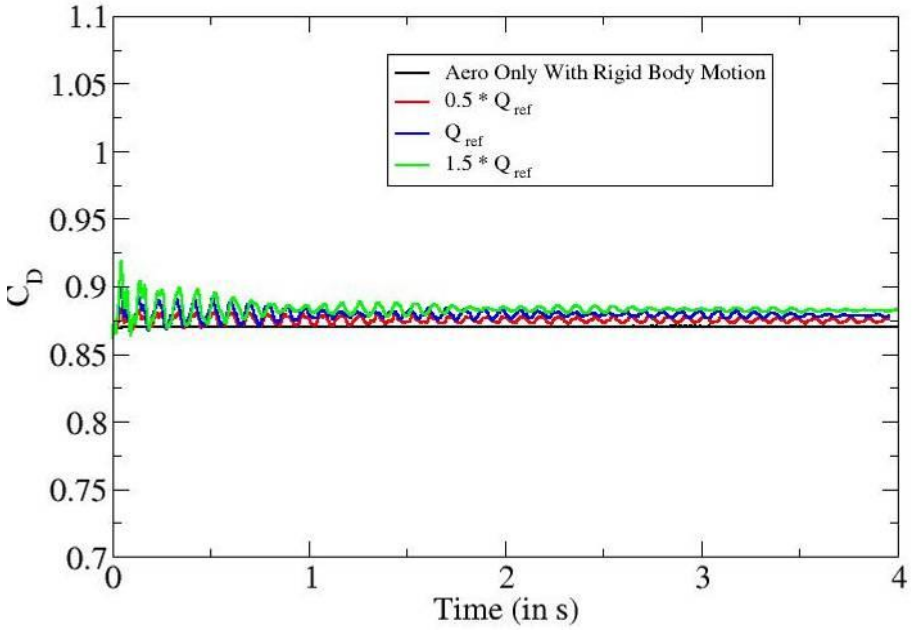

Figure 120. History of coefficient of drag during the aeroelastic dynamic simulation for various dynamic pressures

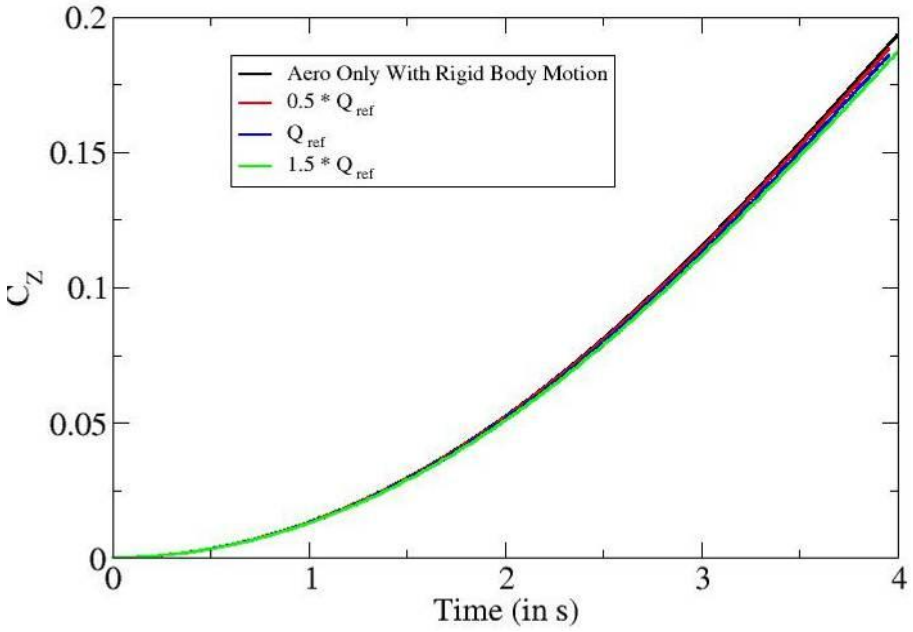

Figure 121. History of side force coefficient during the aeroelastic dynamic simulation for various dynamic pressures

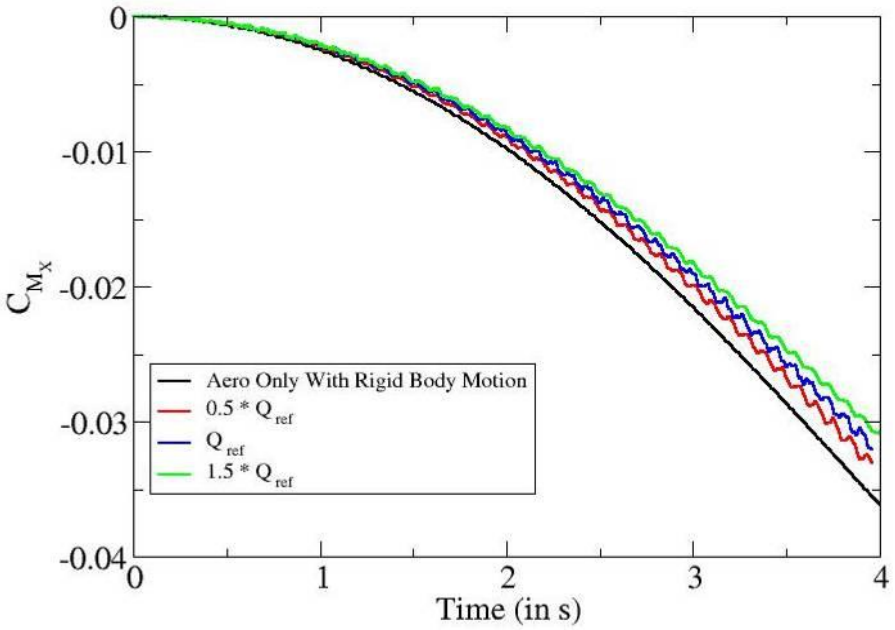

Figure 122. History of side moment coefficient in the x-direction during the aeroelastic dynamic simulation for various dynamic pressures

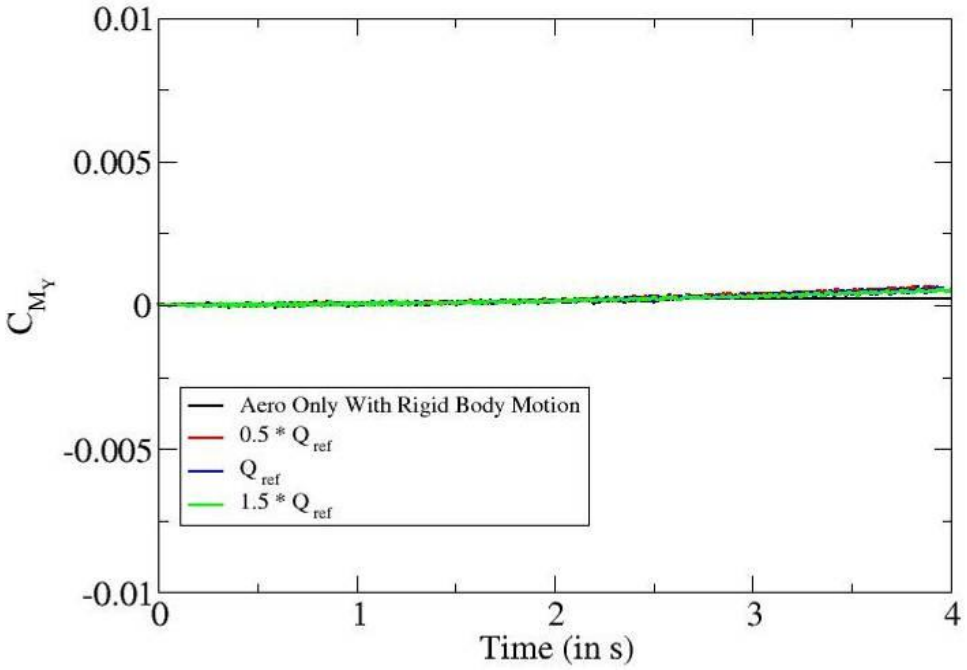

Figure 123. History of side moment coefficient in the y-direction during the aeroelastic dynamic simulation for various dynamic pressures

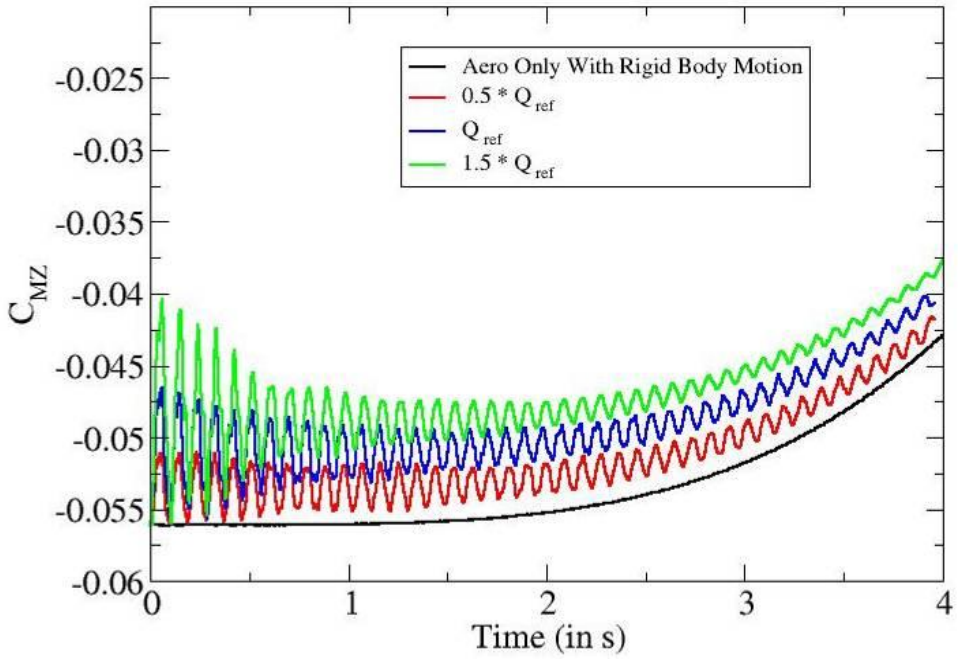

Figure 124. History of banking moment coefficient during the aeroelastic dynamic simulation for various dynamic pressures

8.2.2 Aeroelastic Structural Deformations

The history of displacement in the y-direction (direction of flow) at a point on the outer edge of the IAD for the single stack configurations for various flow dynamic pressures are shown in Figure 125. The displacement in x-direction and z-direction are shown in Figure 126 and Figure 127 respectively. The contribution of the aeroelastic deformation alone for the x-component and the z-component are shown in Figure 128 and Figure 129 respectively.

The results show that there is a large increase in oscillation of the x, y, and z component of displacement about their mean for the single stack configurations as the dynamic pressure is increased. There is also a reduction in amplitude as time passes due to the aerodynamic damping. The results also indicate that there are additional modes in the solution for the higher dynamic pressures.

As seen before in the test with constant CFD-averaged loads, the aeroelastic deformation alone for the z-component in Figure 129 shows increasing amplitude of oscillations as the solution progresses.

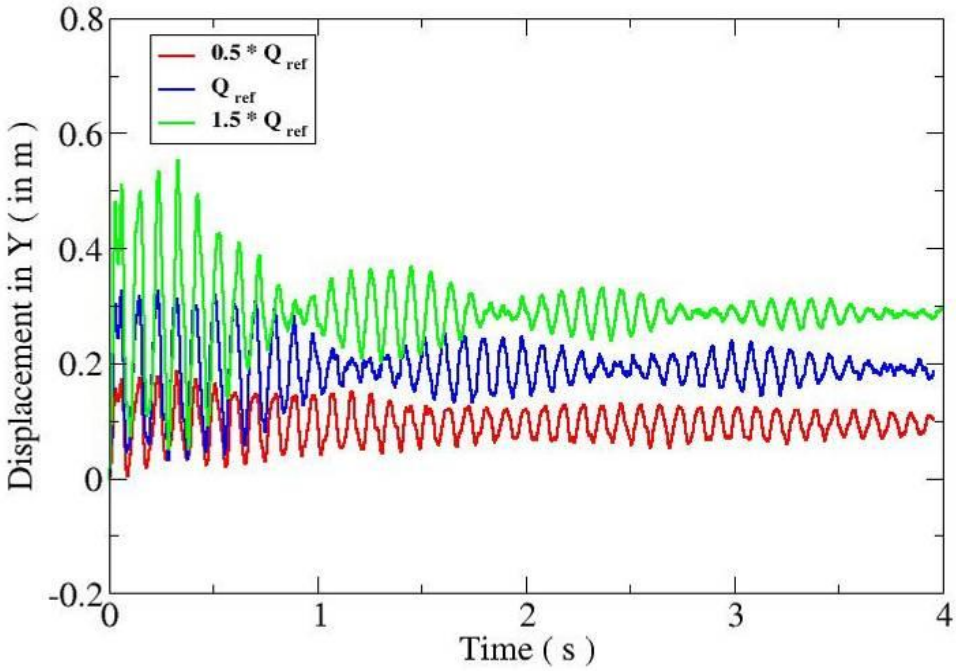

Figure 125 Comparison of y-component of structural deformation for various dynamic pressures.

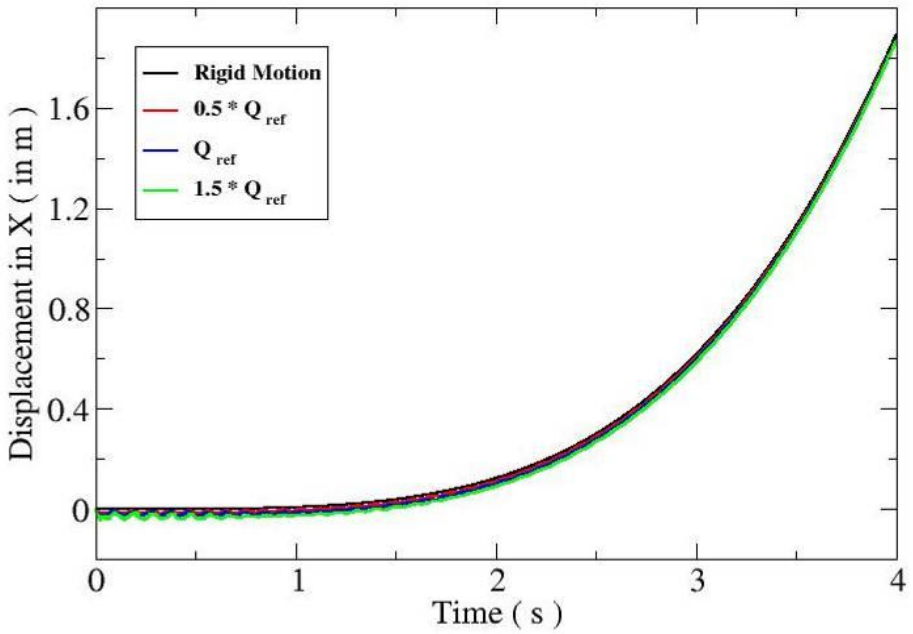

Figure 126 Comparison of x-component of structural deformation for various dynamic pressures.

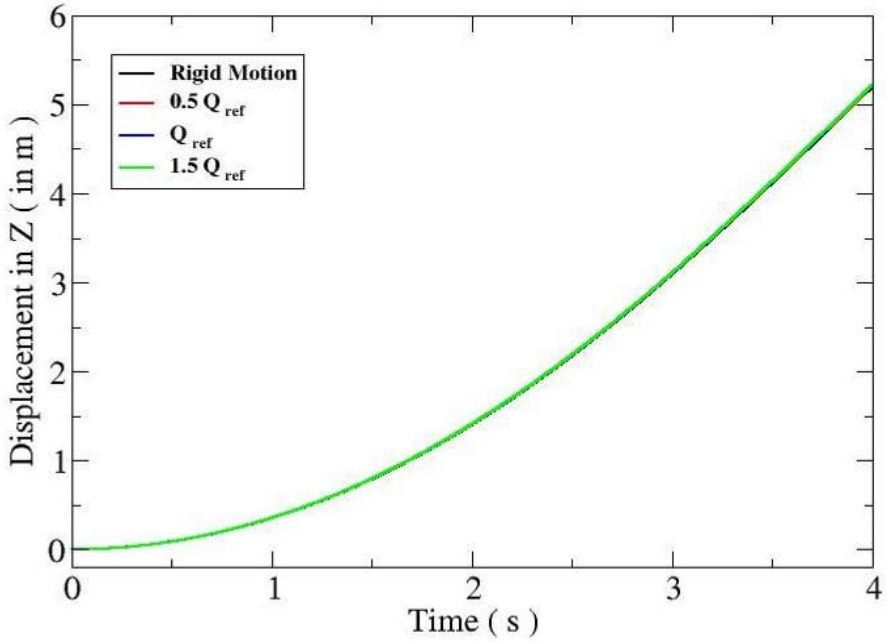

Figure 127 Comparison of z-component of structural deformation for various dynamic pressures.

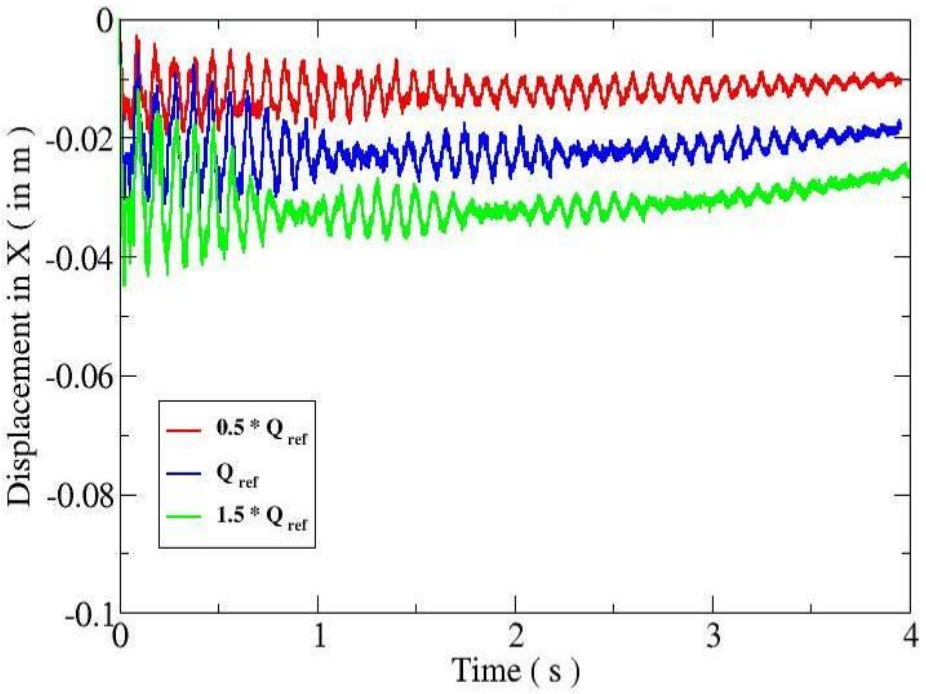

Figure 128 Comparison of aeroelastic component of structural deformation in the x-direction for various dynamic pressures.

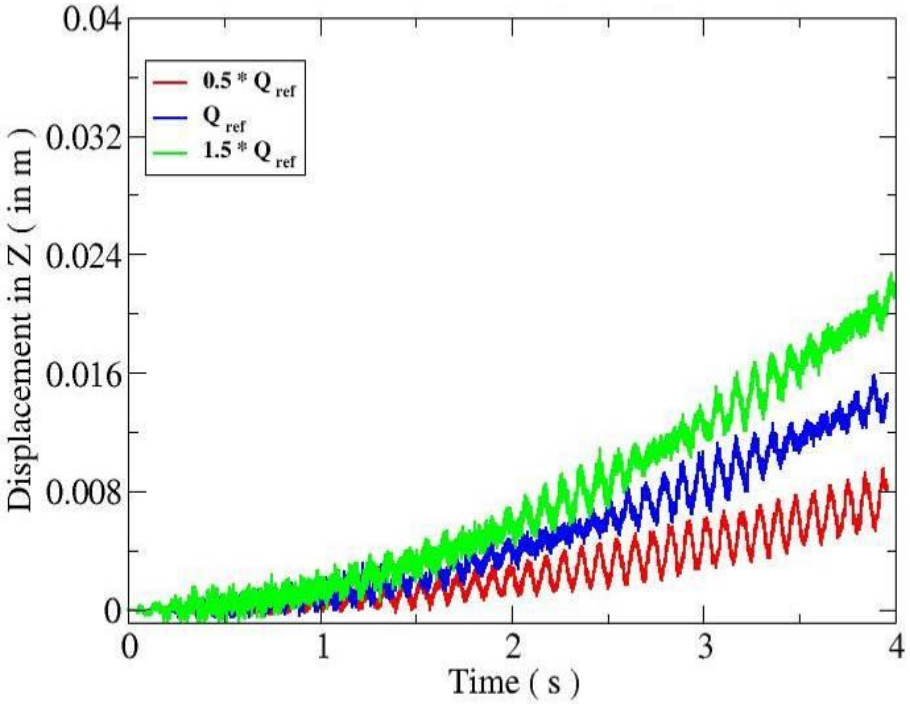

Figure 129 Comparison of aeroelastic component of structural deformation in the z-direction for various dynamic pressures.

Fast Fourier Transforms (FFT) of aeroelastic component of the x-displacement and the y-displacement were performed. The plots of the power spectral density (PSD) of all the cases considered in this subtask are shown in Figure 130 and Figure 131. The plots show a larger number of modes as the dynamic pressure is increased.

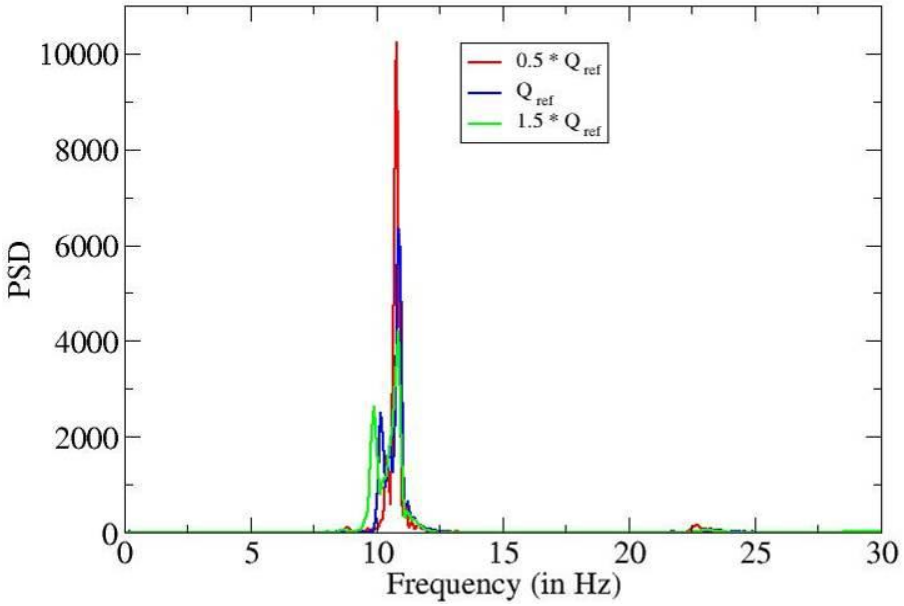

Figure 130 Comparison of PSD based on y-component of structural deformation for various dynamic pressures.

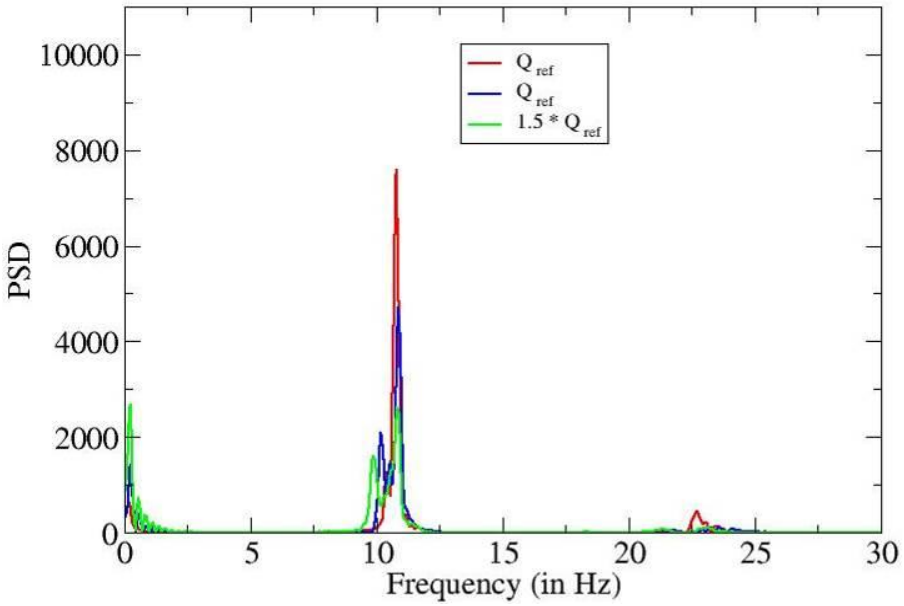

Figure 131 Comparison of PSD based on aeroelastic component of structural deformation in the x-direction for various dynamic pressures.

8.2.3 Aeroelastic Structural von Mises Stresses

In this section, von Mises stress results for the single stack configuration obtained using the two-way coupling for various flow dynamic pressures are presented. The time history of von Mises stress results on the toroids is presented in Figure 132. The figure also shows that the von Mises stress is cyclic, similar to the structural deformations. The stress in the single stack model for the $1.5*Q_{ref}$ case is fluctuating between a maximum value of 5.7 E+08 N/m^2 and a minimum value of 2 E+08 N/m^2. Since the yield stress of the Kevlar material is 35 GPa, the stress levels are way below the yield stress of the material.

The time history of von Mises stress results on the cover (skin/gore) is presented in Figure 133. The von Mises stress on the skin is also cyclic, and is fluctuating between a maximum value of 2.5 E+08 N/m^2 and a minimum value of 1E+08 N/m^2 for the $1.5*Q_{ref}$ case.

Snapshots of peak von Mises stresses on the front surface of the IAD are shown in Figure 134. The peak stress levels occur at the windward side of the front surface of the toroids. For the cover, the peak values of stresses occur around the inner circle of the model near the location of the adapter.

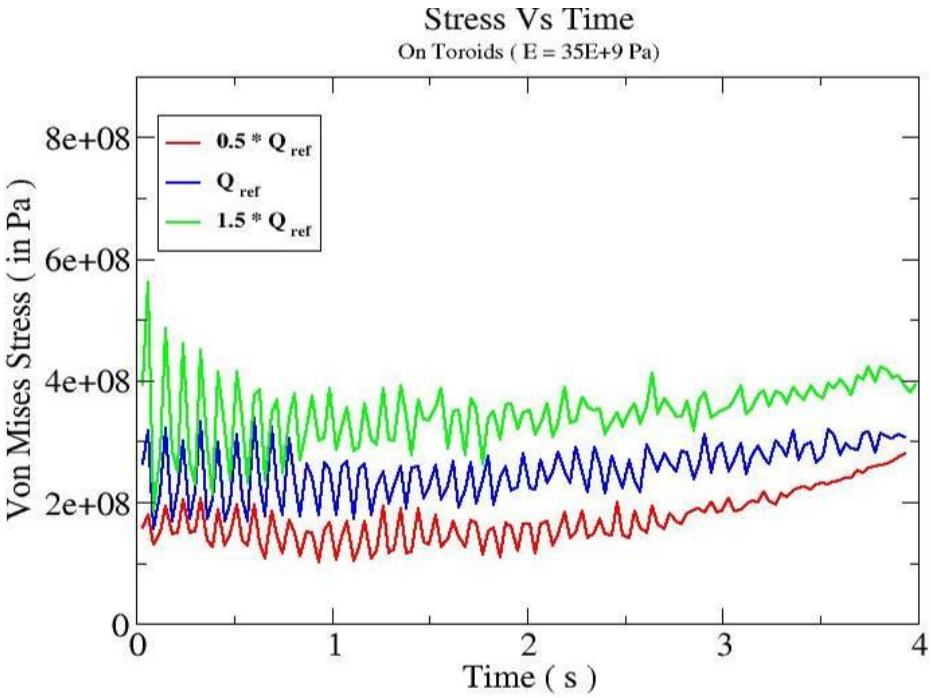

Figure 132 Comparison of von Mises stresses on the toroids for various dynamic pressures.

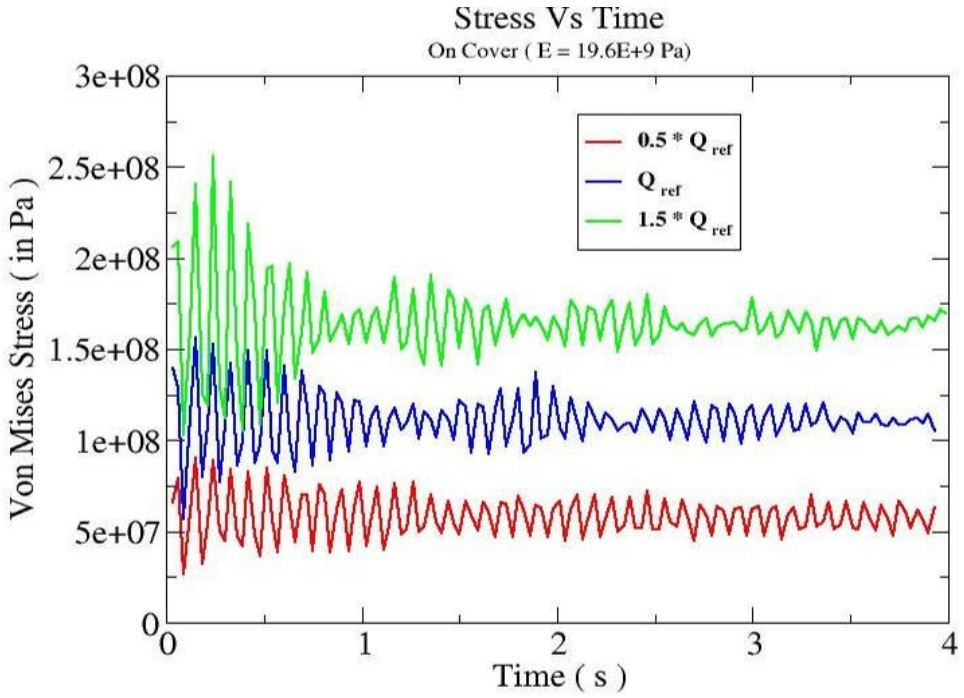

Figure 133 Comparison of von Mises stresses on the cover (gores/skin) for various dynamic pressures.

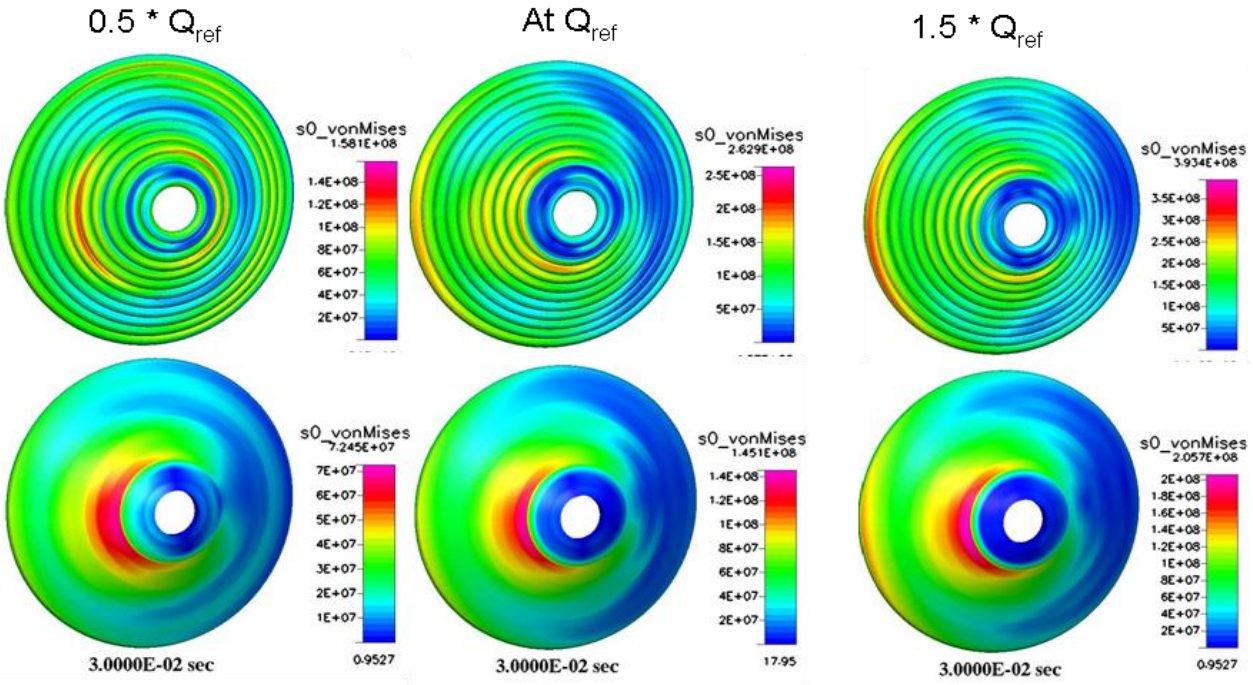

Figure 134 Snapshots of peak von Mises stresses on the toroids and cover (gores/skin) for various dynamic pressures.

8.3 Modeling Failure and Collapse of a Single Stack IAD

In this subtask, the loads required to induce the failure and collapse of a single stack IAD configuration are simulated. The single stack IAD model was run with a design inflation pressure of 30 KPa using average constant CFD loading. Multiple cases were run using various pressure loads equivalent to multiples of the reference flow dynamic pressure and were compared with each other. All simulations were started from an undeformed initial state. The dynamic simulations were conducted for about 0.4 seconds of simulation. Contact between the cover and skin was not modeled for this set of simulations.

The trace of displacements in the y-direction at a point at the edge of the IAD is shown in Figure 135. The results show that the single stack IAD begins to show signs of collapse for pressure loads equivalent to around three times the reference dynamic pressure.

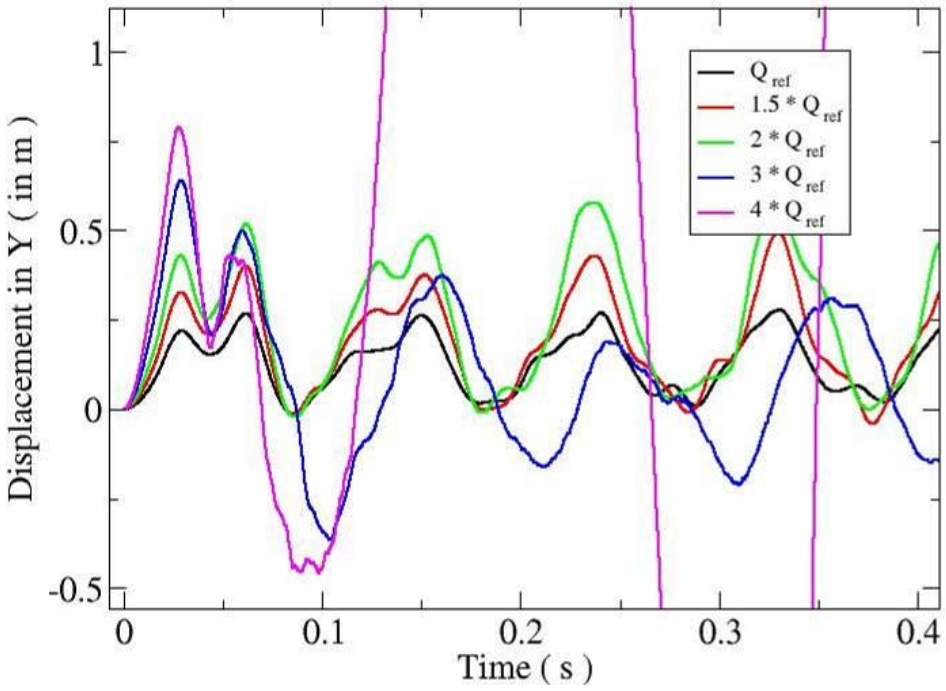

Figure 135 Comparison of y-component of structural deformation for single stack configurations with various pressure loads.

The deformation of the skin at four times the reference dynamic pressure is shown in Figure 136 (a). The large deformation and wrinkling of the skin can be seen clearly. The z-cut of the IAD model shown in Figure 136 (b) shows a large movement of the cover and shows penetration of the toroids, which is clearly unphysical. This is due to the fact that contact was not modeled. The very large stresses developed in the model which are of the order of the yield strength of the materials are shown in Figure 137.

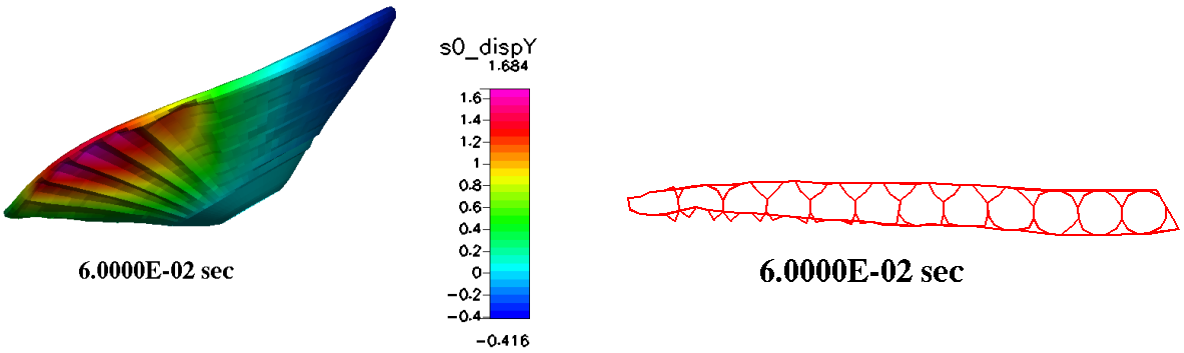

(a) Deformation contours in the y-direction (b) Z-cut of the windward side of IAD model

Figure 136 Contour plots and z-cut of IAD at 60 ms for a pressure load at four times the reference dynamic pressure.

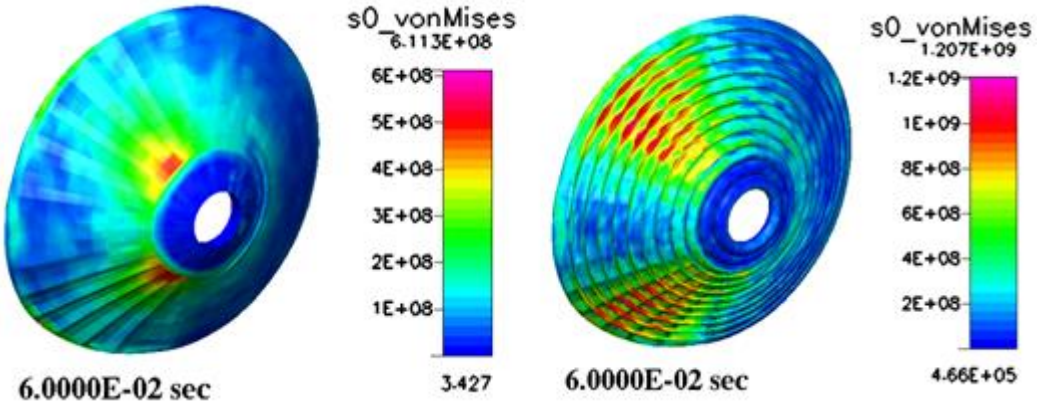

Figure 137 Contour plot of von Mises stress at 60 ms on the cover and toroids for a pressure load at four times the reference dynamic pressure.

Obviously, the penetration between the skin and toroids are not physical due to the absence of the contact model in the previous FEM model. Addition of the contact model would enable the FEM model to predict more accurate response of the structural model. The disadvantage in contact modeling is the large amounts of simulation time required. It was seen that in order to model contact between the cover and toroids, the simulation time increased by a factor of 5. To model the self contact between toroids, the simulation time increase by a factor of 20.

In the next test, contact between the toroid and cover was modeled for the case with four times the reference dynamic pressure. The trace of displacements in the y-direction at a point at the edge of the IAD is shown in Figure 138. The results show that the single stack IAD with contact models at four times the reference dynamic pressure still shows large deformations and buckling compared to the reference dynamic pressure case as seen in Figure 139 but that they are much smaller than without the contact model. The stresses developed in the model are shown in Figure

140. Animations of the structural responses and buckling of the model were created and submitted to NASA engineers to give insight about the dynamic response of the model.

The disadvantage in contact modeling is the large amounts of simulation time required. It was seen that in order to model contact between the cover and toroids, the simulation time increased by a factor of 5. To model the self contact between toroids, the simulation time increase by a factor of 20.

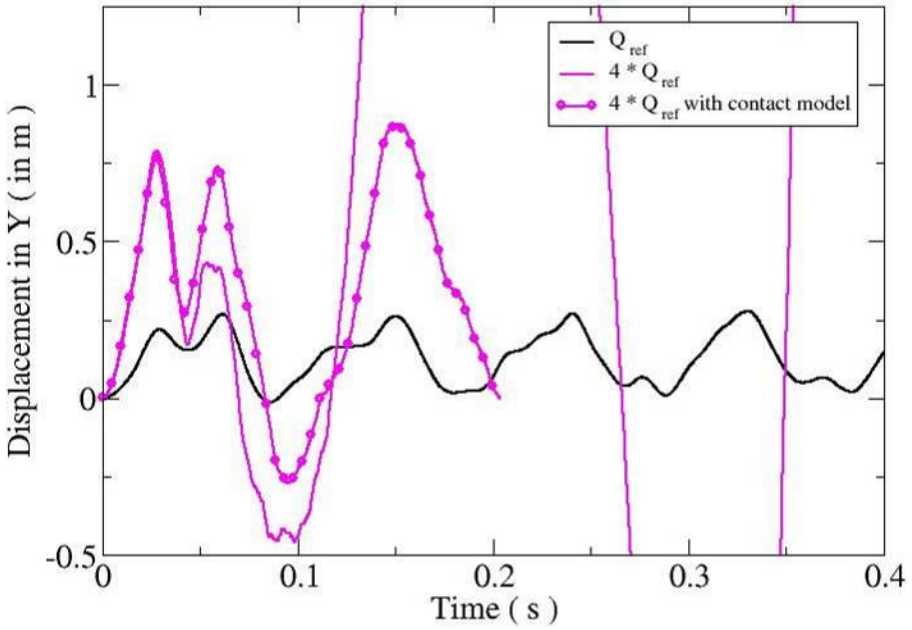

Figure 138 Comparison of y-component of structural deformation for single stack configurations with various pressure loads and with contact.

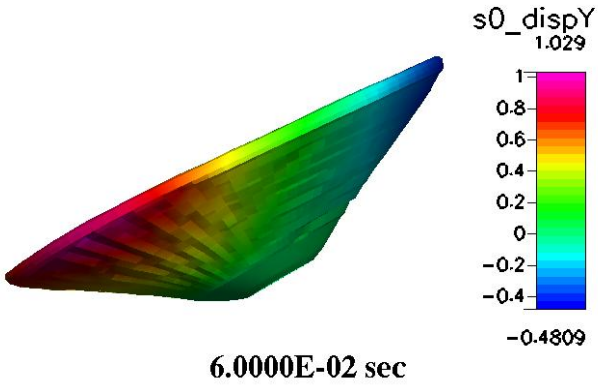

(a) Deformation contours in the y-direction

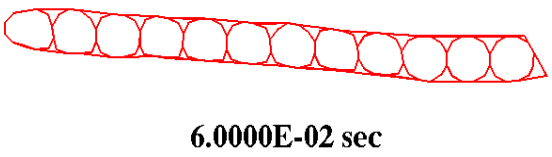

(b) Z-cut of the windward side of IAD model

Figure 139 Contour plots and z-cut of IAD at 60 ms for a pressure load at four times the reference dynamic pressure with contact model.

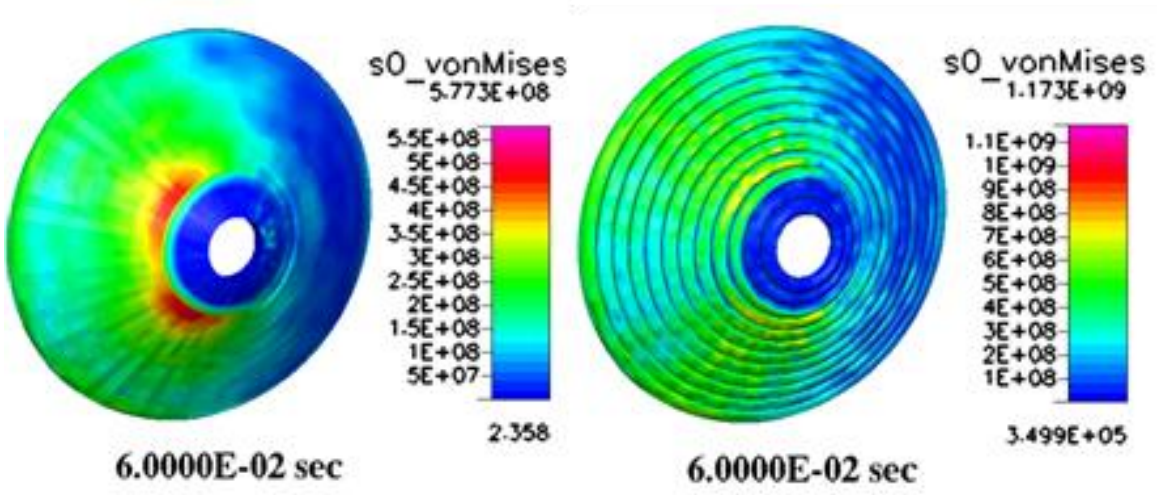

Figure 140 Contour plot of von Mises stress at 60 ms on the cover and toroids for a pressure load at four times the reference dynamic pressure with a contact model.

8.4 Summary

In order to test the limits of the single stack configuration, simulations were run at various multiples of the reference dynamic pressure. Two way FSI coupled simulations were run at 0.5 times the reference dynamic pressure and 1.5 times the reference dynamic pressure. The aeroelastic response was computed for an internal pressure of 30 KPa. The dynamic response showed an increased number of modes with an increase in flow dynamic pressure. The stresses were still within limits even for the case with 1.5 times the reference dynamic pressure. Further tests were conducted on a single stack configuration to find out the multiple of the flow dynamic pressure for which a collapse of the IAD occurred. It was seen that without contact modeling the numerical model showed signs of collapse for pressure loads equivalent to 3 times the reference dynamic pressure. Complete collapse was seen for four times the reference dynamic pressure. Once contact was modeled, collapse did not occur at that dynamic pressure, although large deformations and stresses were still seen. It was also observed that contact modeling has a large penalty associated with it in terms of computational time required.

9 SUMMARY AND CONCLUSIONS

Computational aeroelastic simulations were conducted for Inflatable Aerodynamic Decelerators (IAD) concepts to support the EDL-SA assessments of IAD controllability and structural integrity for Mars Aerocapture and EDL. Several design configurations, including double stack and single stack toroids, were considered to determine the candidate technology that meets the requirements. The following is a summary of the conclusions, lessons learned and recommendations for potential future work that would lead to better understanding of the behavior of these complex and unpredictable inflatable structures.

9.1 Summary and Concluding Remarks

A three-dimensional computational CFD model for the IAD model configuration was developed. A simplified non-reacting thermally perfect CO2 Mars atmosphere model was used since no chemical reactions occur at the Mach of 14.3 modeled. Steady state Euler simulation was conducted at 30 degrees angle of attack, and the aerodynamic forces and moments were predicted. In addition, a computational structural nonlinear FEM model of the IAD model was developed using quad shell elements. A modified version of the FEM model was also developed that takes into consideration the axial enforcement straps of the toroids. Extensive FEM simulations were conducted with various dynamic and internal pressures and using variable fidelity CFD calculated loads. The aeroelastic responses of the model were also computed for three simulations: 1) using averaged constant CFD predicted loading, 2) using one-way fluid-structure interaction (FSI) coupling from the fluid to the structure, and 3) using two-way FSI coupling. The structural responses of the three simulations were comparable. The structural deformations and stresses exhibited cyclic behavior over the model and they tended to fluctuate around almost constant mean values. The von Mises stress levels on the gores and toroids were far less than the yield stress of the respective materials.

The effect of increasing the toroids inflation pressure on the aeroelastic response of the IAD model was also investigated. The results showed that the inflation pressure has a small impact on overall deformation, remaining in line with the conducted static analysis. The effects of the radial straps were also taken into consideration by developing an equivalent mechanical model of the straps, which resulted in increasing the nominal thickness and material properties of the gores. Both CFD constant averaged loads and two-way FSI coupling were used. The results showed dramatic decrease of the aeroelastic deformations when the effects of radial straps are added to the model. von Mises stresses were still far less than the yield stress of the gores and toroids materials.

Another configuration was modeled using a single stack of toroids instead of the double stack configuration model. Additional changes in skin thickness and properties were incorporated into the model to account for the axial and radial straps. Steady state CFD tests were run to provide new load models. The aeroelastic response was then computed for two different internal pressures using constant averaged loads and two-way FSI coupling and compared with previous models. The aerodynamic flowfield and forces of the single stack configuration were very similar to the double stack configuration. There were small increases in the displacements and in

the von Mises stresses. The von Mises stresses were still far less than the yield stress of the gores and toroids materials.

In order to test the limits of the single stack configuration, simulations were run at various multiples of the reference dynamic pressure. Two-way FSI coupled simulations were run at 0.5 times the reference dynamic pressure and 1.5 times the reference dynamic pressure. The aeroelastic response was computed for an internal pressure of 30 KPa. The dynamic response showed an increased number of modes with an increase in flow dynamic pressure. The stresses were still within limits even for the case with 1.5 times the reference dynamic pressure. More tests were conducted on a single stack configuration to find out the multiple of the flow dynamic pressure for which a collapse of the IAD occurred. The analysis was initially conducted without the FEM contact model between the toroids and gores. The results showed signs of collapse for pressure loads equivalent to three times the reference dynamic pressure. Complete collapse was seen for four times the reference dynamic pressure. Once contact was modeled, collapse did not occur at that dynamic pressure, although large deformations and stresses were still seen. It was also observed that contact modeling has a large penalty associated with it in terms of computational time required.

9.2 Lessons Learnt

The following were the lessons learnt during this effort. They are broadly classified into three sections.

9.2.1 Flow Physics and Aeroelastic Coupling

1. A thermally perfect thermophysics model (Cp=Cp(T) curve fits) for pure CO2 captures the important shock physics effects of the Mars atmosphere at the Mach number considered.
2. The temperature dependent thermophysical properties correctly account for the increased temperature behind the shock and the resulting effective Gamma change. Chemically reacting flow effects are negligible at the Mach number considered.
3. No significant changes were seen in the pressure profiles between double and single stack IAD configurations.
4. The pressure profile over the fluid structure interface does not change significantly for any of the cases tested. Therefore, a carefully calculated asymmetric CFD averaged constant load is sufficient to simulate the CFD loading.

9.2.2 Structural FEM Solver

1. Nonlinear FEM modeling is necessary to correctly model the response of the very thin film materials.
2. Problems involving thin shell elements with large aspect ratios (>10000), coupled with the weak material properties are extremely hard to solve with implicit solvers due to the difficulty of inverting ill-conditioned matrices.

3. The usage of explicit solvers is cost-prohibitive due to the fact that the time step is driven by the small thickness. Therefore, we have used the mass scaling technique for shell elements involving explicit transient analysis. This scaling permits large critical time step size without loss of stability, which is particularly necessary for very thin shell structures.
4. If using solid shell FEM elements, two measures were to found to improve convergence and numerical stability: 1) dividing the CFD loads over the nodes top and bottom surfaces of an element, and 2) ramping the loads over multiple steps.

9.2.3 Structural IAD Model

1. Modeling the presence of radial and circumferential straps is important. The IAD is much stiffer and more stable due to the presence of these straps. Modeling these straps also improves numerical stability of the models.
2. Beyond a certain value, the internal pressure has a small effect on the peak displacement and the frequency of the IAD. If the internal pressure is too low compared to the external pressure, the structure will tend towards buckling.
3. The double stack and single stack configurations show remarkably similar frequencies. The single stack IAD shows slightly larger displacements.
4. It is important to model the contact between the skin and the toroids when low inflation pressures or large dynamic pressures are used. However, there is a significant computational penalty as a result.

9.3 Recommendations for Future Work

This Phase III effort has successfully performed all assigned tasks for the aero-structural assessment of different configurations of IADs. Our recommendations for future work in this area are presented next and can be divided into the following major areas.

9.3.1 Modeling Additional Flow Physics

1. Modeling turbulence and the full set of Navier-Stokes equations may prove to be important at lower altitudes.
2. The effect of local aerothermal heating on the structural properties and aeroelastic responses should also be modeled instead of simply using a global knockdown factor.
3. Effects of cone-angle variation of the model should be assessed.

9.3.2 Changes to Structural Model and IAD Dynamics

1. The effects of modeling the presence of the payload and the attachment rope lines to the toroids.
2. Determine aeroelastic responses with different rigid aeroshell attachments. The results showed that the extent of the rigid shield to which the flexible portion of the IAD attaches is critical in determining the peak deflections of the tip of the structure.

3. Determine the lowest possible inflation pressure for which the model will not buckle.
4. Determine aeroelastic responses at various banking rates (1.5, 2.5, or 6 deg/sec^2) and including the effects of gravity (due to the high mass payload).
5. Determine aeroelastic responses of modified IAD model design and/or properties, such as different size of toroids, different number of toroids, different toroids assembly, etc.
6. Determine the aeroelastic responses due to puncture of single or multiple inflated elements. This can be done by deflation of one or two toroidal tubes in the model. The effect of varying the location of the toroid failure should also be considered.

10 REFERENCES

1. CFD Research Corporation, “MDICE Multi-Disciplinary Computing Environment, User’s Manual,” Version 6.0, December 2003.
2. CFD Research Corporation, “MDICE Multi-Disciplinary Computing Environment, Programmers’s Guide,” Version 6.0, October 2001.
3. CFD Research Corporation, “CFD-FASTRAN, V2004: User's Manual,” March 2004.
4. CFD Research Corporation, “Co-Phy User’s Manual,” 2005.
5. Sheta, E. F., Meyer, B., and Habchi, S. D., "Aerodynamic Support of the ARES Program," Final Report, Contract No. ATK-23525, Alliant TechSystems, Brigham City, UT, October 2008.
6. Sheta, E. F., Meyer, B., and Habchi, S. D., "Aerodynamic Analysis of ARES I-X Upper Stage Wake Effect," Final Report, Contract No. 45-010003-CG, NASA Marshal Flight Space Center, Huntsville, AL, May 2008.
7. Liever, P.A.; Habchi, S.D.; Engelund, W.C.: Martin, J.G.: “Stage Separation Analysis of the X-43A Research Vehicle,” AIAA Paper 2004-4725.
8. Liever, P.A.; Habchi, S.D.: “Separation Analysis of Launch Vehicle Crew Escape Systems,” AIAA Paper 2004-4726.
9. Liever, P.A.; Habchi, S.D.; Burnell, S.I.; Lingard, S.: “CFD Prediction of the Beagle 2 Aerodynamic Database,” AIAA Paper 2002-0683.
10. S.D. Habchi, G.S. Hufford, and T. Marquette, “Navier-Stokes Computational Analysis of the B-1A Escape Capsule,” 33rd Aerospace Sciences Meeting; Reno, NV; Jan. 9-12, 1995.
11. Sheta, E. F., Venugopalan, V., Tan X.G., Harrand, V. J., and Habchi, S. D., "Tightly Coupled Aerothermoelastic Analysis Tool for Hypersonic Vehicle Structures," Final Report, SBIR Phase I, Contract No. FA8650-09-M-3929, Air Force Research Laboratory, Dayton, OH, October 2009.
12. Sheta, E. F., Moses, R. W., and Huttsell, L. J., "Active Smart Material Control System for Buffet Alleviation," *Journal of Sound and Vibration*, Academic Press, Vol. 292, No. 5, July 2006, pp. 854-868.
13. Sheta, E. F., "Alleviation of Vertical Tail Buffeting of F/A-18 Aircraft," *Journal of Aircraft*, Vol. 41, No. 2, March/April 2004, pp. 322-330.
14. Sheta, E. F., and Huttsell, L. J., "Characteristics of F/A-18 Vertical Tail Buffeting," *Journal of Fluids and Structures*, Academic Press, Vol. 17, No. 3, April 2003, pp. 461-477.
15. Liever, P.A.; Sheta, E. F.; Habchi, S.D.: “Aeroelastic Simulation Tool For Inflatable Ballute Aerocapture,” 1st JANNAF Spacecraft Propulsion Subcommittee Meeting, JPM/LPS/SPS Joint Meeting, Monterey, California, December 2005.
16. Liever, P. A., Venugopalan, V., Talley, C., Burns, J., Tosh, A., Sheta, E. F., and Habchi, S. D., "Aeroelastic Simulation Tool for Inflatable Ballute Aerocapture," Final Report, SBIR Phase II, Contract No. NNM06AA10C, NASA Marshal Space Center, Huntsville, AL, November 2007.
17. Buck, G., “Testing of flexible ballutes in hypersonic wind tunnels for planetary aerocapture,” AIAA Paper 2006-1319, 44th AIAA Aerospace Sciences Meeting and Exhibit, Reno, NV, Jan. 9-12 2006.

11 APPENDIX A – CFDRC FEM VALIDATION AGAINST NASTRAN

A.1 CFDRC-FEM

CFDRC's FEM code used in this project is part of a multi-physics and multi-scale computational physics (CoPhy) software package, written in the object-oriented language C++ and developed by CFDRC. It contains several modules including: fluid dynamics, heat transfer, structures dynamics, electrostatics, chemistry, and several others. All of the modules can be solved in a loosely or tightly coupled fashion. Each module solves physics on the same or different grids, and data exchanges between different modules are seamless. The modules that are most related to the present project is the finite element module or CFDRC-FEM.

CFDRC-FEM solves stress/deformation, and acoustic in a Lagrangian frame. The most relevant features of CFDRC-FEM are:

- Both explicit and implicit FEM solver available for different time-scale applications;
- Unstructured mixed element grids including tetra, hexa, pyramid, prism, octree;
- Accurate finite elements such as mixed formulation for incompressible materials, and locking-free shell formulation and solid-shell formulation applicable for both smooth and folded shell structure;
- Multi-rigid body dynamics with various joints and its implicit coupling with flexible bodies;
- Various non-linear material models such as hyperelasticity, viscoelasticity and elastoplasticity;
- Various surface interaction such as Contact-impact algorithm, tied-interface to connect domains with different mesh;
- Acoustic model and its implicit interaction with structural dynamics;
- Capable of calculate large structured/unstructured mesh movement in the fluid domain;
- Efficient large-scale parallel computing with interface to Petsc solver;
- Seamless coupling with fluid dynamic module and heat transfer module.

A.2 Introduction and Motivation for Testing

CFD Research Corporation has developed a finite element solver CRDRC-FEM that is fully compliant with the Multi - Disciplinary Computing Environment (MDICE) integration tool, and thus used in analyzing a variety of multi disciplinary problems.

The motivation for the development of an in house finite element solver is the ability to have a tight integration between the FEM solver and other codes inside the MDICE environment. This reason is the driving force behind CFDRC's development of a new code over another tool such as NASTRAN. While it is acknowledged that NASTRAN is the industry standard for FEM solvers it does not offer the hooks inside the code required to tightly integrate it with MDICE. Therefore, MDICE integration must be done in a loosely coupled way. This requires the creation,

passing and reading of files between NASTRAN and an MDICE compliant interface. This method quickly becomes computationally unacceptable for complicated nonlinear multi-disciplinary simulations.

For CFDRC FEM to be accepted as a potential stand in for NASTRAN in computationally intensive simulations it requires comparison against NASTRAN for both static and dynamic, linear and nonlinear problems. Therefore, the main focus of this document is to compare the solutions from CFDRC FEM against NASTRAN for geometric nonlinear problems. The testing was conducted at AFRL by Edward Alyanak as part of an AFRL supported program on large non-linear aeroelastic bending of thin wings.

A.3 CFDRC FEM Elements

CFDRC FEM's development is based on three degree of freedom per node elements. The basic elements include:

- Beams
- Shells
- Tetrahedral
- Hexagon
- Pentagon

The main difference comes in the beam and shell elements. Both of these elements contain 8 nodes per element. The beam becomes a long thin hexagon and the shell becomes a flat plate like hexagon. The solver contains checks to ensure that the element dimensions are consistent with the assumptions made in the beam and shell element formulations.

A.4 Test Case 1 – Slender Beam Test

The first test case is developed to test the geometric nonlinear capabilities of CFDRC FEM against the Nastran. The specific element formulations being analyzed will be:

- NASTRAN
  - CBEAM
  - CHEXA
- CFDRC FEM
  - beam
  - disp – displacement based hexa formulation
  - mixed – mixed hexa formulation

- Problem Description:
The initial test case will consist of a long slender beam. The beam will have an aspect ratio of 100.

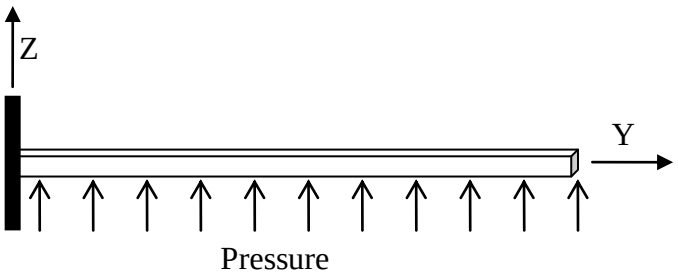

Figure A.1 Test Case 1 – Long slender beam

As seen in Figure A.1, the beam is cantilevered at one end with a pressure force perpendicular to the beam axis applied to the bottom side of the beam. This places the beam in bending. The specific properties and load cases for the beam are:

- Dimensions
  - Length – 100.0 in
  - Height – 1.0 in
  - Width – 1.0 in
- Material Properties
  - Elastic Modulus – 10.4 x 10^6 psi
  - Poison's Ratio – 0.33
  - Wt. Density – 0.1 lb/in^3
    - Wt. to Mass Factor - 0.00259 s^2/in
    - Mass Density – 0.00259 slinch / in^3
      - slinch – lb · s^2 / in
- Pressure Load
  - applied along the length of the beam
    - Case 1: 1.00 psi
    - Case 2: 4.00 psi

- Static Results

The static results of the beam deflection were analyzed for two nastran elements (CHEXA, CBEAM) and for three CFDRCFEM elements (displacement, mixed and beam). The static analysis types consisted of linear, large displacement nonlinear, and follower force nonlinear cases. The test case will detect differences in the element formulations as well as investigate the accuracy of the nonlinear iterative scheme used in the solution inside CFDRCFEM. Different mesh refinements were created for each type of element. The mesh used for each element is as follows:

- CHEXA
  - 900 x 3 x 3
  - 400 x 2 x 2
  - 10 x 1 x 1
- CBEAM
  - 10 x 1 x 1

- displacement (disp)
  - 900 x 3 x 3
  - 400 x 2 x 2
- mixed
  - 900 x 3 x 3
  - 400 x 2 x 2
- beam
  - 50 x 5 x 5
  - 10 x 1 x 1

Inside CFDRCFEM the beam formulation must have a long aspect ratio. This is why a 50 x 5 x 5 mesh was used over a 400 x 2 x 2 mesh that was used for the other brick elements. The CHEXA 900 x 3 x 3 mesh was selected as the "Valid" solution for comparison. This mesh of CHEXA proved to be a converged solution when it is compared against the CHEXA 400 x 2 x 2 mesh.

The results, along with percent error or deviations from the CHEXA valid mesh can be seen in Table A.1 and A.2. These tables represent the first and second load cases. Further results can be seen in Figure A.9 contained at the end of this appendix. This figure plots the beam tip displacement for both Y and Z deflections, where the coordinate system is defined in Figure A.1. From Figure A.9 and Tables 1 and 2 it is clear that the CHEXA, for all but the coarse mesh, CBEAM and CFDRCFEM beam elements are in very close agreement with each other. This is expected since the test case is a beam bending test case. The results further indicate that the CFDRCFEM displacement formulation for a hexagonal element is stiff for the bending case and the mixed formulation is flexible. This is acceptable since a beam element formulation is available for a hexagonal element for bending applications of long aspect ratio structural components. In the table, it is clear that the CFDRCFEM beam element performs very well, even for a 10 x 1 x 1 mesh refinement.

Table A.1 Static results for load case 1

NASTRAN RESULTS		CFDRCFEM disp ELEMENT		CFDRCFEM disp ELEMENT		CFDRCFEM beam ELEMENT	
MESH CHEXA 900 x 3 x 3 (Valid)		MESH disp 900 x 3 x 3		MESH mixed 900 x 3 x 3		MESH beam 50 x 5 x 5	
0.0000	14.4078	0.0000	14.0263	0.0000	14.7965	0.0000	14.4246
-1.1808	14.3223	-1.1200	13.9507	-1.2457	14.7079	-1.1841	14.3440
-1.1609	14.2060	-1.1018	13.8407	-1.2229	14.5773	-1.1634	14.2224
MESH CHEXA 400 x 2 x 2		*%Error*	*%Error*	*%Error*	*%Error*	*%Error*	*%Error*
0.0000	14.4064	0.0000	-2.6479	0.0000	2.6978	0.0000	0.1166
-1.1806	14.3214	-5.1454	-2.5946	5.5033	2.6923	0.2820	0.1515
-1.1608	14.2047	-5.0963	-2.5715	5.3384	2.6140	0.2110	0.1154
MESH CHEXA 10 x 1 x 1		MESH disp 400 x 2 x 2		MESH mixed 400 x 2 x 2		MESH beam 10 x 1 x 1	
0.0000	14.2532	0.0000	13.4154	0.0000	15.2188	0.0000	14.4244
-1.1154	13.8933	-1.0250	13.3493	-1.3175	15.1227	-1.1846	14.3469
-1.0985	13.7916	-1.0099	13.2538	-1.2918	14.9798	-1.1640	14.2262
MESH CBEAM 10 x 1 x 1		*%Error*	*%Error*	*%Error*	*%Error*	*%Error*	*%Error*
0.0000	14.4782	0.0000	-6.8879	-6.2500	5.6289	0.0000	0.1152
-1.1897	14.3923	-13.1902	-6.7936	11.5816	5.5881	0.3231	0.1718
-1.1643	14.2434	-13.0120	-6.7028	11.2745	5.4470	0.2653	0.1422

Table A.2 Static beam results for load case 2

NASTRAN RESULTS		CFDRCFEM disp ELEMENT		CFDRCFEM disp ELEMENT		CFDRCFEM beam ELEMENT	
MESH CHEXA 900 x 3 x 3 (Valid)		MESH disp 900 x 3 x 3		MESH mixed 900 x 3 x 3		MESH beam 50 x 5 x 5	
0.0000	57.6311	0.0000	56.1052	0.0000	59.1858	0.0000	57.6983
-17.6152	52.5100	-16.7885	51.4028	-18.5405	53.7045	-17.6991	52.6293
-13.8149	47.2638	-13.2756	46.4025	-14.3675	48.1201	-13.8416	47.3113
MESH CHEXA 400 x 2 x 2		*%Error*	*%Error*	*%Error*	*%Error*	*%Error*	*%Error*
0.0000	57.6257	-7.6923	-2.6477	0.0000	2.6977	0.0000	0.1166
-17.6123	52.5055	-4.6931	-2.1086	5.2529	2.2749	0.4766	0.2272
-13.8131	47.2602	-3.9038	-1.8222	4.0000	1.8119	0.1929	0.1005
MESH CHEXA 10 x 1 x 1		MESH disp 400 x 2 x 2		MESH mixed 400 x 2 x 2		MESH beam 10 x 1 x 1	
0.0000	57.0127	0.0000	53.6617	0.0000	60.8753	0.0000	57.6974
-12.6647	44.7901	-15.4488	49.5269	-19.5291	54.9346	-17.7990	52.7676
-10.8251	41.8062	-12.4115	44.9790	-14.9664	49.0268	-13.9169	47.4315
MESH CBEAM 10 x 1 x 1		*%Error*	*%Error*	*%Error*	*%Error*	*%Error*	*%Error*
0.0000	57.9130	0.0000	-6.8876	0.0000	5.6293	0.0000	0.1150
-17.9639	53.0561	-12.2985	-5.6810	10.8651	4.6175	1.0437	0.4906
-13.7225	47.1877	-10.1586	-4.8341	8.3352	3.7301	0.7383	0.3548

When the errors are evaluated between Tables A.1 and A.2 it is important to note that the linear error does not change for every element type. This should be the result; any deviation would indicate a coding error was present. The nonlinear solution errors do slightly increase as the tip deflection magnitudes increase from around 15% for load case 1 and 50% for load case 2. This is a result of the nonlinear solution being a combination of linear solutions done in an iterative manner. More intermediate linear solutions were solved in determining the solution to the higher load deflection then the lower load. Since each individual linear solution contains some error this error compounds as the iteration number increases.

- Dynamic Results

For the dynamic case only the cases that were similar in the static case were analyzed. The same loading was applied to an undeflected beam at t = 0.0 seconds. The response history was then analyzed for both the low and high load cases.

The meshes and integration time steps used are the following:

- CBEAM
  - 10 x 1 x 1
    - dt = 0.0001
    - dt = 0.001
- beam
  - 10 x 1 x 1
    - Explicit dt = 3.571×10^{-6}
    - Implicit dt = 0.0001
    - Implicit dt = 0.001

- Results

Figures A.2 – A.4 contain the results of the dynamic analysis test cases. The cases that were run were run because the agreed well in the static sense, and were somewhat less computationally intensive. The specific focus was the accuracy of CFDRCFEM in time integration and mass modeling.

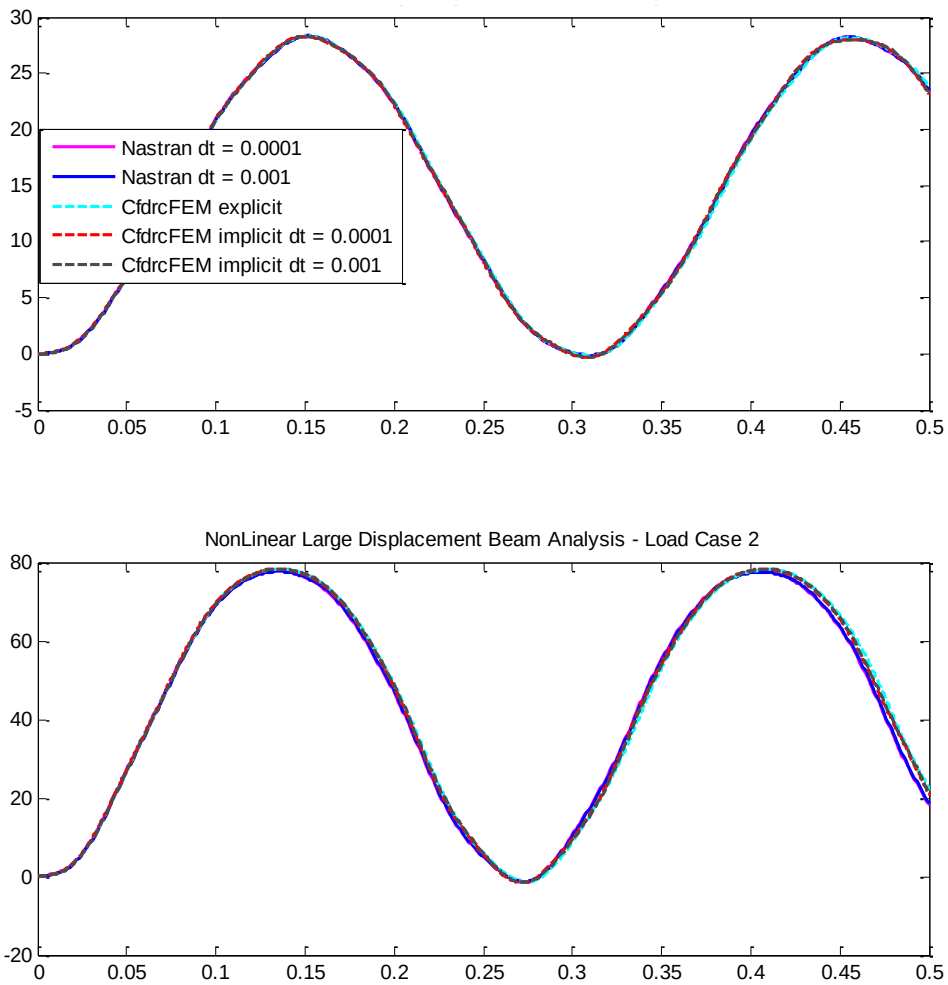

Figure A.2 Dynamic Large Displacement Analysis Results, Beam

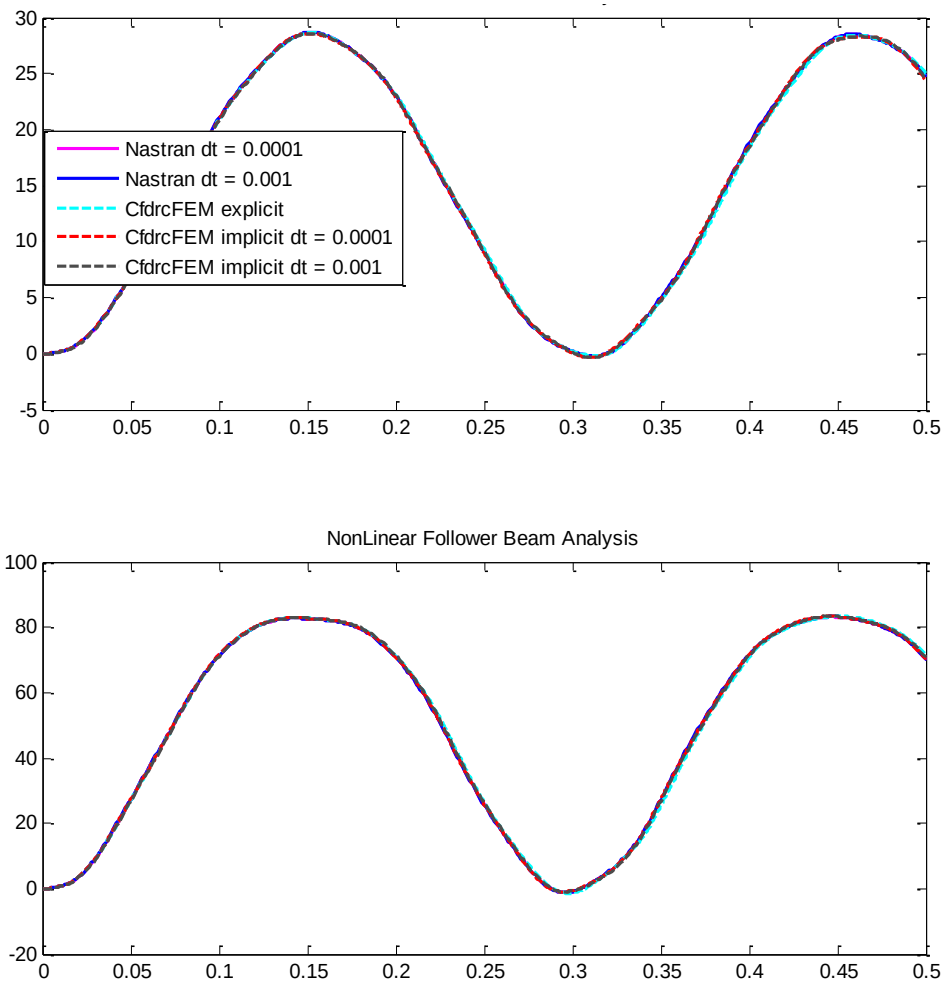

Figure A.3 Dynamic Follower Force Analysis Results, Beam

Form figures A.2 and A.3 it is immediately clear that the results for all of the test cases are very close to each other for dynamic geometric nonlinear analysis. This is critical for dynamic aeroelasticity analysis, since the amplitude and frequency of oscillation can have a great impact on aeroelastic stability prediction.

Below, Figure A.4 just reinforces the need for nonlinear structural analysis. The results are generated for the high load case for the dynamic beam problem. Figure A.4 presents the same solution for the linear, large displacement and follower force result. While both nonlinear analyses have similar displacements the frequency of oscillation are different. This is because the deflection path is longer for the follower force case, and thus it has a longer period. This can be seen from the static results shown in Figure A.9. The linear solution is significantly different. The deflection magnitudes and frequencies are not in any type of agreement. The need for nonlinear structural analysis for large displacement bending applications is quite clear after examining this figure.

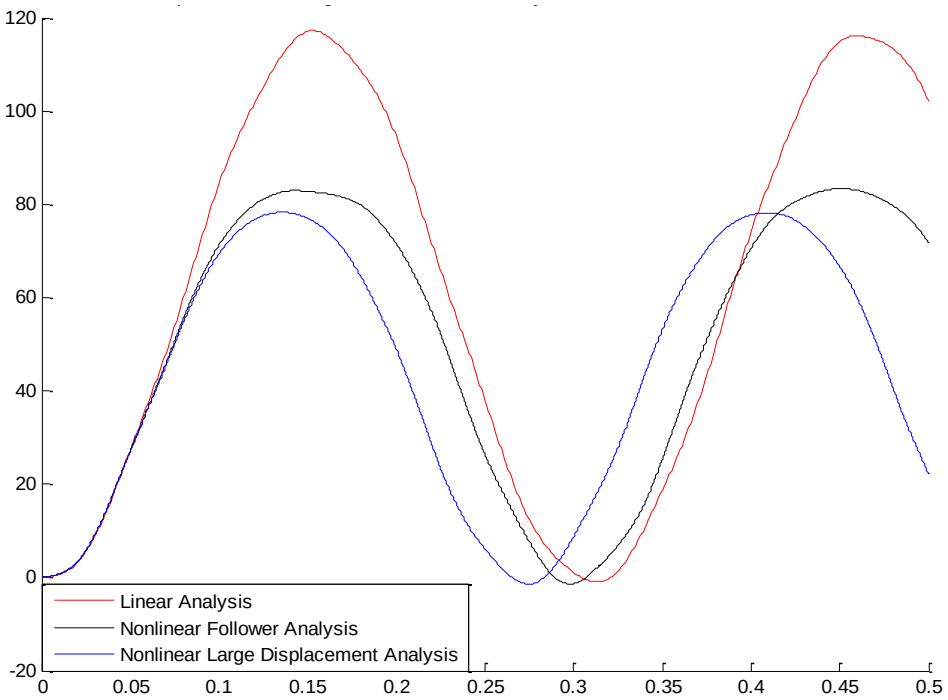

Figure A.4 Dynamic Comparison of Linear, Large Displacement and Follower Force Results for Example 1, Beam: Load Case 2

A.5 Test Case 2 – Plate Test Case

The second test case is developed to test the geometric nonlinear capabilities of CFDRC FEM against the Nastran for wing like plate structures. In the first test case the bending capabilities were considered. In this case a coupled bending and twisting is examined. This case is designed to mimic typical wing like deformations. The specific element formulations being analyzed will be:

- Nastran
  - CHEXA
- CFDRC FEM
  - pshell
  - disp – displacement based hexa formulation
  - mixed – mixed hexa formulation

- Problem Description

The test case consists of a thin plate as seen in Figure A.5. The plate is of a length 100in and a thickness of 1.0in. The root chord is 20in and the tip cord will be 14in. The plate is cantilevered at the root.

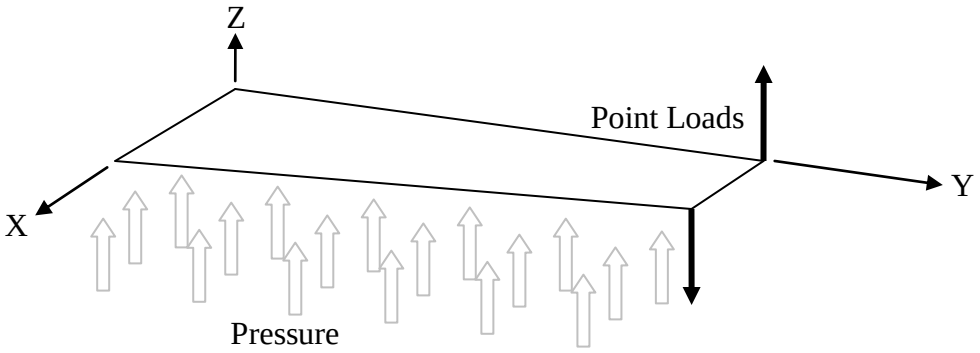

Figure A.5 Test Case 2 – Wing like Plate

- Dimensions
  - Length (y) – 100.0 in
  - Height (z) – 1.0 in
  - Width (x) – 20.0 in tapering to 14.0 in
- Material Properties
  - Elastic Modulus – 10.4×10^6 psi
  - Poison's Ratio – 0.33
  - Wt. Density – 0.1 lb/in^3
    - Wt. to Mass Factor - 0.00259 s^2/in
    - Mass Density – 0.00259 slinch / in^3
      - slinch – lb · s^2 / in
- Pressure Load
  - applied along the bottom of the plate
    - Case 1: 1.00 psi
    - Case 2: 3.00 psi
- Tip Point Loading (applied along with pressure)
  - Applied in the positive z – direction at leading edge
  - Applied in the negative z – direction at the trailing edge
    - Case 1: 200 lbs
    - Case 2: 2000 lbs

- Static Results

Different mesh refinements were created for each type of element. The mesh used for each element is as follows:

- CHEXA
  - 100 x 1 x 20
  - 10 x 1 x 2
- displacement (disp)
  - 100 x 1 x 20
  - 10 x 1 x 2

- mixed
    - 100 x 1 x 20
    - 10 x 1 x 2
- pshell
    - 100 x 1 x 20
    - 10 x 1 x 2

The data format shown is for the tip of the plate or "wing". The format is shown in Figure A.6 below, and corresponds to the results in Tables A.3 and A.4.

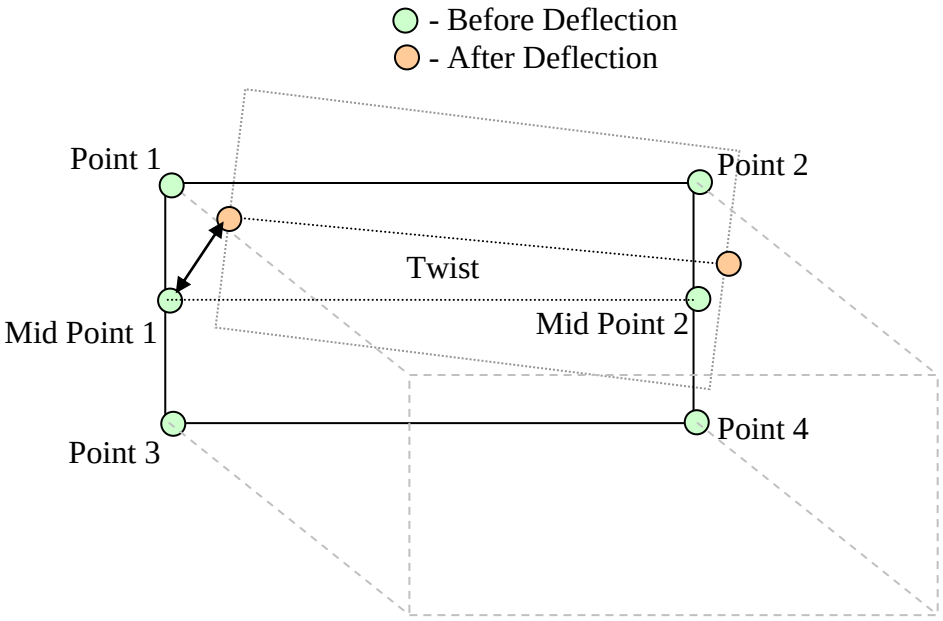

Figure A.6 Data format for Static Results Case 2

Table A.3 contains the results for the lower loading magnitudes applied to the plate. The error calculations are relative to the Nastran solution with the same mesh. The same mesh is used since a direct comparison is being carried out. The formulation for the percent error for each element is shown below.

$$\%Error = \frac{100\%}{7} \times \left[\begin{array}{l} \left(\frac{\partial x_{cfdrc}^{LEtip} - \partial x_{nastran}^{LEtip}}{\partial x_{nastran}^{LEtip}} \right) + \left(\frac{\partial x_{cfdrc}^{TEtip} - \partial x_{nastran}^{TEtip}}{\partial x_{nastran}^{LEtip}} \right) + \left(\frac{\partial y_{cfdrc}^{LEtip} - \partial y_{nastran}^{LEtip}}{\partial y_{nastran}^{LEtip}} \right) + \\ \left(\frac{\partial y_{cfdrc}^{TEtip} - \partial y_{nastran}^{TEtip}}{\partial y_{nastran}^{LEtip}} \right) + \left(\frac{\partial z_{cfdrc}^{LEtip} - \partial z_{nastran}^{LEtip}}{\partial z_{nastran}^{LEtip}} \right) + \left(\frac{\partial z_{cfdrc}^{TEtip} - \partial z_{nastran}^{TEtip}}{\partial z_{nastran}^{LEtip}} \right) + \\ \left(\frac{\alpha_{cfdrc} - \alpha_{nastran}}{\alpha_{nastran}} \right) \end{array} \right]$$

Table A.3 Static Plate Results for Load Case 1

	NASTRAN RESULTS			CFDRCFEM disp ELEMENT			CFDRCFEM mixed ELEMENT			CFDRCFEM pshell ELEMENT		
	dX (in)	dY (in)	dZ (in)	dX (in)	dY (in)	dZ (in)	dX (in)	dY (in)	dZ (in)	dX (in)	dY (in)	dZ (in)
	MESH CHEXA 100 x 1 x 20			MESH disp 100 x 1 x 20			MESH mixed 100 x 1 x 20			MESH pshell 100 x 1 x 20		
	LINEAR			LINEAR			LINEAR			LINEAR		
LE Tip	0.00	0.00	11.84	0.00	0.00	7.55	0.00	0.00	14.77	0.00	0.00	11.84
TE Tip	0.00	0.00	11.61	0.00	0.00	7.33	0.00	0.00	14.53	0.00	0.00	11.61
Twist (deg)	0.97			0.89	% Error =	-11.6217	0.99	% Error =	7.4177	0.97	% Error =	0.0043
	LGDISP			LGDISP			LGDISP			LGDISP		
LE Tip	0.04	-0.79	11.70	0.02	-0.33	7.51	0.05	-1.22	14.50	0.04	-0.79	11.71
TE Tip	0.04	-0.76	11.47	0.02	-0.31	7.30	0.05	-1.18	14.27	0.04	-0.76	11.47
Twist (deg)	0.95			0.88	% Error =	-41.4391	0.97	% Error =	30.5498	0.95	% Error =	-0.0049
	FOLLOWER			FOLLOWER			FOLLOWER			FOLLOWER		
LE Tip	0.04	-0.80	11.76	0.02	-0.33	7.52	0.06	-1.24	14.63	0.04	-0.80	11.77
TE Tip	0.04	-0.77	11.53	0.02	-0.31	7.31	0.05	-1.21	14.39	0.04	-0.77	11.53
Twist (deg)	0.95			0.89	% Error =	-41.5062	0.97	% Error =	31.1321	0.95	% Error =	-0.0551
	MESH CHEXA 10 x 1 x 2			MESH disp 10 x 1 x 2			MESH mixed 10 x 1 x 2			MESH pshell 10 x 1 x 2		
LE Tip	LINEAR			LINEAR			LINEAR			LINEAR		
TE Tip	0.00	0.00	11.81	0.00	0.00	0.38	0.00	0.00	0.39	0.00	0.00	11.82
Twist (deg)	0.00	0.00	11.57	0.00	0.00	0.24	0.00	0.00	0.25	0.00	0.00	11.59
	0.96			0.57	% Error =	-33.6207	0.57	% Error =	-33.6030	0.95	% Error =	-0.1180
LE Tip	LGDISP			LGDISP			LGDISP			LGDISP		
TE Tip	0.04	-0.75	11.41	0.00	0.00	0.38	0.00	0.00	0.39	0.04	-0.79	11.67
Twist (deg)	0.04	-0.73	11.19	0.00	0.00	0.24	0.00	0.00	0.25	0.04	-0.76	11.44
	0.93			0.57	% Error =	-90.2443	0.57	% Error =	-90.2244	0.93	% Error =	3.4615
LE Tip	FOLLOWER			FOLLOWER			FOLLOWER			FOLLOWER		
TE Tip	0.04	-0.76	11.47	0.00	0.00	0.38	0.00	0.00	0.39	0.04	-0.79	11.72
Twist (deg)	0.04	-0.74	11.25	0.00	0.00	0.24	0.00	0.00	0.25	0.04	-0.77	11.49
	0.93			0.57	% Error =	-90.1231	0.57	% Error =	-90.0871	0.94	% Error =	3.4285

As expected the CFDRCFEM pshell element performs very well relative to NASTRAN results. The displacement and mixed formulation elements again are not good choices for these types of problems. Their main use is for modeling of solid structures as opposed to structures with bending deformation. They are shown in the comparison for the purpose of completeness. Table A.4 is the same format as Table A.3 and contains the results for the high load case. The higher load produces significantly more nonlinear deflection behavior then the low load.

Table A.4 Static Plate Results for Load Case 2

	NASTRAN RESULTS			CFDRCFEM disp ELEMENT			CFDRCFEM mixed ELEMENT			CFDRCFEM pshell ELEMENT		
	dX (in)	dY (in)	dZ (in)	dX (in)	dY (in)	dZ (in)	dX (in)	dY (in)	dZ (in)	dX (in)	dY (in)	dZ (in)
	MESH CHEXA 100 x 1 x 20			MESH disp 100 x 1 x 20			MESH mixed 100 x 1 x 20			MESH pshell 100 x 1 x 20		
	LINEAR			LINEAR			LINEAR			LINEAR		
LE Tip	0.00	0.00	36.33	0.00	0.00	23.38	0.00	0.00	45.11	0.00	0.00	36.33
TE Tip	0.00	0.00	34.38	0.00	0.00	21.50	0.00	0.00	43.14	0.00	0.00	34.38
Twist (deg)	7.93			7.64	% Error =	-10.9631	8.01	% Error =	7.2425	7.92	% Error =	-0.0182
	LGDISP			LGDISP			LGDISP			LGDISP		
LE Tip	0.77	-6.26	32.51	0.51	-2.85	22.15	0.97	-9.01	38.70	0.77	-6.26	32.51
TE Tip	0.66	-5.68	30.87	0.40	-2.45	20.44	0.86	-8.33	37.09	0.66	-5.68	30.87
Twist (deg)	6.75			7.04	% Error =	-35.2387	6.60	% Error =	26.2132	6.75	% Error =	-0.0015
	FOLLOWER			FOLLOWER			FOLLOWER			FOLLOWER		
LE Tip	0.87	-6.85	33.92	0.55	-2.95	22.54	1.15	-10.36	41.24	0.87	-6.86	33.93
TE Tip	0.76	-6.25	32.25	0.43	-2.55	20.81	1.04	-9.63	39.61	0.76	-6.26	32.27
Twist (deg)	6.82			7.12	% Error =	-37.2492	6.67	% Error =	31.0110	6.82	% Error =	0.0595
	MESH CHEXA 10 x 1 x 2			MESH disp 10 x 1 x 2			MESH mixed 10 x 1 x 2			MESH pshell 10 x 1 x 2		
LE Tip	LINEAR			LINEAR			LINEAR			LINEAR		
TE Tip	0.00	0.00	36.20	0.00	0.00	1.63	0.00	0.00	1.65	0.00	0.00	36.24
Twist (deg)	0.00	0.00	34.30	0.00	0.00	0.24	0.00	0.00	0.26	0.00	0.00	34.34
	7.77			5.65	% Error =	-31.7271	5.67	% Error =	-31.6758	7.74	% Error =	-0.0252
LE Tip	LGDISP			LGDISP			LGDISP			LGDISP		
TE Tip	0.64	-5.46	30.28	0.04	-0.01	1.62	0.04	-0.01	1.64	0.74	-6.18	32.30
Twist (deg)	0.55	-4.94	28.72	-0.02	0.00	0.25	-0.03	0.00	0.26	0.64	-5.63	30.70
	6.41			5.60	% Error =	-86.3296	5.63	% Error =	-86.2472	6.56	% Error =	10.9936
LE Tip	FOLLOWER			FOLLOWER			FOLLOWER			FOLLOWER		
TE Tip	0.71	-5.87	31.33	0.05	-0.01	1.61	0.05	-0.01	1.63	0.83	-6.75	33.65
Twist (deg)	0.61	-5.34	29.76	-0.02	0.00	0.25	-0.02	0.00	0.26	0.73	-6.17	32.03
	6.45			5.59	% Error =	-86.2475	5.62	% Error =	-86.1343	6.62	% Error =	12.3333

The general comments for this load case are similar then for load case 1. However, it is important to recognize that the percent error calculations are against the NASTRAN solution with the *same mesh*. This is significant when looking at the pshell element solution for a 10 x 1 x 2 mesh size. The coarse NASTRAN solution is relatively stiff and the pshell element is not. The error relative to the 100 x 1 x 20 NASTRAN solution for the pshell 10 x 1 x 2 mesh is: -0.40%, -1.80%, and -2.18% respectively for the linear, large displacement and follower force solutions. This further emphasizes the solid performance of the pshell element in CFDRCFEM for modeling of geometrically nonlinear structural behavior in wing like structures.

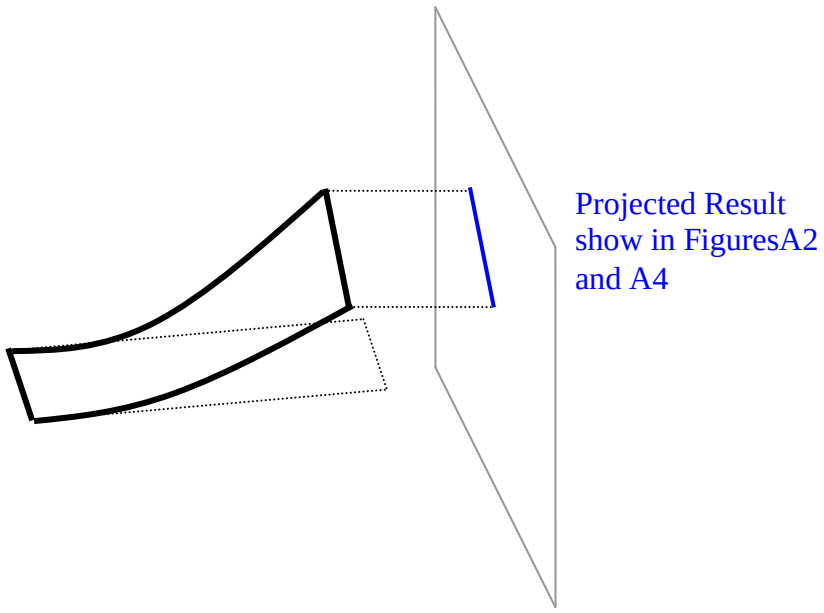

Figure A.7 Result Format for Plate Displacement Plots A2 and A4

Plots of the results contained in Tables A.3 and A.4 are contained at the end of this appendix in Figures A.9 – A.12. Plots A.9 and A.111 are results as if the plate tip was projected onto a plane generated at a constant Y-axis location. Figure A.7 above shows the plate tip projection onto the viewing plane that these plots are generated from.

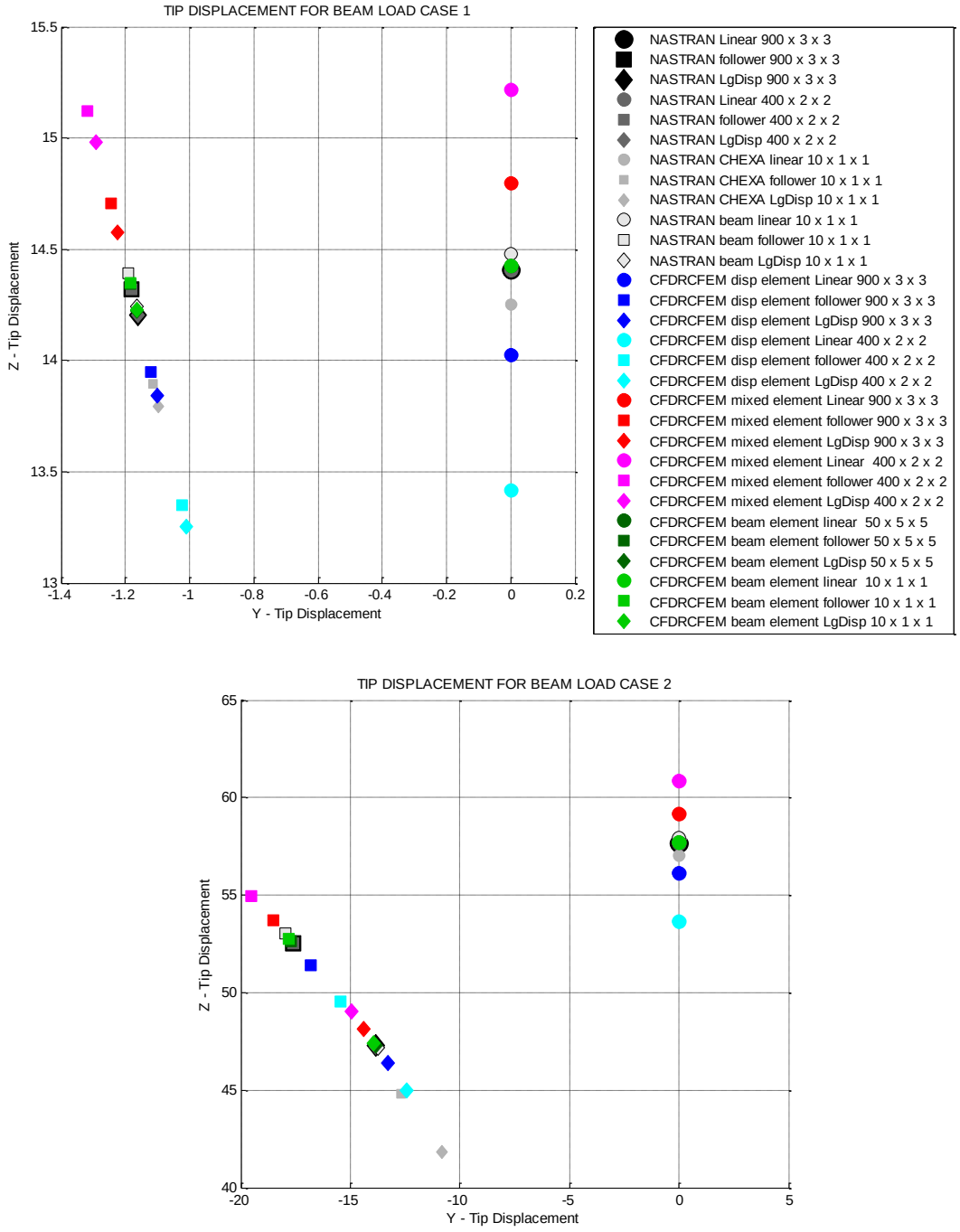

Figure A.8 Static Tip Displacements for Beam Test Case

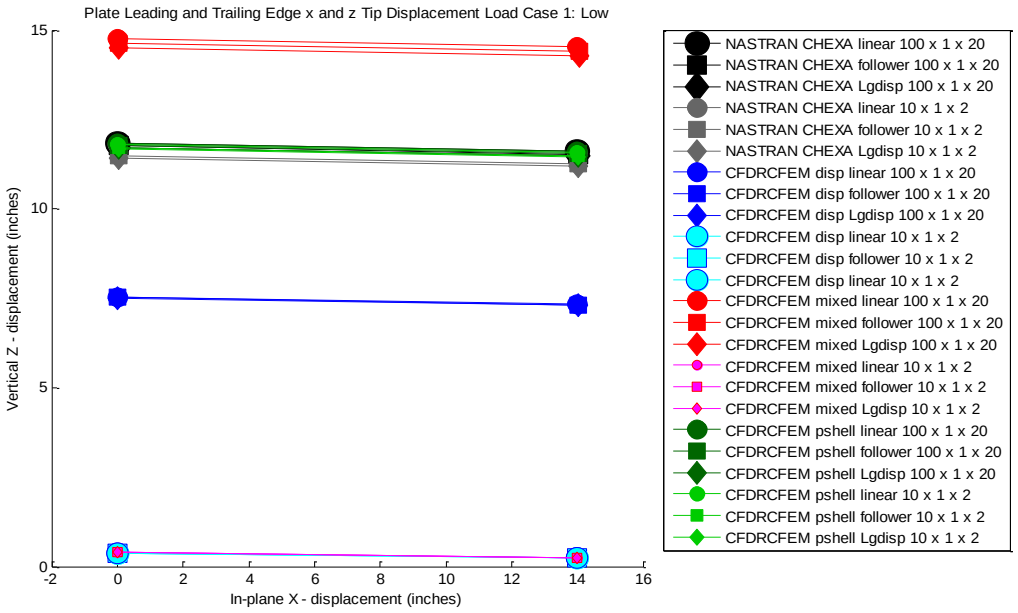

Figure A.9 Static Tip Displacements for Plate, Load Case 1, z-x plane

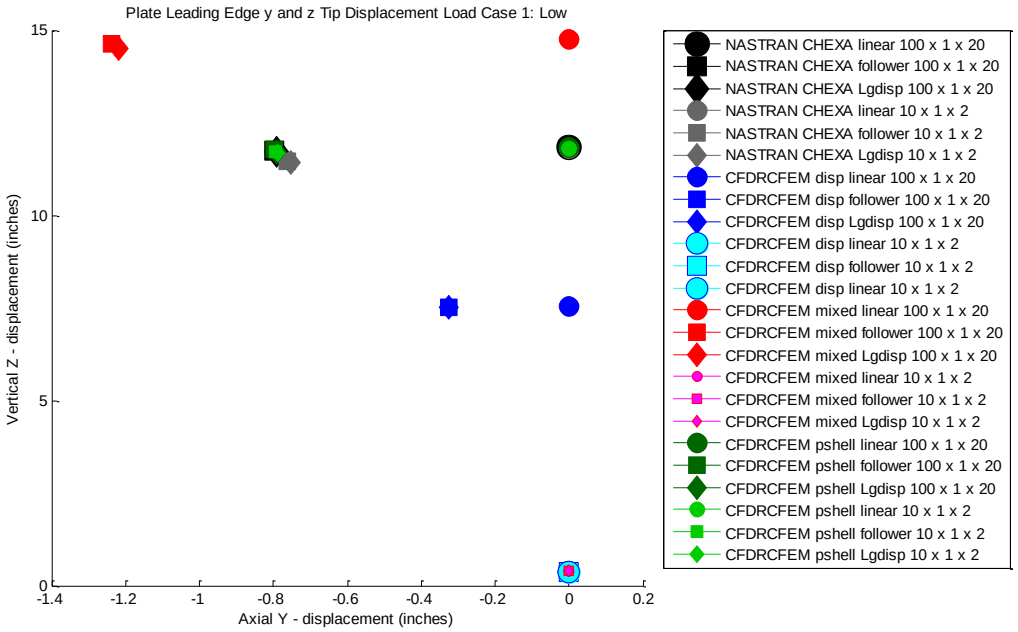

Figure A.10 Static Tip Displacements for Plate, Load Case 1, z-y plane

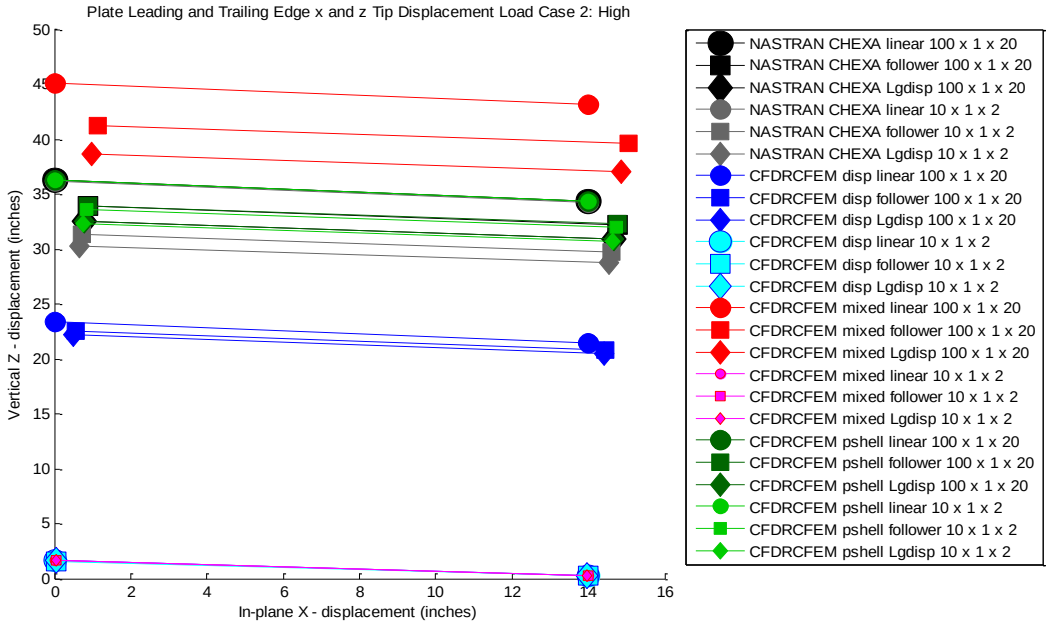

Figure A.11 Static Tip Displacements for Plate, Load Case 2, z-x plane

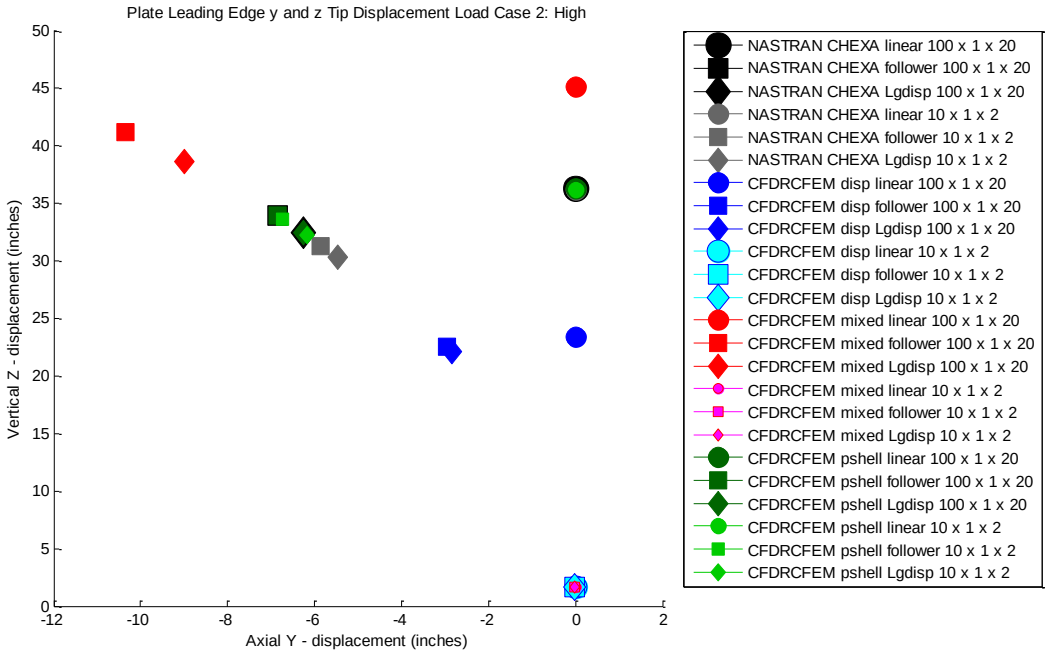

Figure A.12 Static Tip Displacements for Plate, Load Case 2, z-y plane

In addition to fully parallelized FSI within CoPhy, its FEM module, CFDRC-FEM can be used in serial or parallel mode with third party CFD codes through the Multi Disciplinary Integrated Computing Environment (MDICE). In the following example, a FSI coupled problem between CFD-FASTRAN, a density based CFD solver and COBI's FEM module is presented for Mach 5.6 flow over a thin film ballute structure. A ballute (balloon- parachute) is a flexible, inflatable device made from thin film material with thickness on the order of 1 to 10mil, which is deployed to increase the drag of the vehicle to which it is attached during reentry/aerocapture maneuvers. As seen in Figure A.13, the clamped ballute consisted of a clamped, rigid nose section and a fixed outer support and a 1-mil thick kapton film was stretched in between them. Details of the model can be seen in [Gregory M. Buck, 2006]. This problem was run using the explicit solver in COBI. The results can be seen in Figure A.14.

(a) Cross section of test model *(b) Assembled test model* *(c) Model during and after testing*

Figure A.13 CF4 wind tunnel model [Gregory M. Buck, 2006].

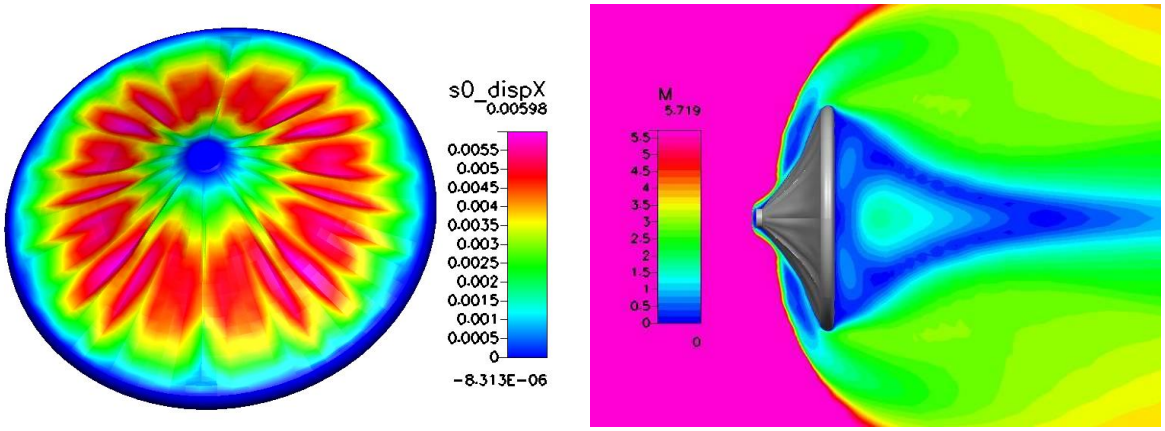

(a) Displacement Contours *(b) Mach Contours Around Deformed Ballute after FSI*

Figure A.14 FSI coupling results between CFD-FASTRAN and CFDRC-FEM for a thin film ballute.

REPORT DOCUMENTATION PAGE

Form Approved
OMB No. 0704-0188

1. REPORT DATE *(DD-MM-YYYY)*	2. REPORT TYPE	3. DATES COVERED *(From - To)*
01- 08 - 2010	Contractor Report	

4. TITLE AND SUBTITLE
Aero-Structural Assessment of an Inflatable Aerodynamic Decelerator

5a. CONTRACT NUMBER
NNM06AA10C

5b. GRANT NUMBER

5c. PROGRAM ELEMENT NUMBER

6. AUTHOR(S)
Sheta, Essam F.; Venugopalan, Vinod; Tan, X. G.; Liever, Peter A.; Habchi, Sami D.

5d. PROJECT NUMBER

5e. TASK NUMBER

5f. WORK UNIT NUMBER

7. PERFORMING ORGANIZATION NAME(S) AND ADDRESS(ES)
NASA Langley Research Center
Hampton, VA 23681-2199

8. PERFORMING ORGANIZATION REPORT NUMBER
CFDRC Report: 8927/6

9. SPONSORING/MONITORING AGENCY NAME(S) AND ADDRESS(ES)
National Aeronautics and Space Administration
Washington, DC 20546-0001

10. SPONSOR/MONITOR'S ACRONYM(S)
NASA

11. SPONSOR/MONITOR'S REPORT NUMBER(S)
NASA/CR-2010-216731

12. DISTRIBUTION/AVAILABILITY STATEMENT
Unclassified - Unlimited
Subject Category 18
Availability: NASA CASI (443) 757-5802

13. SUPPLEMENTARY NOTES
This project is sponsored by NASA Langley Research Center as follow-on to Phase II SBIR (NASA Contract Number NNM06AA10C).
Langley Technical Monitor: Jamshid A. Samareh

14. ABSTRACT

NASA is conducting an Entry, Descent and Landing Systems Analysis (EDL-SA) Study to determine the key technology development projects that should be undertaken for enabling the landing of large payloads on Mars for both human and robotic missions. Inflatable Aerodynamic Decelerators (IADs) are one of the candidate technologies. A variety of EDL architectures are under consideration. The current effort is conducted for development and simulations of computational framework for inflatable structures.

15. SUBJECT TERMS
Inflatable structures; Descent; Landing; EDL; Toroids

16. SECURITY CLASSIFICATION OF:			17. LIMITATION OF ABSTRACT	18. NUMBER OF PAGES	19a. NAME OF RESPONSIBLE PERSON
a. REPORT	b. ABSTRACT	c. THIS PAGE			STI Help Desk (email: help@sti.nasa.gov)
					19b. TELEPHONE NUMBER *(Include area code)*
U	U	U	UU	143	(443) 757-5802